8-2010

EVALUATION OF GEOMETRIC SCALE EFFECTS FOR SCRAMJET ISOLATORS

Jaime Enrique Perez
University of Tennessee - Knoxville, jperez1@utk.edu

To the Graduate Council:

I am submitting herewith a thesis written by Jaime Enrique Perez entitled "EVALUATION OF GEOMETRIC SCALE EFFECTS FOR SCRAMJET ISOLATORS." I have examined the final electronic copy of this thesis for form and content and recommend that it be accepted in partial fulfillment of the requirements for the degree of Master of Science, with a major in Aviation Systems.

Dr. Stephen Corda, Major Professor

We have read this thesis and recommend its acceptance:

Peter U. Solies, Frank G. Collins

Accepted for the Council:
Dixie L. Thompson

Vice Provost and Dean of the Graduate School

(Original signatures are on file with official student records.)

To the Graduate Council:

I am submitting herewith a thesis written by Jaime E. Pérez entitled "Evaluation of Geometric Scale Effects for Scramjet Isolators." I have examined the final electronic copy of this thesis for form and content and recommend that it be accepted in partial fulfillment of the requirements for the degree of Master of Science, with a major in Aviation Systems.

Stephen Corda, Major Professor

We have read this thesis
and recommend its acceptance:

Peter U. Solies

Frank G. Collins

Accepted for the Council:

Carolyn R. Hodges

Vice Provost and Dean of the Graduate School

(Original signatures are on file with official student records.)

EVALUATION OF GEOMETRIC SCALE EFFECTS FOR SCRAMJET ISOLATORS

A Thesis
Presented for the
Master of Science Degree
The University of Tennessee Space Institute

Jaime Enrique Pérez
August 2010

Acknowledgements

I'd like to thank my family for bearing with me as I worked on this thesis for the past two and a half years. I would also like to thank Dr. Corda for his advice and guidance in this field, who I know is looking forward to me finishing. I would like to acknowledge the Air Force for their assistance in helping me pursue this degree. I would like to thank Dr. Tam, Dr. Eklund, Dr. Lin, and Dr. Jackson of Taitech and Air Force Research Labs for providing their assistance and insight in the research of the nozzle-isolator problem.

Abstract

A numerical analysis was conducted to study the effects of geometrically scaling scramjet inlet-combustor isolators. Three-dimensional fully viscous numerical simulation of the flow inside constant area rectangular ducts, with a downstream back pressure condition, was analyzed using the SolidWorks Flow Simulation software. The baseline, or 1X, isolator configuration has a 1" x 2.67" cross section and 20" length. This baseline configuration was scaled up based on the 1X configuration mass flow to 10X and 100X configurations, with ten and one hundred times the mass flow rate, respectively. The isolator aspect ratio of 2.67 was held constant for all configurations. To provide for code validation, the Flow Simulation program was first used to analyze a converging-diverging channel and a wind tunnel nozzle. The channel case was compared with analytical theory and showed good agreement. The nozzle case was compared with AFRL experimental data and showed good agreement with the entrance and exit conditions (P_{i0}= 40 psia, T_{i0}= 530ºR, P_e= 18.86 psia, T_e= 456ºR, respectively). While the boundary layer thickness remained constant, the boundary layer thickness with respect to the isolator height decreased as the scale increased. For all the isolator simulations, a shock train was expected to form inside the duct. However, the flow simulation failed to generate this flow pattern, due to improper sizing of the isolator and combustor for a 3-D model or having a low pressure ratio of 2.38. Instead, a single normal shock wave was established at the same relative location within the length of each duct, approximately 80% of the duct length from the isolator entrance. The shape of the shock changed as the scale increased from a normal shock wave, to a bifurcated shock wave, and to a normal shock train, respectively for the 1X, 10X, and 100X models.

Table of Contents

List of Tables

Table Page

List of Figures

Figure Page

Nomenclature

A	=	Cross-sectional area
AR	=	Aspect ratio (width to height)
D	=	characteristic length
h	=	isolator height
H	=	nozzle height
HR	=	height comparison ratio
l	=	isolator length
L	=	nozzle length
L_{st}	=	shock train length
LH	=	length to height ratio
LR	=	length comparison ratio
$\dot{m}$	=	mass flow rate
M	=	Mach number
P	=	pressure
PR	=	static back pressure to static inlet pressure ratio
Re	=	Reynolds number
T	=	temperature
$\mathcal{T}$	=	thrust
V	=	velocity
w	=	isolator width
x	=	scaling parameter
y	=	nozzle surface location
Δy	=	difference between upper and lower surface of nozzle

γ = specific heat ratio

θ = boundary layer momentum thickness

μ = kinematic viscosity

Superscript

' = condition at shock wave leading edge

* = choked condition

Subscript

0 = total condition

1 = condition at facility nozzle exit

b = condition at isolator extension piece exit

B = combustor

e = exit location

i = inlet condition

I = isolator

I-B = isolator to combustor

max = maximum value

s = static condition

th = throat condition

x = scaled model

I. Introduction

A. Scramjet Isolators Design and Purpose

The scramjet engine has no moving parts compared to turbo machinery; however the engine itself is still sectioned into components. The scramjet has four components: inlet, isolator, combustor, and diffuser/nozzle. The inlet is designed to capture the air and stabilize the flow before entering the isolator and combustor. Upon exiting the isolator, the air enters the combustor at supersonic speeds as fuel is injected and burned before exiting the combustor.

The purpose of the isolator is to separate or "isolate" the inlet from the combustor, preventing inlet unstart from high combustor back pressure. Without this critical component, the engine could reach an unstart condition, resulting in the disgorgement of airflow from the combustor and out the inlet. This would result in unacceptable drag and a dramatic loss of thrust.

The inlet flow is allowed to stabilize through a series of reflecting shock waves creating a uniform exit plane pressure before entering the combustor. This shock train forms inside the length of the isolator through the interaction of a strong shock wave, boundary layer separation along the wall surfaces, and an overexpansion process. This process acts as a natural valve, which allows flow to come into the combustor and prevents the combusting air from returning into the inlet. In order to prevent disgorgement, the exit pressure of the shock train must be higher than the back pressure of the combustor, which has a range between the maximum combustion pressure and the inlet static pressure. As an adjustment for changes in back pressure, the shock train translates downstream until the exit plane pressure of the shock train is equal to the back pressure of the combustor. Sudden pressure rises across each shockwave in the isolator causes the flow at the wall to reverse locally as the flow near the surface separates from the wall. As the

flow propagates downstream, each shockwave becomes weaker and the boundary layer separates further from the wall. The core flow between the boundary layers experiences an aerodynamic converging-diverging nozzle effect, which was formed by the overexpansion process and boundary layer separation. By having a higher pressure at the shock train exit, compared to the back pressure of the combustor, the shock train prevents the combustor air flow to reverse towards the inlet. This in effect isolates the inlet from the combustor, and prevents inlet unstart.[1]

B. Prior Research on Scramjet Isolators

In 1973, Waltrup and Billig[2,3] conducted experiments to investigate shock trains in cylindrical ducts. They discuss how the shock train develops for supersonic flow inside a cylindrical duct by initially separating the boundary layer inside the duct. If the pressure rise for a weak oblique shock is sufficient to separate the boundary layer, and the overall duct pressure rise is greater, a repeating series of reflecting shocks forms to produce this pressure rise. The compression ratio is dependent upon Mach number, duct diameter, boundary layer momentum thickness, Reynolds number, wall pressure, and Pitot pressure distributions. Waltrup and Billig developed a correlation which related shock train pressure rises and boundary layer properties. AFRL simplified the correlation into a quadratic formula using the parameters mentioned.

$$\frac{\left(L_{st}/D\right)\left(M'^{2}-1\right)\mathrm{Re}_{\theta}^{0.25}}{\left(\theta/D\right)^{0.5}} = 50\left(\frac{P_{\max}}{P'}-1\right)+170\left(\frac{P_{\max}}{P'}-1\right)^{2} \qquad (1)$$

In 1989, Stockbridge[4] investigated shock trains inside an annular duct. It was determined that an isolator duct of sufficient length was necessary to prevent a shock structure, produced by

combustion, in a supersonic stream from propagating upstream and disrupting the external flow of the air inlet.

However, there is a disadvantage in increasing the length of the isolator. It can result in a decrease of total pressure recovery at the main combustor entrance and an increase in overall weight. It was also determined that a normal shock would develop in an over expanded or "throttled" duct flow, when the boundary layer was removed or the Mach number was close to one. For the shock train to develop the boundary layer must thicken and the Mach number must increase to supersonic conditions. The starting point of the shock train is determined by the growth, separation, and reattachment to the wall. Stockbridge concluded, from the formation of the shock train and the qualitative results, the annular duct had similar results to the cylindrical duct experiment, performed by Waltrup and Billig, and that Eq. 1 was consistent for both experiments.[5]

In 1990, Dutton and Carroll performed experiments on rectangular ducts experiencing turbulent boundary-layer interactions with multiple shocks. The procedures used were spark schlieren photography, surface oil flow visualization, and laser Doppler velocimetry. The flow was tested for M=1.6 and 2.45 at the entrance. It was determined, through testing, that as Mach number increased, the length of the interacting boundary-layer and shock increased.

The tendency for the shock to form a repeated oblique shock from a normal shock increased with the Mach number as well. It was observed that the stability of the shock train decreased as the Mach number increased. Two modes of unsteadiness were observed for oblique shocks: a high frequency streamwise oscillation, and a low frequency transverse oscillation. The low frequency oscillation is believed to be related to the neutrally stable shock pattern which has an asymmetric profile. This asymmetry can be noticed through the flow patterns along opposing walls.[5]

During this same year, Billig, Corda, and Stockbridge wrote a technical review for Applied Physics Laboratory, which gave an overall assessment of past experiments performed in solving combustor-inlet interactions problems. It displays the location of the isolator inside the scramjet, along with the pressure profile relative to the overall pressure distribution of the engine. During the time of this review, it was believed that experimental methods were needed to obtain a necessary database rather than computational fluid dynamics (CFD). It was recommended that one technique allow for overexpanding or back-pressuring the flow to generate shock trains. The strength of the shock train increases with heat release. It was determined that with modest heat release rates, the pressure rise at the first shock wave of a shock train is sufficient to separate the boundary layer. It was also determined that the pressure through the entire shock train can be significantly larger than the initial pressure rise after boundary-layer separation. The review gives an overall assessment of the varying geometries for ducts and the corresponding correlation Eq. 1. The review concluded that the data obtained can be used to assist future experiments using CFD modeling as a tool to develop numerical simulations of the flow phenomena.[6]

In 1991, P. Lin, Rao, and O'Connor worked to investigate the behavior of normal shocks using CFD modeling for 2-D flow inside a constant area isolator. It was determined that, as the back pressure at the exit of the isolator increases, the shock length will increase inside the duct. Depending on the intensity of the pressure differential, the boundary-layer momentum thickness can affect the shock length. For high pressure differentials or pressure ratios, an increase in the boundary-layer thickness can increase the shock length. It was discovered that as the inlet Mach number increases, the shock profile changes from normal to oblique. The increase in Mach number also increases the number and spacing of the series of secondary shocks. For normal shocks, the spacing is less affected by momentum thickness. It was also discovered that for a given back pressure, an increase in the Mach number would decrease the shock length.[7]

In 1992, Sullins and McLafferty took an experimental approach toward investigating shock trains in rectangular ducts. These ducts were tested using a throttle valve installed downstream of the diffuser, which created a back pressure induced shock train inside the duct. It was determined that the shock train can reach up to 95% of the normal shock strength, but at a cost of a substantially long duct. Once the flow is subsonic behind the train and the boundary layer reattaches to the constant area duct, the friction tends to accelerate the flow. This occurrence also follows the Fanno flow theory. “At some point, the pressure decrease due to Fanno flow will be greater than the increase due to mixing” of air, from the combustor, “and a maximum pressure is reached by a gradual decrease in pressure” from the Fanno flow process and interaction with the combustor air.

It states Eq. 1 as being an optimal correlation for relating shock train length and the pressure rise for a given set of inflow conditions. This correlation is believed to help in establishing the optimal isolator design length. The data collected for this experiment was stated to be for “a constant area duct with a uniform entrance profile except for the lower wall boundary layer.” The intention of the lower wall boundary layer was to simulate a vehicle with a long forebody. The duct was long to ensure that the full shock train was captured for M=2 and 2.85 at the entrance. It was observed that the shock system was still symmetric, even after a difference in boundary layer profiles between the upper and lower wall surfaces. The boundary layer profiles were given as algebraic equations for the thickness and momentum thickness.[8]

In 1993, the geometry of ducts became a primary focus for understanding how shock trains form when the shape of the cross section varied, and determined which is more efficient. Using numerical simulations, a 2-D planar duct and a cylindrical duct at Mach 2.6 were tested at various back pressures. It was determined that cylindrical ducts developed normal shock trains compared to the mix of oblique and normal shocks developed by the planar duct. It was also determined that for the same back pressure and inflow condition, the shock train developed in the

cylindrical duct is shorter compared to the planar duct. However, the computed total pressure losses between the two ducts approached the same value with increasing back pressure.[9]

In 2003, a study was performed to verify if there is a difference in performance between low and high aspect ratio isolators. Each isolator was tested at various back pressures, it was determined that the aspect ratio shows a significant difference in how isolators operate. It was concluded that more experimental testing was needed to be done combined with CFD testing to explore the phenomena of high aspect isolators as most tests done before never truly explored the phenomena shown in their experimentations.[10]

The Air Force Research Laboratory (AFRL) and Taitech performed a wind tunnel experiment; which compared the geometric cross section of an axis-symmetric isolator and a rectangular isolator duct. Using Mach 2.2 and Mach 1.8 nozzles to simulate inlet conditions for a constant-area isolator, they varied the back pressure and temperature at the isolator exit and observed the length and position of shock trains in the isolator. They also monitored the effects of geometry and surface roughness on the shock train to see what possible changes may occur with the shock train. Their objective was to characterize three constant-area isolators which are listed in table 1. The surfaces of the isolators with TBC (thermal barrier coating) coating have a roughness of 520-610 μ-in. The ceramic panels listed for I-3 were considered smooth with low thermal conductivity, with the information obtained from Dr. Tam, Dr. Lin, and Dr. Eklund, the ceramic tiles were measured to have a roughness of 43 μ-in. For future experimentation, the roughness of the tiles obtained from these AFRL experiments will be used to configure the walls of the isolators.[11]

The effect of temperature and heat transfer on the shock train structure and isolator performance was evaluated. They found that heat addition to a low Mach number flow inside the isolator can choke the flow and decrease the isolator performance. Heat addition to supersonic flow increases the boundary layer thickness and decreases both the amount of heat required to

choke the flow and the flow Mach number. Shock trains will be long in high-temperature flow and may require a long isolator to prevent engine unstart.[12]

The shock train location, pressure profile inside the shock train, and the flow properties at the exit plane were measured and compared with Billig's correlation for shock trains. In order to characterize the pressure profile of the shock train, AFRL used the correlation:

$$\left[\left(P_s - P_s'\right)\Big/P_0\right]\Big/\left(P_b/P_1\right) \tag{2}$$

This term is used to avoid the use of boundary layer-related parameters (boundary layer momentum thickness or Reynolds number) used in Eq. 1. It was determined that the boundary layer thickness could not be accurately determined in their experiment set-up. They also considered the effect of incoming flow Mach number on the normalized pressure profile in Eq. 2. The results from these profiles showed similarities to each other, having profiles with narrow bands and a small dependence on geometry, the only exception to this observation came from the rectangular Mach 1.8 flow, which showed high scatter.

Using computational fluid dynamics (CFD), they attempted to predict the experimental results. The CFD case proved to be accurate to the experimental results. The data, obtained from the CFD model and the wind tunnel tests, was planned to be used for a more in depth analysis of isolator scaling. In the end, AFRL concluded they did not have enough information on how scaling the isolator would affect their results in determining the location and size of the shock trains.

AFRL did not consider the effects of scaling on isolators, which may have a significant effect on their design. Scaling is a critical method to analyze models without having to design large wind tunnels. By scaling the model, the same flow and thermodynamic patterns can be

monitored for a smaller model compared to the full scale model. Scaling effects need to be monitored as they relate to shock train length and location.

In 2007, CFD was used to reproduce the setup and test data collected from the AFRL test case. Different turbulence models were tested and compared with the wind tunnel data. They attempted to create 2D and 3D CFD models using RANS and Large Eddy Simulation (LES) turbulence calculations. In the tests, comparisons were made between RANS and LES to simulate the same flow, their grid adaptation techniques, and turbulent intensity.

Through these tests, it was found that inlet turbulence intensity and the implementation of adaptive grid refinement are not critical factors in the determination of isolator shock location. However, the turbulence model can adversely affect the results of isolator shocks. There is a distinct difference between the Spalart-Allmaras and k-epsilon models. It was discovered that the RANS model was more accurate compared to the LES turbulence model. The contour plots displayed from these models give a qualitative example for future simulation models and programs.[13]

C. CFD Approach towards Scaling Isolators

Using a CFD computer, an analytical approach was taken to evaluate the geometric scale effects for scramjet isolators. The first step was to determine the capabilities of the CFD code, by comparing the simulation results with a theoretical case, and an experimental wind tunnel case. The theoretical case was setup to demonstrate the reactions of supersonic flow inside a two-dimensional converging-diverging duct. This was designed to compare the accuracy and precision of the CFD simulation with the theoretical results, which used thermodynamic laws and principles to calculate the flow. Mach number, pressure, temperature, and shockwave and expansion angles were parameters used to compare these results. The wind tunnel experiment

consisted of a test facility nozzle, with a supersonic exit, connected to a scramjet isolator test section with a throttled back pressure. The normalized wall static pressure was measured down the length of the isolator, while the normalized total pressure, normalized static temperature, and Mach number were measured at the exit of the isolator.

The final step towards evaluating the geometric scale effects for scramjet isolators involved running a simulation for 1X, 10X, and 100X isolators, where each isolator had 1, 10, and 100 times the mass flow rate passing through the isolators, respectively. The shockwave patterns, pressure, temperature, and Mach number profiles were observed for each isolator. Using a normalized height and length for each isolator, the pressure, temperature, and Mach number profiles could be compared. These profiles were used to evaluate the overall effects of geometrically scaling the scramjet isolators.

II. Methods

Prior to evaluating isolator scaling effects, two code validation cases were analyzed: (1) supersonic flow through a two-dimensional converging-diverging (C-D) channel, and (2) supersonic flow through a three-dimensional, rectangular cross-section isolator connected at the exit of a test facility C-D nozzle. For the converging-diverging channel, the CFD results were compared with the exact theoretical values. For the three dimensional isolator, the CFD results were compared with experimental data from wind tunnel tests.

The computations were performed using Dassault Systemes Flow Simulation 2009[14] on a Dell Precision T7400 computer with an Intel Xeon CPU (Dual-Core 2.66 GHz, 1.63 GB). Each isolator computation required approximately 48 hours to complete.

Flow Simulation uses Navier-Stokes equations and a density weighted time average (Favre-averaged) for turbulent flow, which separates time-averaged effects of the flow turbulence from the mean-flow for compressible flow. The Favre-averaged procedure introduces Reynolds stresses into the equations with transport equations for the turbulent kinetic energy and dissipation rate.[14]

Flow Simulation uses a Modified Wall Function to simulate[14] boundary layers. This model uses a Van Driest profile compared to the standard logarithmic profile used in other CFD simulators. The purpose of the Modified Wall Function is to provide accurate velocity and temperature boundary conditions for the Favre-averaged Navier-Stokes equations. The turbulence model uses k-ε inputs or turbulence intensity and length. These inputs are needed to assess how accurate the experiment is with real world models as well as how the simulation compares with previous CFD experiments.

Flow simulation solves the governing equations with the finite volume method on a spatially rectangular computational mesh designed in the Cartesian coordinate system with the

planes orthogonal to its axes and refined locally at the solid/fluid interface and in the fluid region during calculation. Values of all the physical variables are stored at the mesh centers. The governing equations are discretized in a conservative form due to the finite volume method. The governing equations are integrated over a control volume which is a grid cell, and then approximated with the cell-centered values of the physical variables. The spatial derivatives are approximated with implicit difference operators of second-order accuracy. The time derivatives are approximated with an implicit first-order Euler scheme. The viscosity of the numerical scheme is negligible with respect to the fluid viscosity. The second-order upwind spatial approximations are based on the implicitly treated modified Leonard's QUICK approximations and the Total Variation Diminishing method.

The numerical solution technique uses stages to create a locally refined rectangular computational mesh and used then for solving the governing equations on it. The meshing procedures are performed before the calculation. The first procedure uses partial cells for near wall conditions to monitor heat and mass fluxes; and uses a basic rectangular mesh, which is determined by the computational domain and not dependent on the solid/fluid interface. The next step involves capturing the solid/fluid interface by uniformly splitting, into smaller cells, the basic mesh cells intersecting with the solid/fluid interface. The next stage allows cells to either merge or split further to refine the mesh at the solid/fluid interface curvatures. The final stage allows the mesh to be refined by using a narrow channel criterion. This results in cells being merged in low-gradient regions and splitting of cells in high-gradient regions.[14]

The algorithmic parameters are stated to be velocity, temperature, density, turbulent energy, turbulent dissipation rate, and component concentrations in fluid mixtures. These parameters are put into a vector form and are added with a pressure correction, which is considered an auxiliary variable. These discrete functions are stored at the cell centers. The numerical algorithm in Flow Simulation solves for fully implicit discrete convection/diffusion

equations. These equations obtain the intermediate values of momentum and the final values of turbulent parameters, temperature, and species concentrations. The pressure correction and a final momentum field are combined to satisfy the discrete fully implicit continuity equation.

In order to decrease the solution time, Flow Simulation uses a technique called the multigrid method. Given the mesh, a sequence of grids (grid levels) is constructed, with decreasing nodes. On every such grid, the residual of the associated system of algebraic equations is restricted to a coarser grid level, forming the right hand side of the system on that grid. When the solution on the coarse grid is computed, it is interpolated to the finer grid and used there as a correction to the result of the previous iteration. After that, several smoothing iterations are performed. This procedure is applied repeatedly on every grid level until the corresponding iteration meets the stopping criteria. The stopping criteria are based on the EFD.Lab convergence process. EFD.Lab treats all steady state flow problems as a time-dependent problem. The solver module iterates on an internally determined time step to seek a steady state flow field. The program has built-in criteria, however, it was recommended to have user-defined criterion or goals. The two primary goals are surface and global goals. The surface goal is a physical parameter calculated on a user specified face of the model. The global goal is a physical parameter calculated within the entire computational domain.

As an example, one experiment calculated the airflow inside a nozzle-isolator configuration. The number of iterations (time-steps and grid points) calculated varied from 16,000-45,000 iterations for .0018s-.018s of simulated airflow propagation and development.

A. Two-Dimensional, Converging-Diverging Channel Configuration and Setup

Using a Flow Simulation validation case setup for a converging-diverging nozzle, the resulting airflow was hand-calculated using thermodynamic laws and equations. The flow for the

validation case uses classical Navier-Stokes equations. The Favre-averaged Navier-Stokes equations are used to calculate the flow patterns for the isolator cases. The validation case is discussed in Appendix A and B. Appendix B discusses the theoretical approach towards obtaining the thermodynamic properties of the flow through a converging-diverging channel with given dimensions.

The geometry of the converging-diverging channel is given in figure 1. The entrance and exit of the channel have equal heights of 1.181 inches with a center section of 0.677 inches, which is less than half the height of the entrance. The overall length of the channel is 12.28 inches with a maximum height of 1.181 inches. As the flow approaches the corner between the throat and diverging section, expansion waves are created, which accelerates the flow downstream. These waves are reflected and intersect at points along the diverging section of the wall. The last section has a constant area; however, the corner where the diverging section turns the wall to run parallel with the upper wall induces an oblique shock which decelerates the flow. Shock wave/expansion theory was used to obtain analytical results for the flow in the channel. Complete numerical details of the theoretical analysis are shown in Appendices A and B.[15]

The static pressure and temperature at the exit and entrance of the channel were assumed to be 14.69 lbs/in^2 and 527.8ºR. For the flow to be established inside the channel, everything inside the channel was determined to be M=3, P=14.69 lbs/in^2, and T=527.8ºR. The channel walls were to be considered adiabatic. The initial conditions for the C-D channel are given in table 2.

B. Test Facility Nozzle Validation Case Configuration and Setup

Assuming isentropic flow and using the velocity-area relationship for quasi one-dimensional flow, the thermodynamic properties at the entrance and exit of the nozzle could be obtained. After finding these parameters, the boundary conditions, as well as the initial conditions, could be set-up to run Flow simulation. The walls were assumed to be smooth and adiabatic.

The initial conditions throughout the entire flow were based on the assumption of choked flow at the throat of the facility nozzle. The following ratios were used to establish this condition:

$$\frac{P_{th}}{P_0} = \left(1 + \frac{\gamma - 1}{2} M_{th}^2\right)^{\gamma/1-\gamma} = .5283 \text{ for } M_{th}=1 \text{ and } \gamma=1.4 \tag{3}$$

$$\frac{T_{th}}{T_0} = \left(1 + \frac{\gamma - 1}{2} M_{th}^2\right)^{-1} = .8333 \tag{4}$$

Equations (3) and (4) are the isentropic conditions for choked flow. Using the isentropic equations, along with the information provided by AFRL for the reservoir conditions (P_0= 40 psia, T_0= 530 ºR), the initial conditions for choked flow are P_{th}= 21.132 psia and T_{th}= 441.667 ºR. Using the side profile of the nozzle from fig. 7, and assuming the geometry of the nozzle is rectangular with a constant width of 4 inches, the area ratio for the exit and throat (A_e/A^*), was determined to be 1.456311. The location of the throat was determined mathematically by the minimum value of y differentials (Δy). Where:

$$\Delta y = (y_{upper}) - (y_{lower}) \tag{5}$$

After this area was located, it was simply compared with the Δy of the exit plane. The ratio of Δy for the throat and exit should yield the same exact result as the area ratio for a rectangular duct.

$$\frac{A_e}{A^*} = \frac{\Delta y_e}{\Delta y^*} \tag{6}$$

Using the value given by Eq. (6), the Mach number was predicted using an iterative process by the following formula:

$$\frac{A_e}{A^*} = \frac{1}{M_e}\left[\frac{2}{\gamma+1}\left(1+\frac{\gamma-1}{2}M_e^2\right)\right]^{\frac{(\gamma+1)}{2(\gamma-1)}} \tag{7}$$

Eq. (7)[15] predicted an exit speed of M_e=1.815776. However, this value is not needed to set up the exit boundary condition for the facility nozzle. The flow needs the pressure and temperature at the exit for a successful test. Repeating Eq. (5) and (6) for M_e=1.815776 will yield P_e=9.086 psia and T_e= 842.4ºR at the exit plane of the nozzle. This was the set up for the exit boundary condition of the nozzle.

The nozzle was assumed to have smooth and adiabatic walls, however, viscous flow could be observed near the walls. The location and thickness of the boundary layer were to be analyzed in anticipation of the isolator experiment. The facility nozzle exit conditions would be the basis for the isolator entrance conditions.

Table 3 gives the parameters used to create standard air flow through the M=1.8 test facility nozzle. The parameters used for the air flows are predicted exit values as determined through theoretical calculations for a perfect gas. The resolution level is higher than compared to other simulations due to the testing of accuracy of the nozzle. Along with verifying the flow

conditions inside the nozzle, the intent of the experiment was to accurately determine where the boundary layer would establish itself inside the nozzle, thus the necessity to increase the resolution level from four to eight. Using fig. 7 and table 3, boundary conditions were set to establish the control volume and initial conditions for the experiment.

C. AFRL Isolator with No Back Pressure Configuration and Setup

After completing the CFD validation cases, computations were performed for the AFRL isolator geometry, representing the baseline, 1X scale isolator. The 10X and 100X isolators were scaled from this 1X baseline configuration. Isolator length and aspect ratio was held constant when scaling to the 10X and 100X configurations.

The test facility nozzle was analyzed separately from the isolator geometries, providing the nozzle exit flow conditions, including the boundary layer properties. These nozzle exit conditions were used to define the isolator entrance boundary conditions. However, technical errors prevented a complete transference of the boundary condition at the exit plane of the nozzle to the entrance of the isolator. The exit condition data, primarily the boundary layer data, was essential for an accurate and conclusive test of the isolator. The error came from the merging of meshes and the time scale for the boundary condition. The program required equal amounts of cells from the isolator entrance and the nozzle exit. Since the mesh was already refined ahead of the isolator, the grid meshing inside the isolator had a lower refinement level and would be misaligned. To resolve this issue, the flow through the facility nozzle and the isolator were computed together.

The data from the nozzle experiment, combined with the tabulated data from the AFRL isolator case, helped to predict the flow profiles of the isolator in the simulation. The nozzle data gave the location of the leading edge of the boundary layer. It also provided the boundary layer

thickness and thermodynamic properties at the entrance of the isolator. This information, combined with the pressure profile and exit conditions of the AFRL isolator case, was used as a baseline to measure the accuracy of the combined nozzle-isolator simulation.

From the three AFRL configurations, the isolator with TBC (Thermal Barrier Coating) was chosen for the CFD analysis. It was the only configuration which had enough data to be reproduced by a CFD simulation. The Mach 1.8 condition for a rectangular isolator with TBC (520 μ-in roughness) and a back pressure to inlet static pressure ratio of 2.38 was selected for having a complete data set which could be repeated by experimentation. This case had data for the exit profile along with numerical values which could be used to determine the original inlet conditions for the isolator. The data was also used to determine the nozzle thermodynamic properties. Table 4 shows the calculated results recorded from the AFRL case, this is used to establish the initial conditions for the CFD program.

In order for the program to recognize a no back pressure condition, it was decided that a constant Mach number, pressure, and temperature inside the entire configuration would be used as the initial condition. This condition would also be used at the exit as to avoid any shocks in the system, and maintain steady flow inside the configuration. The CFD program was expected to correct for this initial condition as it had done previously, for the nozzle experimentation. The isolator entrance total pressure and temperature was held constant at 40 psia and 530ºR, respectively. The nozzle and isolator walls were set to a constant temperature of 510ºR.[12] The wall roughness was 520 μ-in roughness for the isolator and 0 μ-in (smooth) roughness for the nozzle.

It was determined that any attempt to copy the no back pressure results and use the profile as the initial condition inside the entire isolator resulted in the formation of expansion and shock waves inside the isolator for the CFD simulation, even though the data from AFRL indicated the presence of neither in their experiments. Thus, a constant Mach number, static

pressure, and static temperature were used for the initial conditions in the isolator. Along with this observation, it was also noticed that inducing a pressure at the exit, which was different from the initial condition, would result in a normal shock developing near the exit.

Therefore, for the isolator to develop a no back pressure result, the CFD profile AFRL provided was used as the base condition. However, since the plots given by AFRL[11] show the values as ratios. The total pressure and temperature, from the nozzle reservoir, were used and the pressure and temperature at the exit were recalculated. The Mach number remained the same, as it was expected that this value would remain consistent as long as the pressure and temperature ratios did not change during the experimentation. The airflow had a static pressure of 10.872 psia, a static temperature of 371ºR, and a Mach number of 1.55.

The case was originally performed on a VULCAN Navier Stokes code by AFRL; however, AFRL did not state the turbulence parameters used to simulate the flow.[11]. Previous testing was done and an assessment was given of the CFD programming and how it was used to test isolators.[13] It was determined that the turbulent intensity must be low for the model to accurately represent the wind tunnel test performed by AFRL. However, the turbulent length scale was not given, and therefore it was decided to use the k-ε model. The flow was assumed to have a turbulent dissipation of 9.793 lbf*ft/s/lb and turbulent energy of .4187 Btu/lb.

D. AFRL Isolator with Back Pressure Ratio of 2.38 Configuration and Setup

The no back pressure case was recorded to ensure that all thermodynamic properties were consistent Fanno Flow and isentropic theories. It was also used to help establish the location of the shock train. For the PR=2.38 case, AFRL declared that the leading edge of the shock train is located at the point where there is a 5% rise in pressure from the no back pressure case.

After multiple experimentations, and many attempts at developing a shock train within the duct, it was decided that the initial conditions must match the flow results given by AFRL to accurately model real world conditions. Table 5 gives the parameters used to input into Flow Simulation. Figure 24 displays the original tabulated data collected from AFRL, this data was used as the initial condition for the entire length of the duct. The nozzle data was combined with the AFRL data to create the initial condition for the airflow simulation.[11]

Figures 25 and 26 were obtained by combining the data obtained in fig. 8 and fig. 10 and using a linear relationship with the pressure profile used from fig. 24. The data from fig. 25 and fig. 26 was used as a basis for the simulation to develop the proper flow conditions in the nozzle and isolator. The data beyond the nozzle exit may be inaccurate and it was anticipated that the CFD simulation would calculate the correct thermodynamic property values needed to compensate for this inaccuracy and give a proper profile. This was also done so that the simulation would capture any shocks developed in the system as the profile itself does not indicate shocks in the system.

E. Isolator Scaling Configuration and Setup

The isolators were scaled based on the inlet mass flow rate. Using the equation for thrust, and understanding what parameters affect the thrust equation, a new set of equations had to be solved in order to determine the sizing and scaling of the isolator. Given that the pressures and the velocities could vary for the engine, and the size of the engine had to remain consistent, the only variable remaining for scaling was the mass flow rate. The following equations show how the sizing of the isolators related to mass flow rate and eventually lead to the 10X and 100X scaled isolators. The 1X case was based on the AFRL PR=2.38 experiment. Using a constant cross-section, a constant pressure ratio of 2.38, and a constant inlet Mach number, the mass flow rate could be adjusted and calculated for the 10X and 100x cases.

The 1X baseline isolator had a cross section of 1" by 2.67" with a length of 20". The 10X and 100X isolators were scaled from the 1X geometry as follows: 3.16" by 8.43" cross section with a length of 63.2" for a 10X isolator, and 10" by 26.67" cross section with a length of 200" for a 100X isolator. Using the original AFRL thermodynamic data as the boundary conditions and the equations listed (eq. 8-15), the 10X and 100X isolators were calculated and tabulated.

$$\mathcal{T} = \dot{m}\left(V_e - V_i\right) + \left(P_e - P_i\right)A \tag{8}$$

$$A_I = h_I w_I \tag{9}$$

$$A_{xI} = h_{xI} w_{xI} \tag{10}$$

$$AR_I = \frac{w_I}{h_I} = \frac{w_{xI}}{h_{xI}} \tag{11}$$

$$\dot{m}_1 = \frac{P_{o1} A_I \sqrt{\gamma} M_1}{\sqrt{RT_{o1}}} \left(1 + \frac{\gamma - 1}{2} M_1^2\right)^{(\gamma+1)/(2-2\gamma)} \tag{12}$$

$$\begin{aligned} \dot{m}_{x1} &= x\dot{m}_1 \\ \dot{m}_{xb} &= x\dot{m}_b \end{aligned} \tag{13}$$

$$w_x = \sqrt{xA_I AR} = w_I \sqrt{x} \text{ where } x\text{= scaling value } (x\text{=100 for 100x model}) \tag{14}$$

$$h_x = \frac{w_x}{AR_I} \tag{15}$$

In order for the test facility nozzle to be connected to the scaled isolator models, the exit area of the nozzle had to increase. This required a redesign of the nozzle and an analysis of the airflow at the exit of the redesigned nozzle. However, the test facility nozzle could not be redesigned and scaled without testing it separately from the tests performed on the 10x and 100x isolator models. A different approach towards testing isolators was taken based on published CFD testing,[7] and used a constant area duct with M= 1.8 flow entering the duct and exiting to an open area.

This open area was essentially a box, which has a plate and 5 pressure walls. The box was intended to simulate the flow entering the combustor. The airflow exited this duct/isolator through the plate, which constituted the upstream wall of the combustor. The other 5 faces of this box could be set at various pressure and temperature conditions, which could simulate no back

pressure or increasing back pressure inside the combustor. The box along with the duct was scaled in order to remain consistent in testing.

This method was tested in 1991. However, the original case was a 2-D experiment testing normal shock train development. The original parameters used, were in metric units with values similar to the AFRL test case. The parameters used by AFRL were determined to be a valid choice for testing the models.[7] Table 6 displays the sizing of the AFRL isolator along with the expected flow conditions at the entrance and exit of the isolator. The pressure and temperature at the exit of the isolator would also be the boundary conditions for the five sides of the combustor.

Table 6 also displays the height and length of the combustor, using the set-up obtained from published experiments. The width of the combustor was determined based on an estimate of how the flow would react to a 2.67" isolator width compared to a 1" isolator height. This also would help establish a consistent aspect ratio for the combustor as the dimensions changed with the isolator scaling. Table 7 and 8 show the intended schematics and assumed mass flow rates for the 10x and 100x isolators and combustors, respectively. The cross-sectional area and mass flow rate can be compared to the 1x case using eq. 11, 12, 14, 15, and 16.

The set-up shows that the scale factor relates area and mass flow rate to be proportional with each other. Eq. 17-24 display the step-by-step method used to determine the length of the scaled isolator and dimensions of the scaled combustor. Eq. 16, 17, 19, 22 use variables that help simplify the calculations, and design of the isolator and combustor. As mentioned before, the scaling of both the combustor and the isolator must be consistent. The aspect ratio and proportionality of the lengths, heights, and widths between the isolator and combustor were also considered. The length of the shock train as well as the effects that adjusting the length, width, and height of the isolator had on airflow were monitored.

A no back pressure case for the 1x model was performed as well as a 2.38 pressure ratio case for the 1x, 10x, and 100x models.

$$AR_B = \frac{w_B}{h_B} \tag{16}$$

$$HR_{I-B} = \frac{h_I}{h_B} \tag{17}$$

$$h_{xB} = \frac{h_{xI}}{HR_{I-B}} \tag{18}$$

$$LH_B = \frac{l_B}{h_B} \tag{19}$$

$$l_{xB} = LH_B h_{xB} \tag{20}$$

$$w_{xB} = AR_B h_{xB} \tag{21}$$

$$LR_{I-B} = \frac{l_I}{l_B} \tag{22}$$

$$l_{xI} = LR_{I-B} l_{xB} \tag{23}$$

III. Results and Discussion

A. Two-Dimensional, Converging-Diverging Channel

Appendix A displays the results of the C-D computation along with a comparison of the theoretical calculation and validation case. The CFD results for the static pressure, total pressure, static temperature and Mach number along the centerline of the duct are given in figures 2, 3, 4, and 5, respectively.

The CFD computation compared well with the theoretical values. The error between theoretical and CFD calculations is up to .05% for shockwaves and 2% for expansion characteristics. However, SolidWorks compared their own theoretical calculations with the validation case performed on Flow Simulation; SolidWorks expected a .4% error for shockwaves and a .8% error for expansion waves.[14] The calculations for the validation case ended between the first expansion wave and second expansion wave. The amount of error for the final shockwave near the exit was not calculated for the validation case. The validation case did not calculate for the actual expansion process and for the region the final shockwave actually entered. Depending on the Mach number of the region ahead of the shock wave, the Mach number behind the shock wave will also be affected. The region behind the shock wave also mixed with the expansion fan ahead of the shock which affects the overall Mach number. Therefore, the data collected for x=11.79 (for the theoretical case) is insufficient to ascertain the flow properties behind the shock.

There was less than a 5% error between the theoretical calculations and the experimental results, except for the expansion process. The calculations used for the theoretical values came from the oblique shock relations, method of characteristics, and Prandtl-Meyer theory.[15] The expansion waves were calculated using the assumption that there were 2 lines expanding and

reflecting inside the nozzle. The expansion process is based upon uncertain assumptions of the expansion fan. Therefore, ~2% error is considered acceptable for the experimental results and theoretical calculation comparison.

This uncertainty can also be shown in figure 3, where there are pressure oscillations at 8 inches downstream. This can be the result of where the data was collected inside the duct. The program uses a line plot to collect data, anywhere inside the computational domain. The line traveled downstream through the center axis of the channel. The total pressure oscillation is near where the expansion fans have reflected and are traveling to the bottom of the duct before interacting with the shock wave. However, this does not completely explain why the total pressure oscillates in a system, where there should be a steady decrease or constant total pressure, since the expansion process is considered isentropic. Further investigation of the code would be needed to understand the oscillations.

In figure 5, the Mach number relative to the duct length is shown. The plot shows that the CFD results were accurately compared with the theoretical calculations. However, there is a large deviation at the exit of the duct. The exit velocity was predicted to be much lower than what the CFD results simulated. This is considered an uncertainty, as the theoretical calculations did not calculate for shock/expansion wave interaction, while the CFD program may have calculated for this.

Mach number contours for the channel are shown in figure 6. The decrease from Mach 3 as it approaches the ramp and converges towards the throat of the channel to approximately Mach 2.2. The Mach number decreases abruptly as shown by the thin line separating the two regions. The thin line represents the oblique shockwave captured using a grid mesh capturing technique to isolate this change in Mach number. This is repeated as the shockwave is reflected from the top wall and stops at the corner of the ramp and throat. As the flow exits the throat at M~1.9, the bottom wall diverges and accelerates the flow to M~2.3, creating expansion waves from the

corner of the throat and the diverging wall. The expansion waves reflect from the top wall and converge toward the oblique shock wave formed from the abrupt turn of the bottom wall. The air flow velocity decreases as it crosses the shockwave, however it increases as it exits the channel. The reason for this acceleration may be due to the location of the expansion waves relative to the shockwave. The two-dimensional C-D analysis required over 30,000 iterations and approximately 63 hours of computing time at the highest grid cell resolution for the code.

B. Test Facility Nozzle Validation Case

The initial condition inside the nozzle for the entire flow was set to Mach 1, and the flow was assumed choked at this condition. This was a necessary step to establish supersonic flow downstream beyond the throat of the nozzle. The CFD simulation corrected this assumption and calculated for the true values through an iterative process. Figures 8 through 10 display the results along the nozzle centerline. The length plotted is 11.69" from the entrance of the nozzle to the exit plane. Figure 8 and 9 show the relationship between pressure and temperature for a gas as it passes through a converging-diverging nozzle. As the flow passes the through the throat, it should transition from subsonic to supersonic flow.

Figure 10 gives the plot of how the flow accelerated from a near zero velocity to approximately Mach 1.8. The CFD computed flow compared well with the calculations used to predict the exit and throat conditions of the nozzle. Figure 11 shows that the nozzle exit Mach number was approximately 1.8 as expected for this nozzle area ratio. The computed nozzle exit data was used to determine the boundary layer thickness at the nozzle exit. The nozzle boundary layer thickness was measured to be less than 0.1 inches.

The static pressure and temperature at the nozzle exit are shown in figures 12 and 13 respectively. Both matched the values predicted using isentropic flow theory. Figure 14 shows

that the total pressure at the nozzle exit remained constant at 40 psia, indicating isentropic flow throughout the nozzle. Figure 15 gives an overall Mach number profile in the nozzle.

C. AFRL Isolator with No Back Pressure

The initial conditions listed in table 4 are based on the results provided by AFRL.[11] Figures 16 through 19 show the static pressure, static temperature, total pressure, and Mach number, respectively, normalized by the reservoir conditions. The plots compare the present CFD results with the AFRL CFD analysis results.

Figure 16 shows that each plot was consistent with the profile of the nozzle, however each plot varied but converged to a final pressure solution. When compared with the results provided by AFRL, the CFD profiles appear to be out of phase. According to past CFD experiments, turbulence intensity and length or the turbulence model itself can shift the location of the pressure profile.[13] This appears consistent with the results as the true turbulence parameters used by AFRL are not listed and SolidWorks does not use the Spalart-Allmaras turbulence model.[13] This can affect the friction of the model which is used to judge whether the Fanno flow is being applied in the model. The pressure appears to slightly rise over the given isolator length, and given the thermodynamic laws, the temperature will rise from the pressure change as well.

The temperature profile displayed in fig. 17 shows the model slowly converging towards the exit profile displayed by AFRL. If the flow data overlapped the AFRL data, the temperature profile may actually have a higher temperature for the same given length.

Figure 18 shows the exit total pressure is lower than the total pressure in the reservoir, which would be consistent with an adiabatic system with friction on the walls. The pressure profile matches the maximum pressure of the AFRL case. However, the pressure near the walls

needs to be refined. With more calculations, it is believed a more pronounced profile could be accurately determined.

Figure 19 shows that the exit Mach profile is higher than what AFRL measured for the no back pressure case. As previously stated with fig. 16, the profile is close to converging towards the solution. However, it appears that the entire profile is shifted, and therefore, compared with the theories of Fanno flow, the length is too short for the friction to slow the flow to the AFRL no back pressure exit condition.

Figure 20 gives a side view pressure profile at the center of the duct and nozzle. It appears the flow is relatively constant or slightly increasing in pressure, which is consistent with fig. 16. Figures 21 through 23 display color contours, which also show the location of the boundary layers and how thick they are relative to the duct height. The boundary layer has a lower Mach number, higher temperature, and lower total pressure relative to the mean flow. The boundary layer can be distinctly seen at close to 50% of the overall length. The temperature and total pressure profiles, show interesting characteristics. Even though the flow is consistent with Fanno flow, the pictures show hints of shock development as the total pressure decreases in each individual area. This area can also be considered a source of error and distortion, as the total pressure appears to return to a higher value, instead of continuously decreasing as what would be expected of airflow crossing shock waves.

D. AFRL Isolator with Back Pressure Ratio of 2.38

The program showed that it was capable to simulate real world conditions; however, it appears the data did not stabilize as shown by fig. 27. The data shown in fig. 27 shows the original test points used to model the flow along the wall. The flow matched the data points at around 1727 iterations. However, the flow began to translate towards the isolator exit at 2896

iterations. Past experiments illustrated how turbulence models can adversely affect the results of CFD experiments.[13] Since the experiment shows a translation of ~1.5 inches and the exact turbulence values were not known, it has been considered that this could be a cause to the translation in the profile.

Figures 28, 29, and 30 show the Mach number, total pressure ratio, and static pressure ratio exit profiles, respectively. The convergence histories of the total pressure at the exit plane, SG_{av} (surface goal average), and for the overall flow field, GG_{av} (global goal average), are shown in Figure 31. If the simulation was allowed to run longer, it is believed that the profile would have developed at the exit towards the indicated experimental conditions. Figure 31 gives an example of how the flow developed as the program computed over time. The SG_{av} total pressure measured how the total pressure varied at the exit as an average value over the entire surface area. The GGav Total Pressure measured the entire flow and averaged the total pressure values. This was done to show how the flow stabilized and gave a precise analysis of the flow.

Figure 32 shows the entire flow and how pressure varied downstream. The nozzle flow remains the same as was demonstrated in fig. 15. As the flow developed downstream inside the isolator, it appears the flow compresses, then expands, and compresses again at what appears to be a normal shock. As the flow accelerates, the expansion waves propagate towards the normal shock. It appears that this allows the compression wave to propagate back towards the isolator.

These mixtures of compression and expansion waves allow for the pressure to stabilize inside the isolator. The exit pressure from the mixture of waves is much higher than the isolator entrance pressure. This flow was prevented from propagating towards the nozzle by the initial compression or shock formed near the entrance. The flow then compresses inside this long distance to form a series of shocks which raise the pressure gradually from the initial shock

downstream. As the pressure begins to stabilize, the shock train begins to translate along the length of the isolator and adjusts to the pressure variance between the entrance and exit.

Figure 33 shows how the boundary layer and shocks form as the shock train forms. As the flow propagates downstream, the boundary layer length increases. Once the shock and compression waves mix, the boundary layer lengths combine to a continuous thickness at the walls. As the flows mix the walls begin to heat from the wall friction and increase the boundary layer thickness.

E. Isolator Scaling

No Back Pressure Results

The data collected from the 1x no back pressure case displays an expansion profile at the exit of the isolator inside the combustor. The no back pressure mesh profile is displayed in fig. 34. It displays where the areas of focus are for the entire flow using the adaptive mesh program. Figure 35 displays the change in Mach number as the flow exits the isolator and goes through the compression-expansion process. The airflow appears go through overexpansion at the exit of the isolator where the walls turn 90º and attempts to stabilize towards equilibrium. The friction induced by the walls appears to slow the flow as it goes downstream, but the flow remains supersonic. The flow outside the expansion region appears to be sonic and then dissipates to equilibrium.

Figure 36 displays the compression waves located at the exit of the isolator. The pressure goes through an oblique shock and matches the static pressure surrounding the jet boundary, then goes through another reflecting shock wave to turn the flow back towards the centerline. However, this pressure is too high relative to the surrounding pressure and must equalize and turn the flow outwards through expansion waves. This process repeats until the flow is stabilized to the surrounding pressure. This pressure increases as the flow decelerates to a stop when the pressure is equal to the boundary conditions listed in table 6.

The flow inside the isolator follows Fanno flow theory by increasing pressure with increasing length. This also results in a decrease in Mach number as shown in fig. 36. The flow is not isentropic as the total pressure decreases as the flow exits the isolator, as displayed in fig. 37. This also supports the Fanno flow theory for adiabatic flow with friction for a constant area duct

with increasing length. The boundary layer can be clearly seen increasing in thickness as the total pressure decreases. The total pressure dissipates after the flow enters the combustor. Figure 38 displays how the static temperature changes with length. The temperature rises due to the friction and the increase in length, and a boundary layer is formed due to the friction and converges. The flow outside the jet is hotter and dissipates into the cooler flow inside the combustor.

PR=2.38 Results for all isolators

Figure 39 displays the mesh for the 1x isolator. The areas of focus for the mesh program were the shock wave and the jet located at the exit of the isolator. The adaptive mesh program refined around the normal shock wave and displayed the data through "shock capturing". The Mach number contour in fig. 40 displays the normal shock at the point where the Mach number is above one on one side and below one on the other side. The display shows the shape of the normal shock to be flat, and on closer observation, appears to be a slight bow in its shape. The shock is thickest near the walls and very thin at the center, as displayed in fig. 40. Fig. 41 displays a pressure contour which also contains a normal shock with no series of shocks afterwards, therefore, no shock trains developed in either figure. The flow, however, appears to accelerate towards the exit with a decrease in pressure. The flow stabilizes at the exit at ~6 psia and near M=0.3.

The total pressure contour displayed on fig. 42 gives a clear indication of how the boundary layer responds to the length of the isolator. The shock wave is located at ~66% of the isolator length from the entrance. The total pressure is constant and increases as the flow crosses the normal shock then decreases below the total pressure value at the entrance. This observation appears to be inconsistent with basic thermodynamic theories. The total pressure should be constant inside the combustor and should not be decreasing as it leaves the isolator. There appears

to be a total pressure build-up from the back pressure as the flow nears the normal shock. A time analysis of this flow would be needed. It appears this normal shock is moving upstream and has not stabilized given the total pressure gradient. This can also be related to the phenomena experienced in airflow disgorgement through the inlet, had the isolator not been present. Figure 43 shows the static temperature profile of the flow inside the isolator. It appears the temperature is constant, before the normal shock. As the flow exits the isolator beyond the shock, the temperature decreases, which is consistent with the Mach profile displayed in fig. 40.

The 10x case was monitored and displayed in fig. 44-49. Figures 44 and 45 give an example of how the adaptive mesh program operates. Figure 44 gives the initial mesh formed before any critical calculations are made to define the flow inside the computational domain. Figure 45 is the end result after capturing the shock and other distortions in the flow. Figure 45 is more refined compared to fig. 44. The mesh from fig. 44 monitored the boundary layer as shown by a finer grid mesh near the walls inside the isolator. The mesh became more refined inside the entire isolator, and more so at the shock wave.

Figure 46 appears to have the same flow characteristics as fig. 40. The boundary layer thickness, however, appears to have decreased with the increase in scale. The formation of the shock appears to be bifurcated compared to the normal shock formed by the 1x case. The boundary layer thickness increases as the flow crosses the shock. The flow behind the shock is subsonic and stops inside the boundary layer. The flow behind the shock appears to decelerate from the exit and develops a boundary layer before approaching the bifurcated shock.

For the flow to decelerate, the pressure must increase. The flow appears to be constant at 8 psia as the flow approaches the shock wave a seen on fig. 47. The pressure rises behind this shock from around 50 psia and decreases to 6-7 psia at the exit. Compared to fig. 41, the pressure profiles appear to be similar and the shock waves are located at 80% of the isolator from the entrance. The total pressure displayed on fig. 48 shows the boundary layer thickness before

crossing the shock wave. The thickness is about 50% of the isolator height compared to the 75% for the 1x case. Once the flow passes through the shock, the total pressure appears to drop more quickly at the center compared to a more uniform total pressure drop observed in the 1x case.

The temperature profile, displayed in fig. 49, shows similarities to the profile of the 1x case. As previously mentioned, in the Mach number and pressure profiles for the 10x case, there appears to be a curvature or bow in the flow formation. The flow is not uniform compared with the flow in the 1x case. The center of the flow also appears cooler compared to the flow inside the boundary layer near the shock. This observation was compared to the findings of the 100x case.

Figure 50 displays the mesh development for the 100x case. The refinement near the shock appears to be in the form of a large bow shock, compared to the more uniform vertical meshes for the 1x and 10x cases. The Mach profile, displayed in fig. 51, shows an extremely thin boundary layer before crossing the shock. The shock can be noticed inside the flow as having a convexity towards the downstream side at the center. There appears to be a thick boundary layer behind the shock which allows the flow at the center to accelerate towards the exit from subsonic to supersonic flow. This normal shock wave appears to be a bifurcated shock which is interestingly located at 80% of the isolator length from the entrance, as seen for the 10x case.

The static pressure displayed in fig. 52 gives a clearer depiction of the bifurcated shock. The flow near the entrance is constant up to the shock. A static pressure rise occurs as the flow passes through the shock and decreases as the flow approaches the exit of the isolator. This change in pressure near the exit is consistent with Mach flow accelerating at the exit. When compared with the 1x and 10x cases, there appears to be a shock structure developing inside the 100x model. The static pressure behind the shock appears to be lower compared to the 1x and 10x cases. In the 100x case, the pressure steadily decreases from 50 psia to about 45 psia. The shock comparison done on fig. 41, 47, and 52 all show how the shock wave changes shape yet maintains location inside the isolator.

In fig. 53, the total pressure profile displays how thick the boundary layer had become once it had reached the shock. The thickness was 25% of the isolator height, an observation consistent with what was observed in the 1x and 10x models. As the scale increased, the boundary layer thickness relative to height decreased (δ/H). The total pressure behind the shock appears to be bifurcated. The total pressure near the walls and center are similar in strength. However where a boundary layer appears to have formed, the total pressure appears to be lower. The overall total pressure appears to have risen as it crosses the shock and then decreases below the level of the total pressure at the entrance. The total pressure behind the shock shows a larger drop near the centerline compared to the 10x case.

The temperature profile displayed in fig. 54 displays the flow occurring behind the shock with better clarity. The temperature is held constant upstream and rises greatly as it crosses the shock. Near the walls behind the shock, boundary layer separation occurs then reattaches to the wall. When compared with the Mach flow from fig. 51, this separation-reattachment phenomenon acts a converging-diverging nozzle inside the isolator, which accelerates the flow to supersonic conditions before exiting the isolator. The lines occurring near the shock at the center of the flow appear to be small normal shocks which could be the signs of a normal shock train developing inside the flow. Further investigation of this flow may be needed before proceeding towards a conclusion that a shock train formed inside the 100x isolator.

Figures 55-58 show the comparisons for the scaled isolators. They display the static pressure of the flow at the center of the isolator as it progresses downstream, as well as the static pressure, temperature and Mach number at x/L=.95 respectively. The flow appears to operate like a Fanno flow with a normal shock inside the isolator. Figure 55 displays the static pressure having a shallow rise linearly, with a sudden rise as it passes through the isolator, and then decreases as it exits the isolator. The pressure value appears to be 2 times the value it had been when it entered the isolator. The difference between the scaled models appears to be minimal.

The only difference is the slope of the pressure change with regard to length and the maximum pressure rise before exiting the isolator. The pressure value for each isolator at the exit appears to converge towards the same value of P_s/P_0=2.13.

However, the exit profiles of each isolator appear to be dramatically different for the static pressure, temperature and Mach number. The static pressure ratio at the exit of the isolator, displayed on fig. 56, appears to approach unity with increasing scale. The static pressure increased to P_s/P_0=0.465, 0.525, and 0.612 for the 1x, 10x, and 100x cases, respectively. These values were constant with respect to height. Figure 57 displays how the temperature profile changes with scale. The flow for the 1x model appears to be constant with a very small boundary layer. As the scale increased, the temperature gradient increased at the center and the overall profile appeared to be out of phase with the 1x case. The 100x model showed an even larger temperature gradient with a near linear increase in temperature toward the center of the isolator. The profile was beyond unity and out of phase with the 1x case.

Figure 58 showed that increasing the scale would decrease the exit Mach number and result in subsonic flow near the exit. Like fig. 57, the change in Mach number as a function of height appeared to increase with increased scaling. The 1x profile showed a near constant Mach number while the 10x case was out of phase with a large difference in Mach number between the center and walls of the isolator. The 100x model showed a near linear change in Mach number from wall to center of the isolator. It also showed the lowest Mach number average compared to the 1x and 10x cases.

IV. Conclusion

A numerical analysis was conducted to study the effects of geometrically scaling scramjet inlet-combustor isolators. The C-D channel validation case was used to determine if Flow Simulation and SolidWorks were viable programs for testing thermodynamic and aerodynamic theories. This was done by comparing the software results to theoretical and analytical data. After this was performed, the AFRL case was used as the next step to determine if the programs were capable of reproducing the results performed by actual wind-tunnel testing by AFRL. Two test were performed, one test with the nozzle and isolator combined, and another test with the nozzle by itself. The isolator was scaled by changing the cross-sectional area and length as this corresponded to the mass flow rate. The 10X and 100X models represented isolators which could capture 10 times and 100 times, respectively, the airflow.

While the numerical simulations did not form shock trains in the isolators as expected, the simulations did show that the boundary layer height decreased relative to the isolator height (75%, 50%, 25%, respectively) as the scale of the isolator increased (1x, 10x, 100x, respectively). While the relative location of the shock in relation to the isolator length remained unchanged as the isolator scale was changed, the formation and shape of the shock waves changed from a normal shock wave, to a bifurcated shock wave, to a normal shock train as the scale of the isolator increased.

Scaling the mass flow rate may be a possible solution towards scaling the isolator. However, there is more which needs to be done to improve in the area of CFD for hypersonic and scramjet experimentations. The experiments failed to show distinct shock trains for the given pressure ratios scales. More work need to be done for 3-D simulations, since the previous CFD models were based on 2-D simulations.

References

[1] Heiser, W. H., and Pratt, D. T., *Hypersonic Airbreathing Propulsion*, AIAA Education Series, AIAA, Washington D.C., 1994, pp. 250–256.

[2] Waltrup, P. J. and Billig, F. S., "Structure of Shock Waves in Cylindrical Ducts," *AIAA Journal*, Vol. 11, No. 10, Oct. 1973, pp. 1404-1408.

[3] Waltrup, P. J. and Billig, F. S., "Prediction of Precombustion Wall Pressure Distributions in Scramjet Engines," *Journal of Spacecraft and Rockets*, Vol. 10, No. 9, Sept. 1973, pp. 620-622.

[4] Stockbridge, R. D., "Experimental Investigation of Shock Wave/Boundary-Layer Interactions in an Annular Duct," *Journal of Propulsion and Powers*, Vol. 5, No. 3, May-June 1989, pp. 346-352.

[5] Carroll, B. F., Dutton, J.C., "Characteristics of Multiple Shock Wave/Turbulent Boundary-Layer Interactions in Rectangular Ducts," *Journal of Propulsion and Power*, Vol. 6, No. 2, March-April 1990, pp. 186-193.

[6] Billig, F. S., Corda, S., Stockbridge, R. D., "Combustor-Inlet Interaction in Scramjet Engines," *APL Technical Review*, Vol. 2, No. 1, Nov. 1990, pp. 118-126.

[7] Lin, P., Rao, G. V. R., O'Connor, G. M., "Numerical Analysis of Normal Shock Train in a Constant Area Isolator," AIAA Paper 91-2162, Sacramento, CA, June 24-26, 1991.

[8] Sullins, G., McLafferty, G., "Experimental Results of Shock Trains in Rectangular Ducts," AIAA Paper 92-5103, Orlando, FL, Dec. 1-4, 1992.

[9] Lin, P., "Geometric Effects on Precombustion Shock Train in Constant Area Isolators," AIAA Paper 93-1838, Monterey, CA, June 28-30, 1993.

[10] Rice, T., "High Aspect Ratio Isolator Performance for Access-to-Space Vehicles," AIAA Paper 2003-7041, Norfolk, VA, Dec. 15-19, 2003.

[11] Lin, K.-C., Tam, C.-J., Jackson, K. R., Eklund, D. R., Jackson, T. A., "Characterization of Shock Train Structures inside Constant-Area Isolators of Model Scramjet Combustors," AIAA Paper 2006-0816, Reno, NV, Jan. 9-12, 2006.

[12] Lin, K.-C., Tam, C.-J., Jackson, K. R., Eklund, D. R., Jackson, T. A., "Effects of Temperature and Heat Transfer on Shock Train Structures inside Constant-Area Isolators," AIAA Paper 2006-0817, Reno, NV, Jan. 9-12, 2006.

[13] Allen, J. B., Hauser, T., Tam, C.-J., "Numerical Simulations of a Scramjet Isolator Using RANS and LES Approaches," AIAA Paper 2007-0115, Reno, NV, Jan. 8-11, 2006.

[14] SolidWorks Flow Simulation 2009 Technical Reference, Software Package, Build 706, Dassault Systémes, 2009.

[15] Anderson, J. D., *Modern Compressible Flow with Historical Perspective*, 3rd ed., McGraw-Hill Higher Education, New York, NY, 2003, pp. 143, 152-157, 167-172, 204.

Appendix

A. Figures and Data Tables

Tables

Table 1. AFRL isolator configurations

Isolator Case	Cross-sectional Shape	Dimension	Interior Surface
I-1	Rectangular	4”(W) x1.5”(H) x 25.75”(L)	0.02” Thick TBC
I-2	Axisymmetric	2.76”(Dia.) x 25.38”(L)	0.02” Thick TBC
I-3	Rectangular	4”(W) x1.5”(H) x 25.75”(L)	0.25” Thick Ceramic Panels

Table 2. Converging-Diverging channel case initial and boundary conditions

Initial Conditions:	Static Pressure (psia)	14.70
	Temperature (ºR)	527.8
	Mach Number	3
Boundary Conditions:	Inlet Mach Number	3
	Inlet Static Pressure (psia)	14.70
	Inlet Temperature (ºR)	527.8
	Exit Static Pressure (psia)	14.70
	Exit Temperature (ºR)	527.8
	Wall conditions	Adiabatic wall

Table 3. Test facility nozzle initial and boundary conditions

Initial Conditions:	Static Pressure (psia)	21.132
	Temperature (ºR)	441.649
	Mach Number	1
Boundary Conditions:	Total Pressure (psia)	40
	Temperature (ºR)	530
	Exit Static Pressure (psia)	6.79
	Exit Temperature (ºR)	319.4
	Wall Roughness (μ-in)	0
	Wall conditions	Adiabatic wall

Table 4. AFRL isolator initial and boundary conditions, no back pressure case

Initial Conditions:	Static Pressure (psia)	10.872
	Temperature (ºR)	371
	Mach Number	1.55
Boundary Conditions:	Inlet Total Pressure (psia)	40
	Inlet Temperature (ºR)	530
	Exit Static Pressure (psia)	10.872
	Exit Temperature (ºR)	371.0
	Wall Roughness (μ-in)	0 in nozzle, 520 in isolator
	Wall Temperature (ºR)	510

Table 5. AFRL isolator initial and boundary conditions, PR=2.38

Initial Conditions:	Flow Type	Turbulent
Boundary Conditions:	Inlet Total Pressure (psia)	40
	Inlet Temperature (ºR)	530
	Exit Static Pressure (psia)	18.860
	Exit Temperature (ºR)	456.0
	Wall Roughness (μ-in)	0 in nozzle, 520 in isolator
	Wall Temperature (ºR)	510

Table 6. 1x isolator geometry with entrance and exit conditions

1x Isolator Geometry	h_I (in.)	1
	w_I (in.)	2.67
	l_I (in.)	20
	h_B (in.)	13
	w_B (in.)	16
	l_B (in.)	10
	AR_B	1.231
	HR_{I-B}	0.0769
	LH_{I-B}	2
	LR_B	0.769
	AR_I	2.67
	A_I (in^2) (cross-sectional)	2.67
Entrance Conditions	γ for air	1.4
	P_{0i} (psia)	40
	P_i (psia)	6.96
	T_0 (ºR)	530
	T_i (ºR)	321
	M_i	1.8
	Inlet mass flow rate (slug/s)	0.0532
Exit Conditions	Exit mass flow rate (slug/s)	0.0559
	P_{0b} (psia) (averaged)	29.9
	P_b (psia)	18.86
	T_b (ºR) (averaged)	458
	M_b (averaged)	0.835

Table 7. 10x isolator geometry with entrance and exit conditions

h_{10I} (in.)	3.16
w_{10I} (in.)	8.43
l_{10I} (in.)	63.2
A_{10I} (in^2) (cross-sectional)	26.67
AR_I	2.67
h_{10B} (in.)	41.1
w_{10B} (in.)	50.6
l_{10B} (in.)	31.6
Inlet mass flow rate (slug/s)	0.532
Exit mass flow rate (slug/s)	0.559

Table 8. 100x isolator geometry with entrance and exit conditions

h_{100I} (in.)	10.00
w_{100I} (in.)	26.67
l_{100I} (in.)	200
A_{100I} (in^2) (cross-sectional)	267
AR_I	2.67
h_{100B} (in.)	130
w_{10B} (in.)	160
l_{100B} (in.)	100
Inlet mass flow rate (slug/s)	5.32
Exit mass flow rate (slug/s)	5.59

Figures

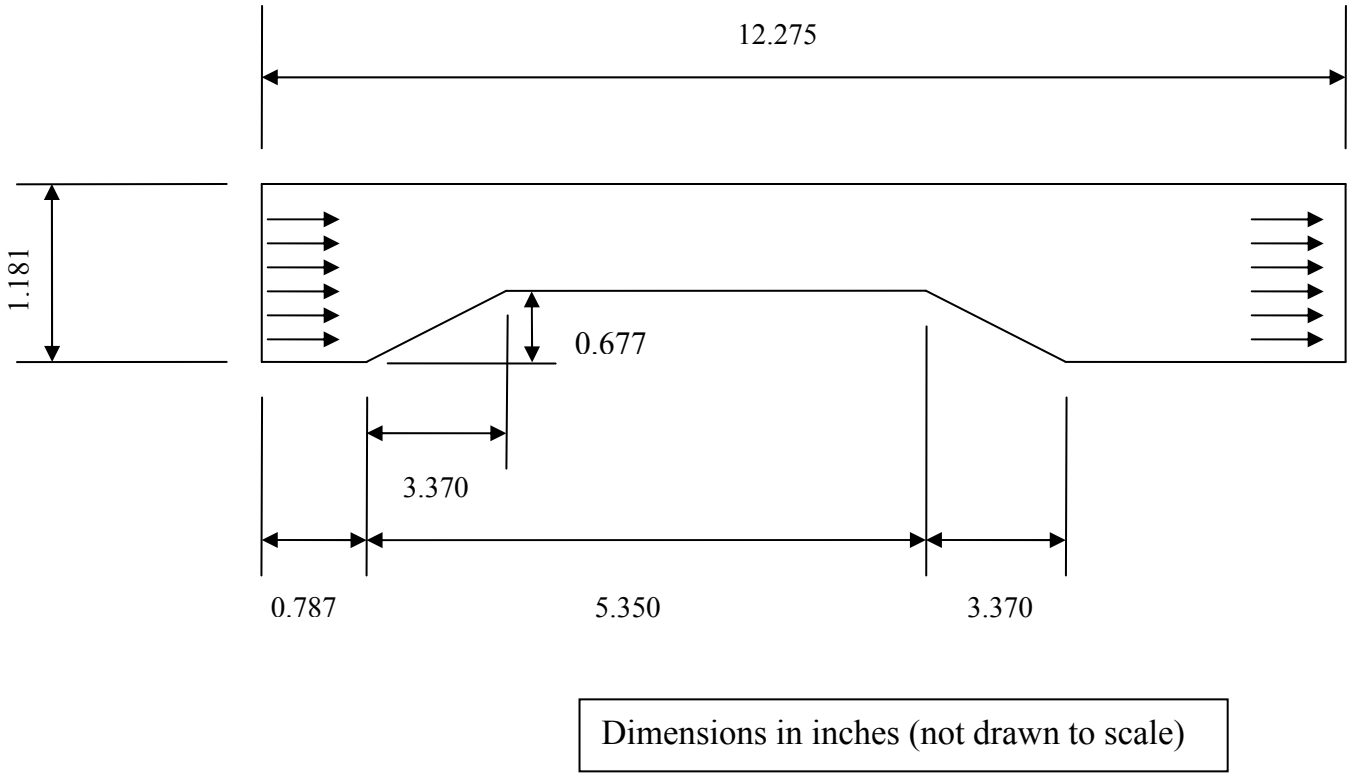

Fig. 1 Converging-diverging channel schematics

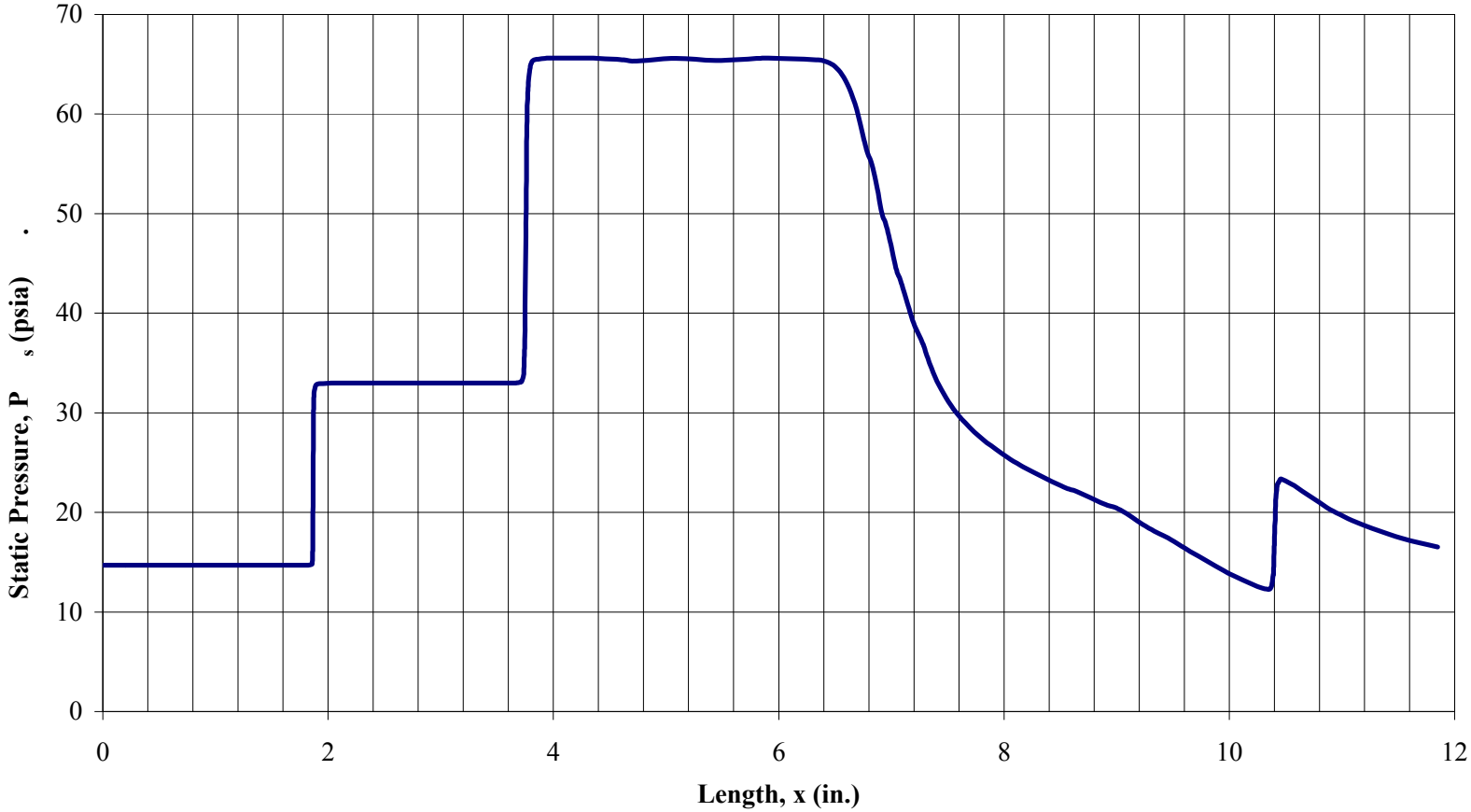

Fig. 2 Static pressure profile for converging-diverging duct

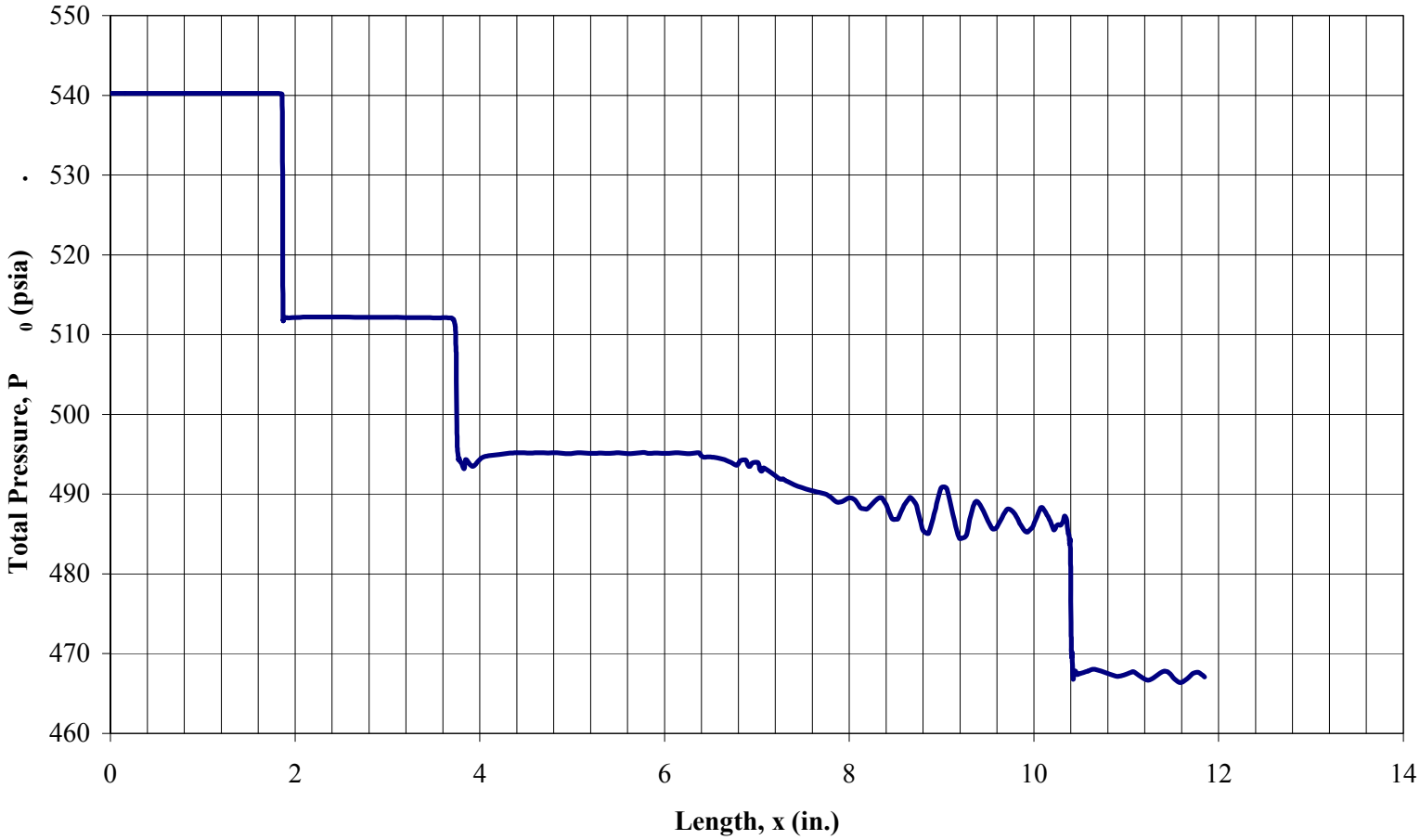

Fig. 3 Total pressure profile for converging-diverging duct

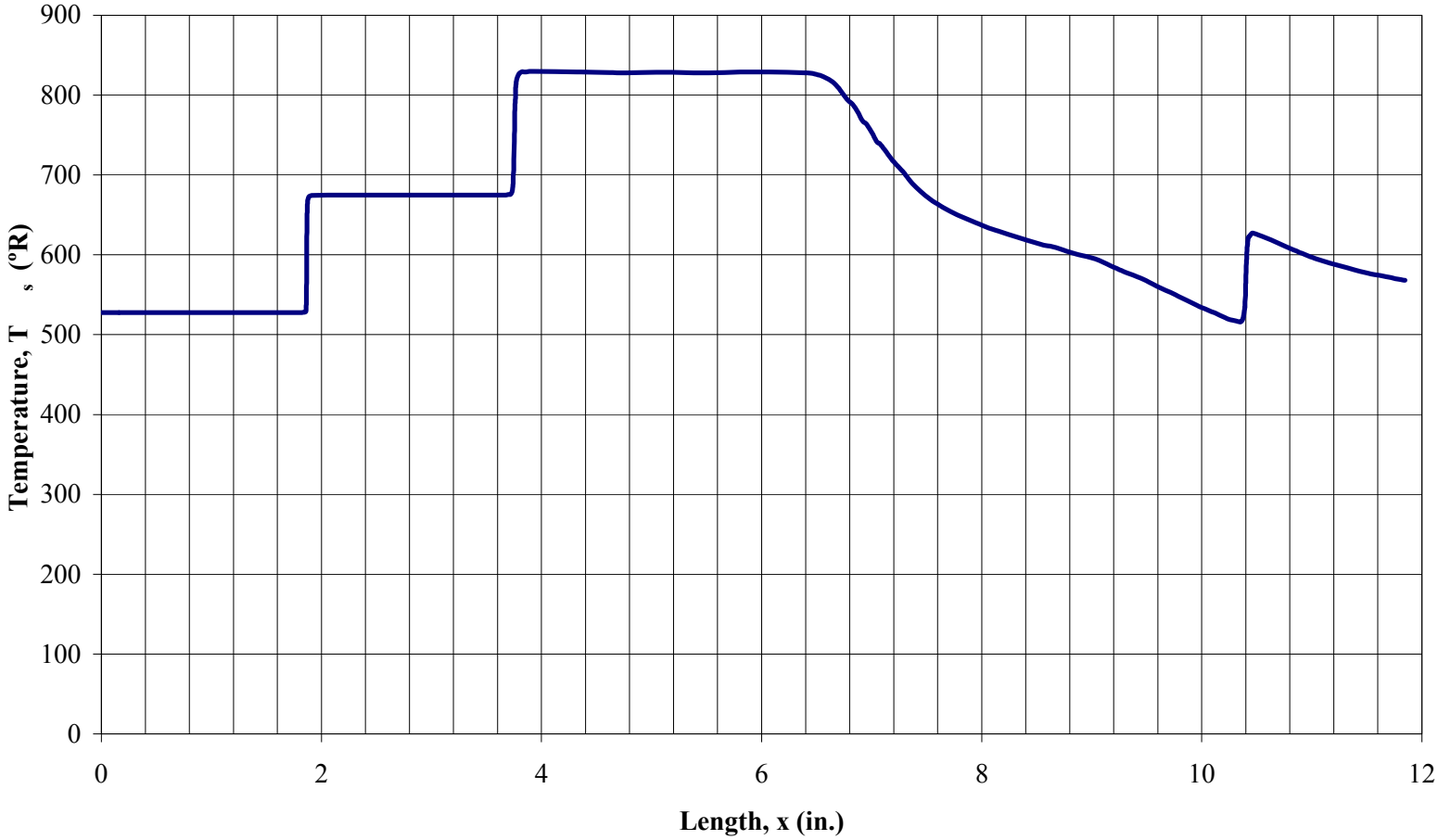

Fig. 4 Static temperature profile for converging-diverging duct

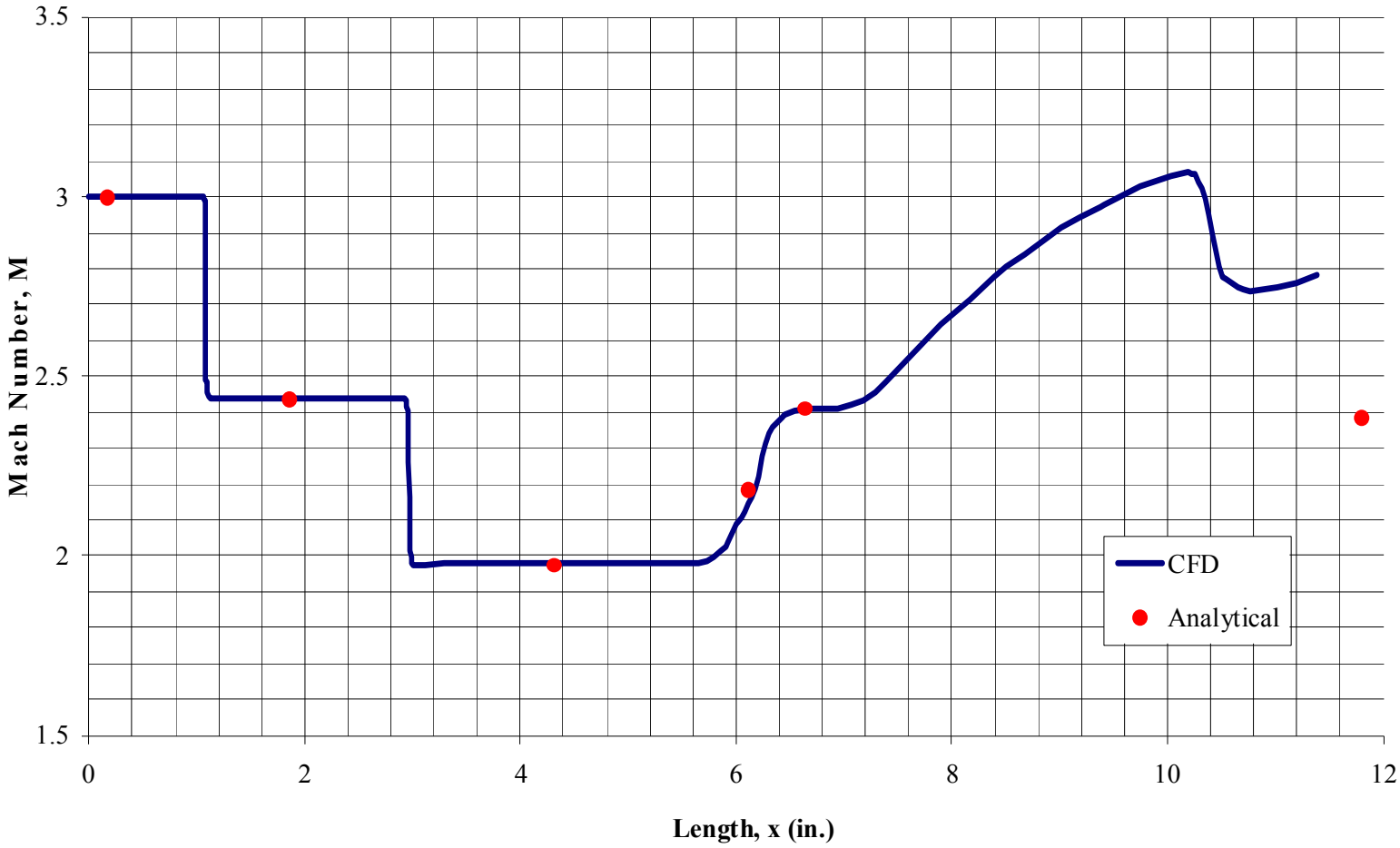

Fig. 5 Comparison of CFD Mach number distribution with theory for converging-diverging duct

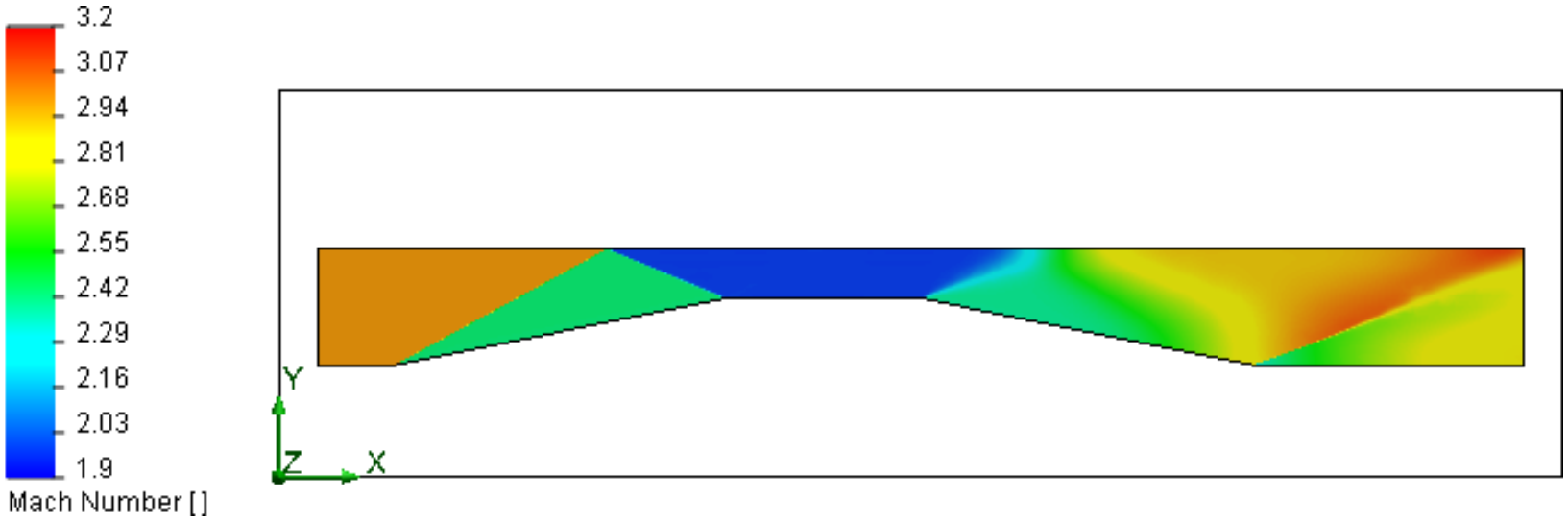

Fig. 6 CFD Mach contour for converging-diverging duct

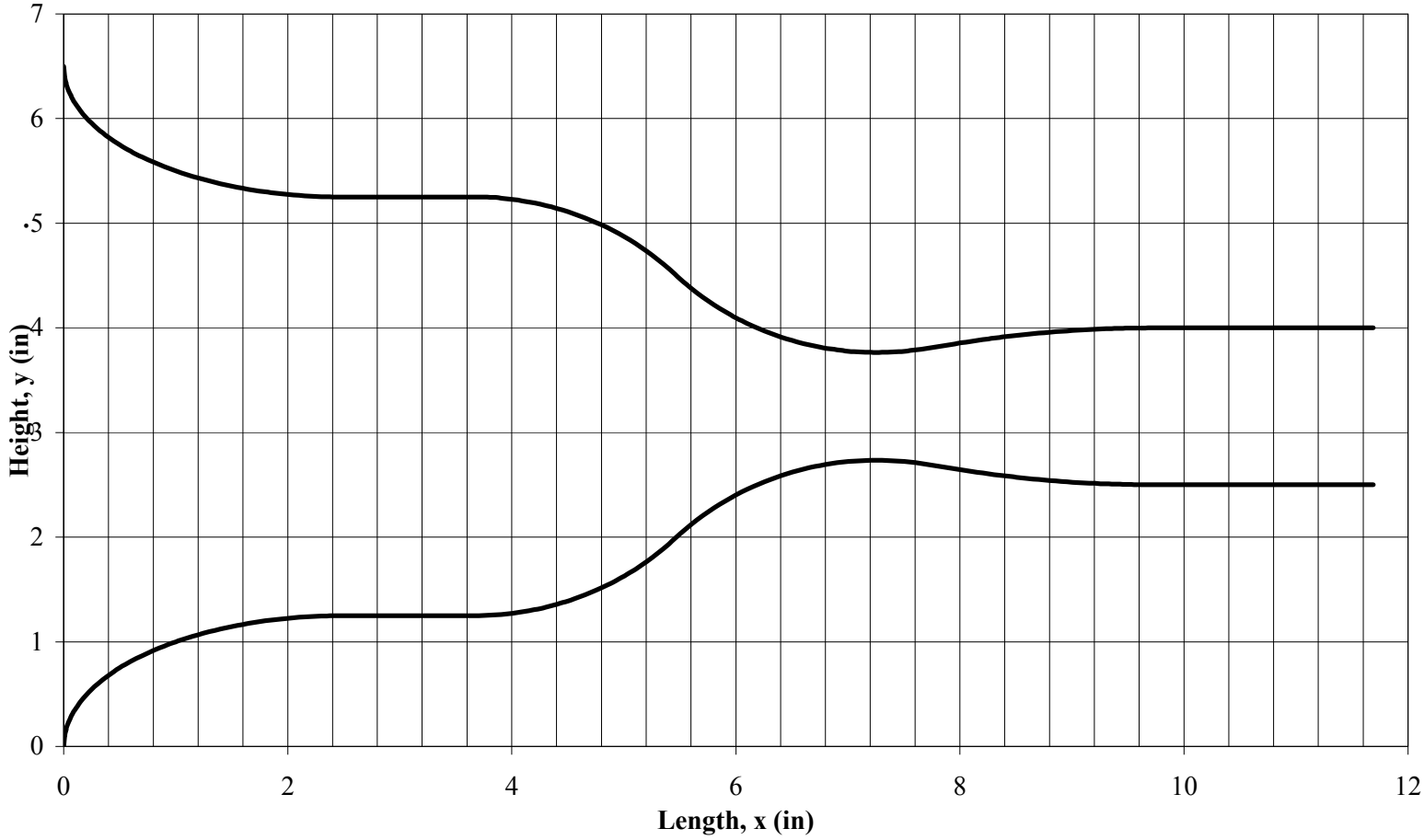

Fig. 7 Test facility, two-dimensional nozzle profile

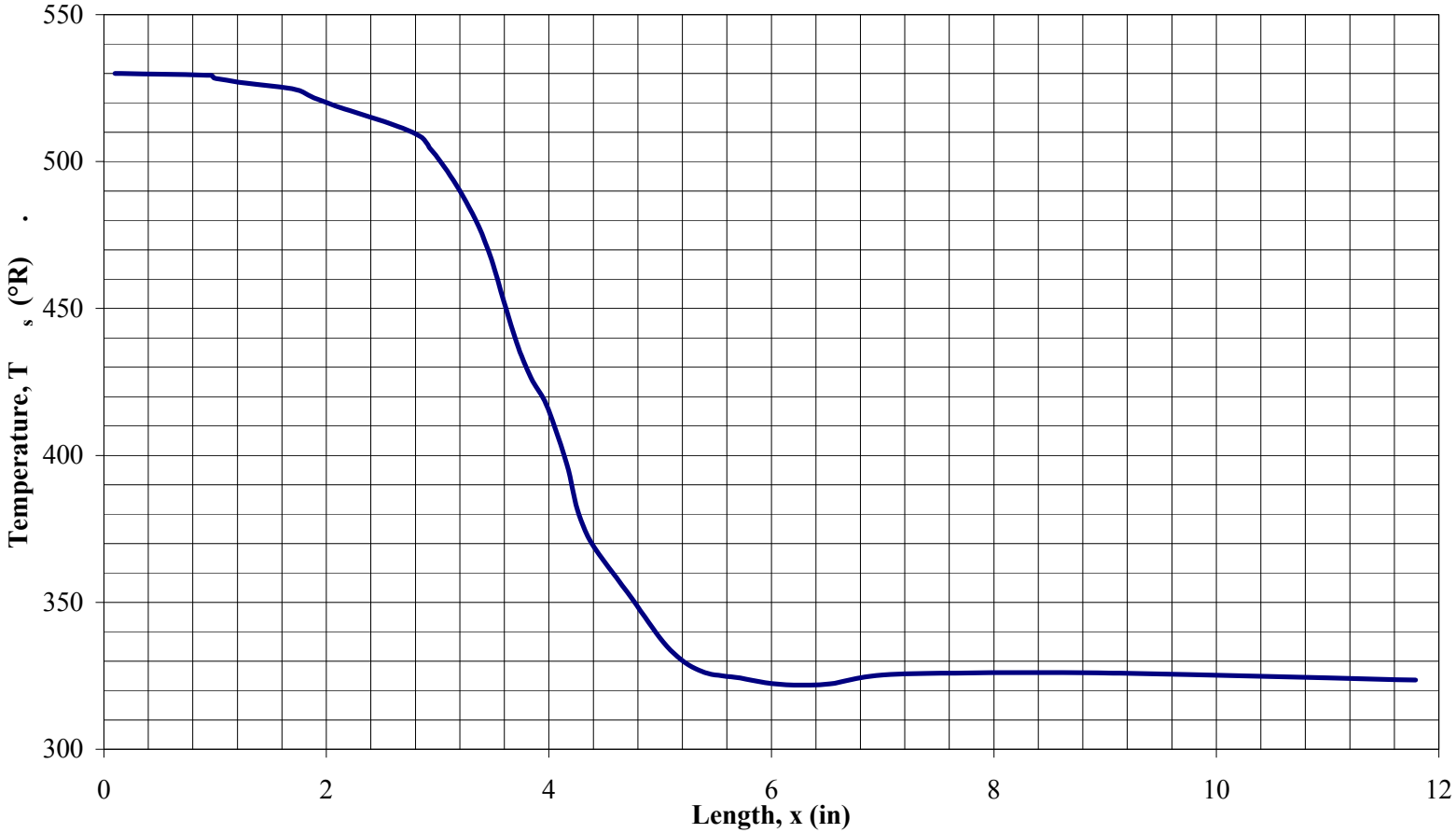

Fig. 8 Static temperature distribution along nozzle centerline

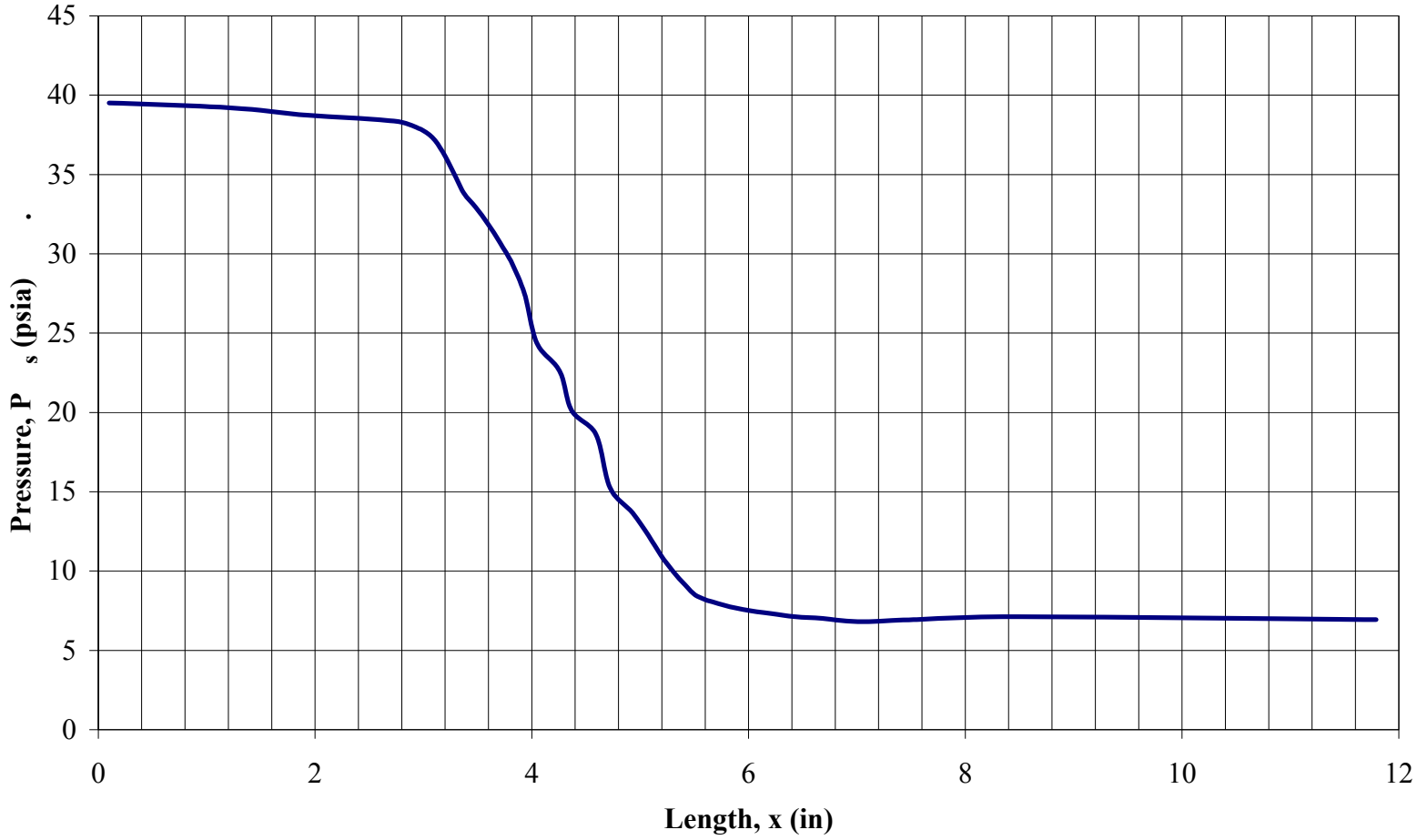

Fig. 9 Static pressure distribution along nozzle centerline

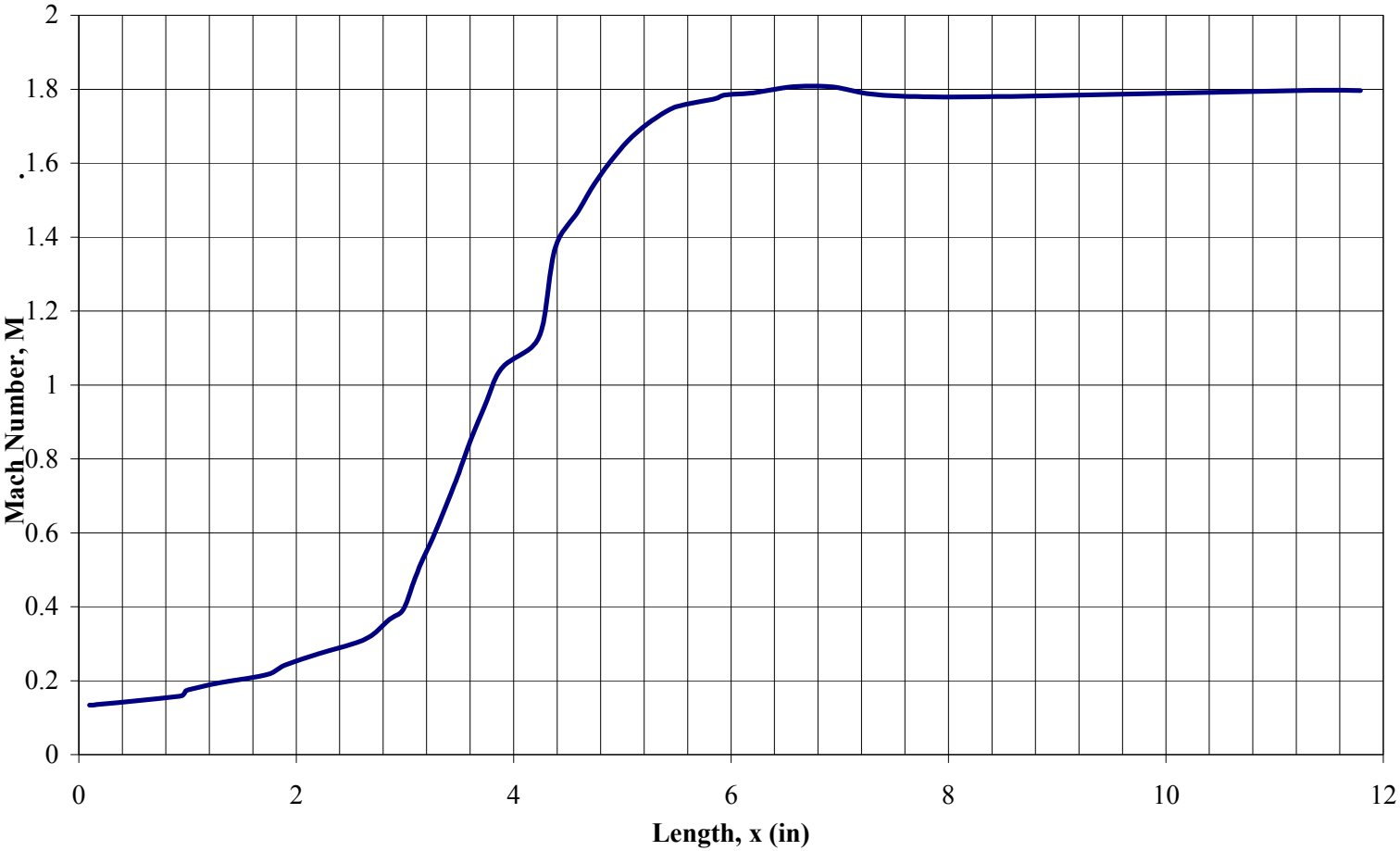

Fig. 10 Mach number distribution along nozzle centerline

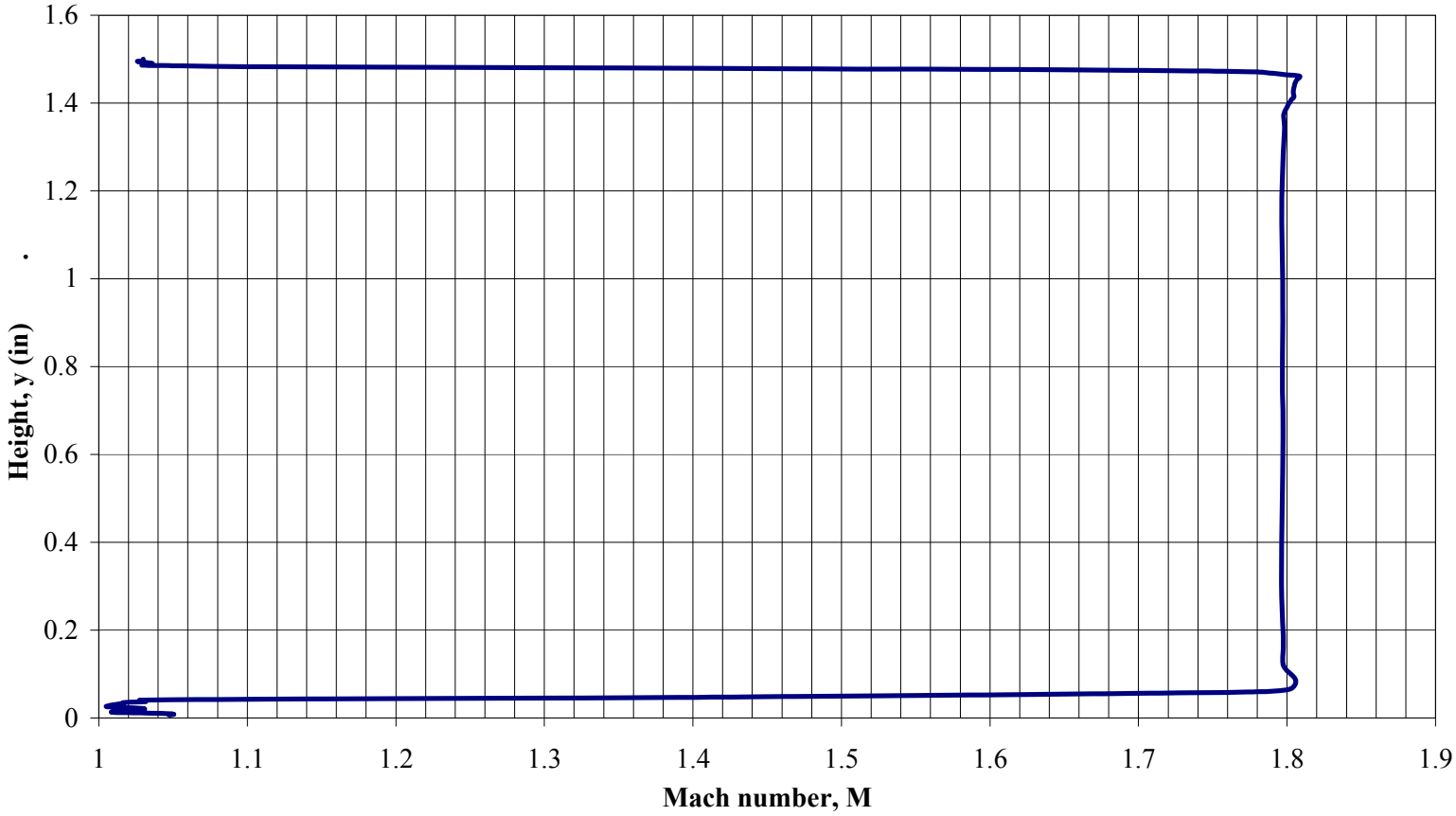

Fig. 11 Nozzle exit Mach number profile

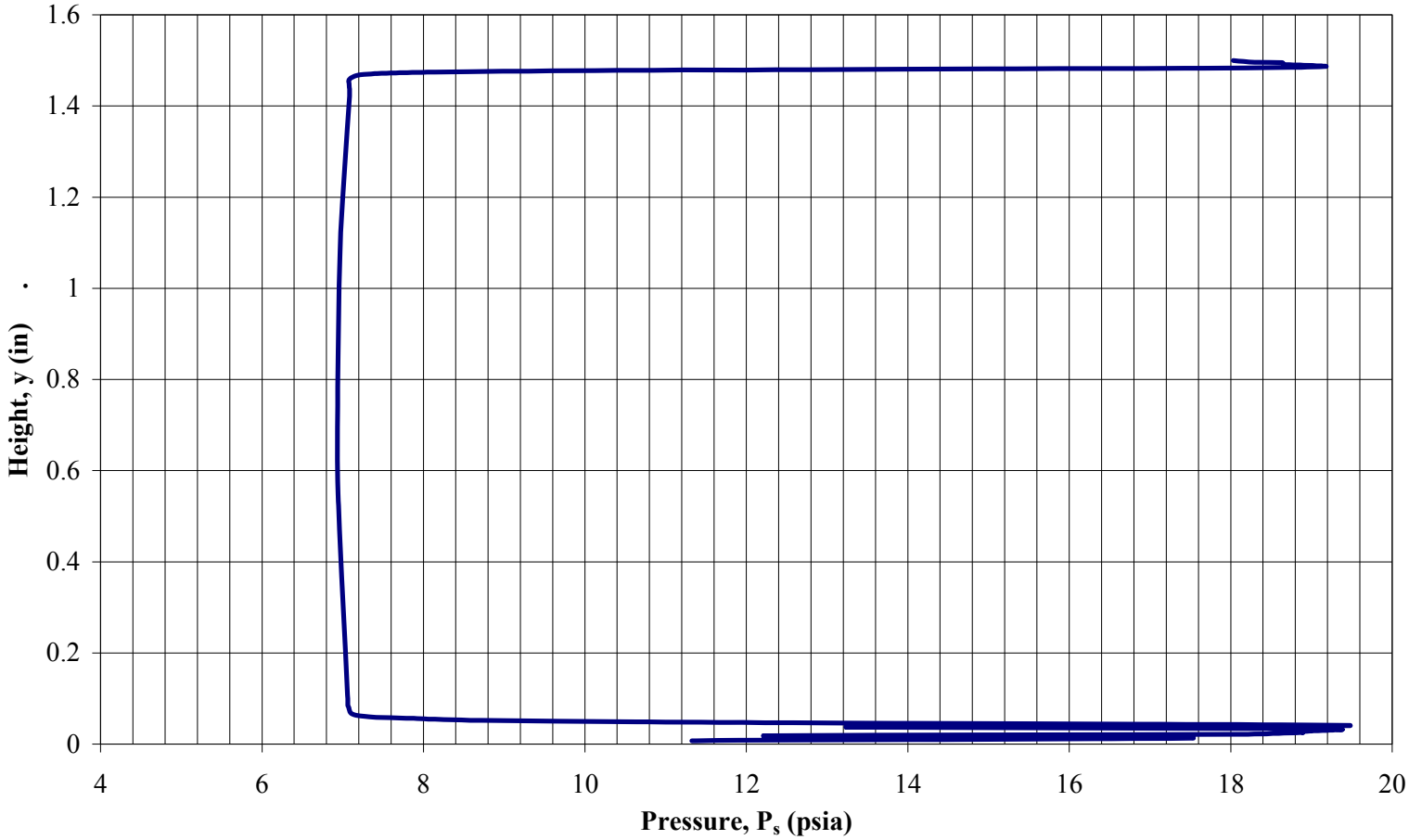

Fig. 12 Nozzle exit static pressure profile

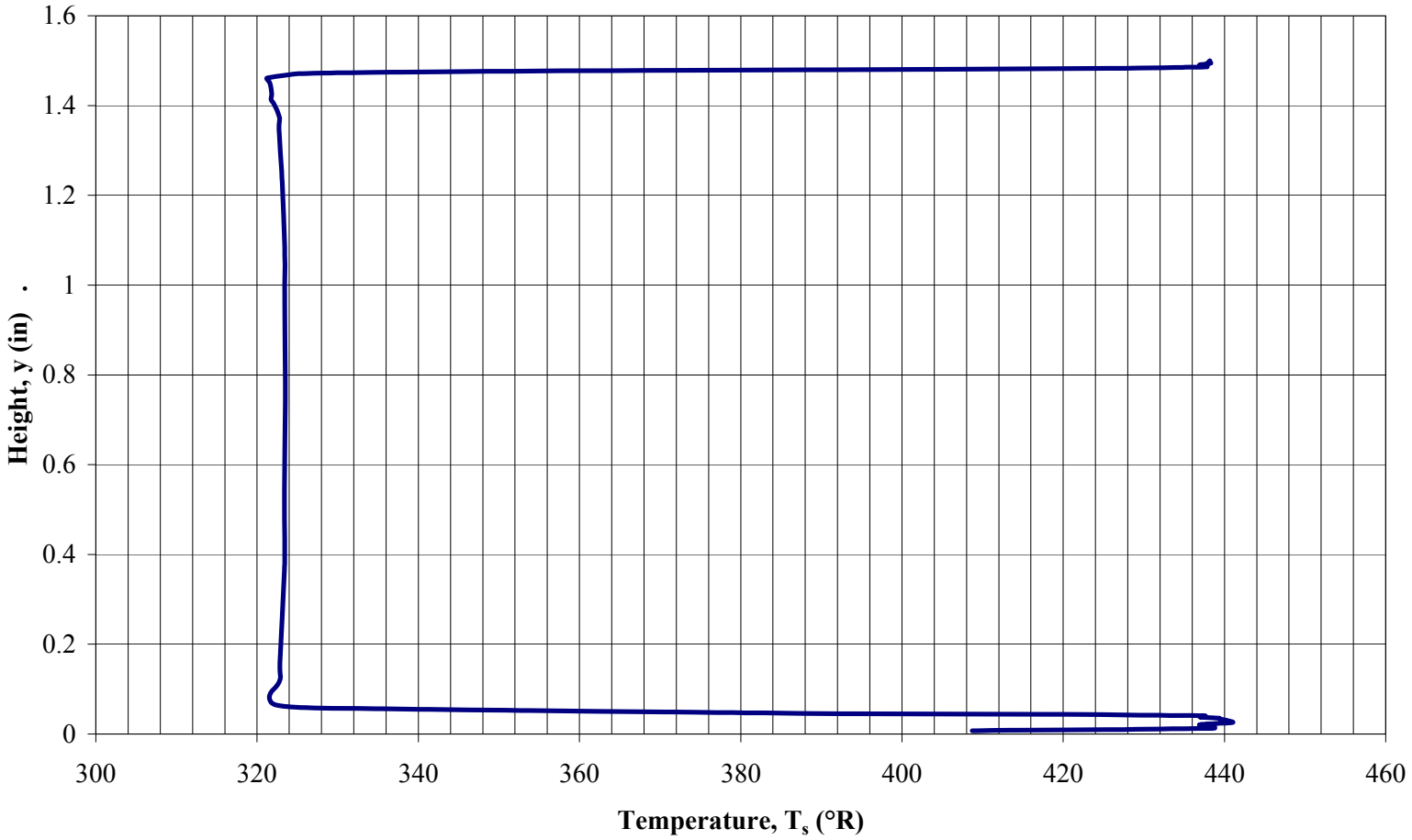

Fig. 13 Nozzle exit static temperature profile

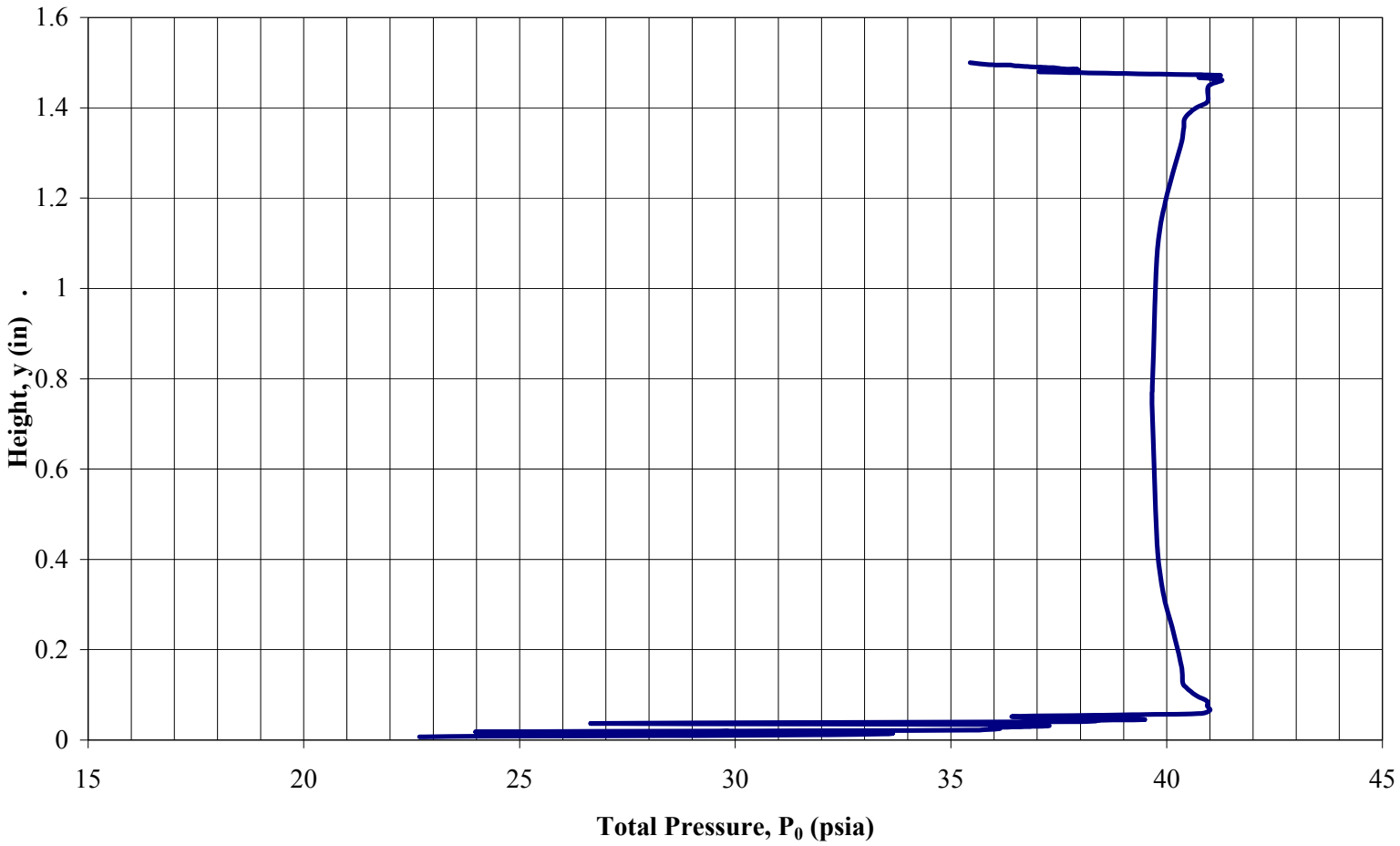

Fig. 14 Nozzle exit total pressure profile

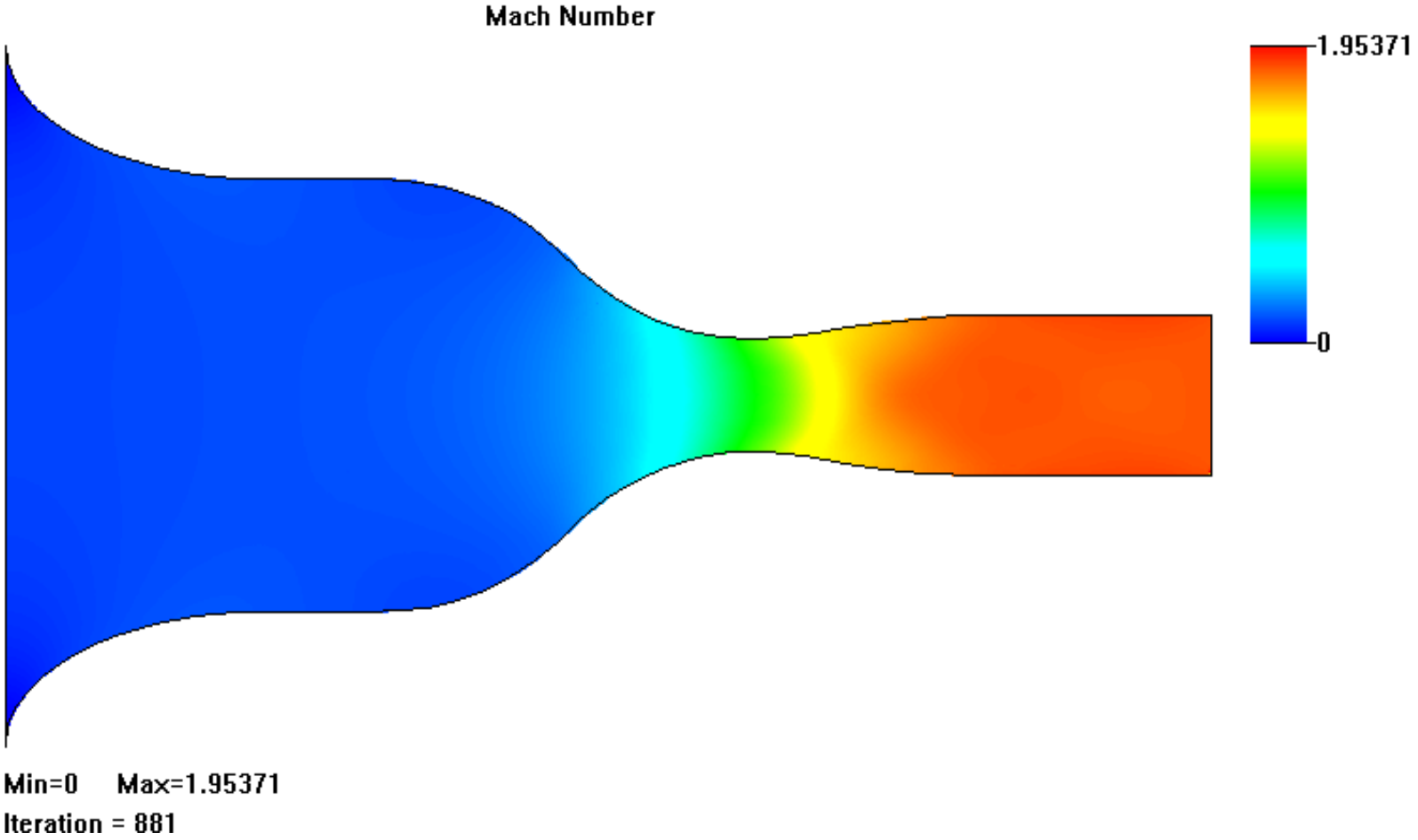

Fig. 15 Nozzle Mach number contours from CFD

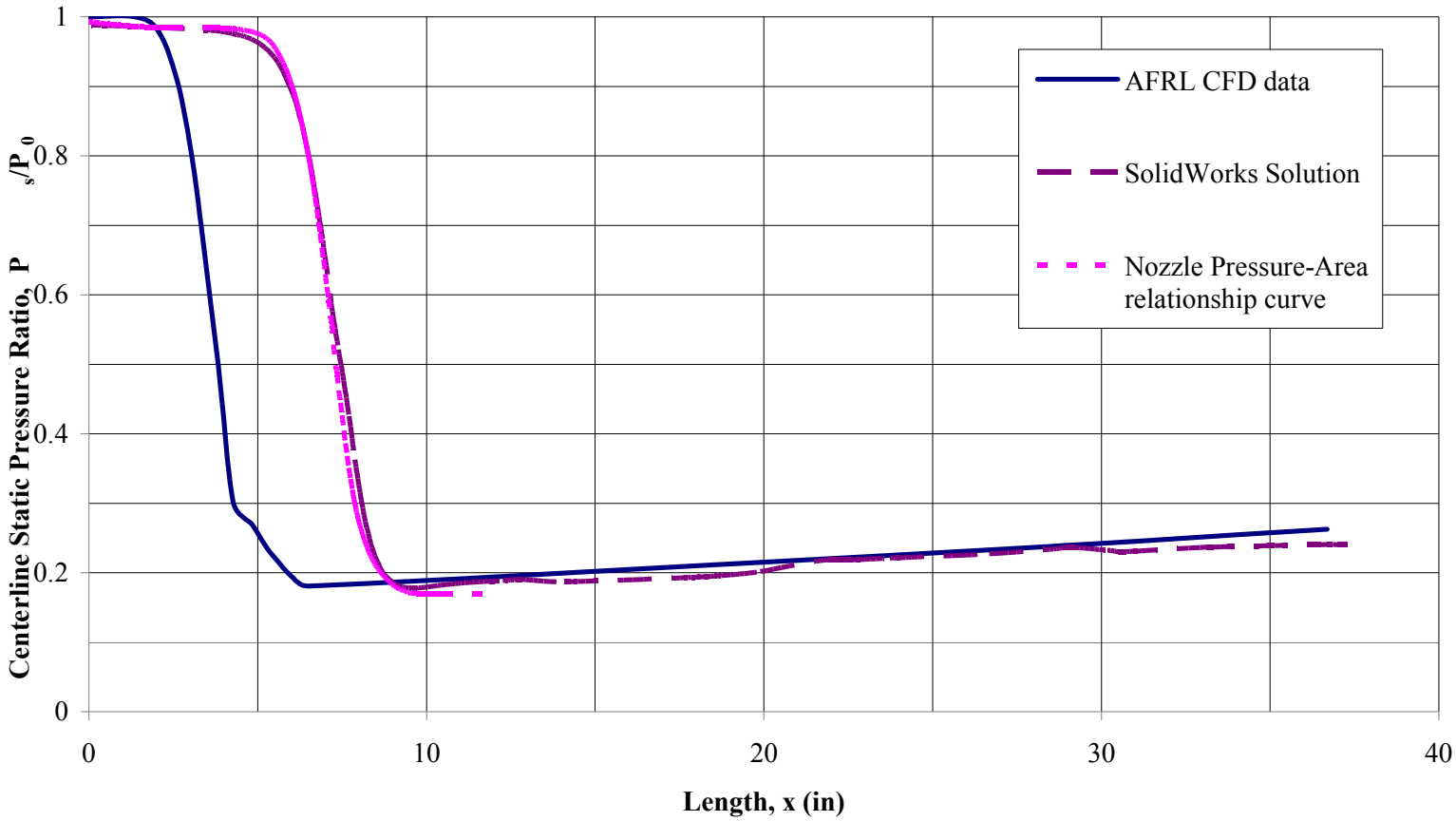

Fig. 16 Centerline static pressure distribution comparison for nozzle-isolator no back pressure case

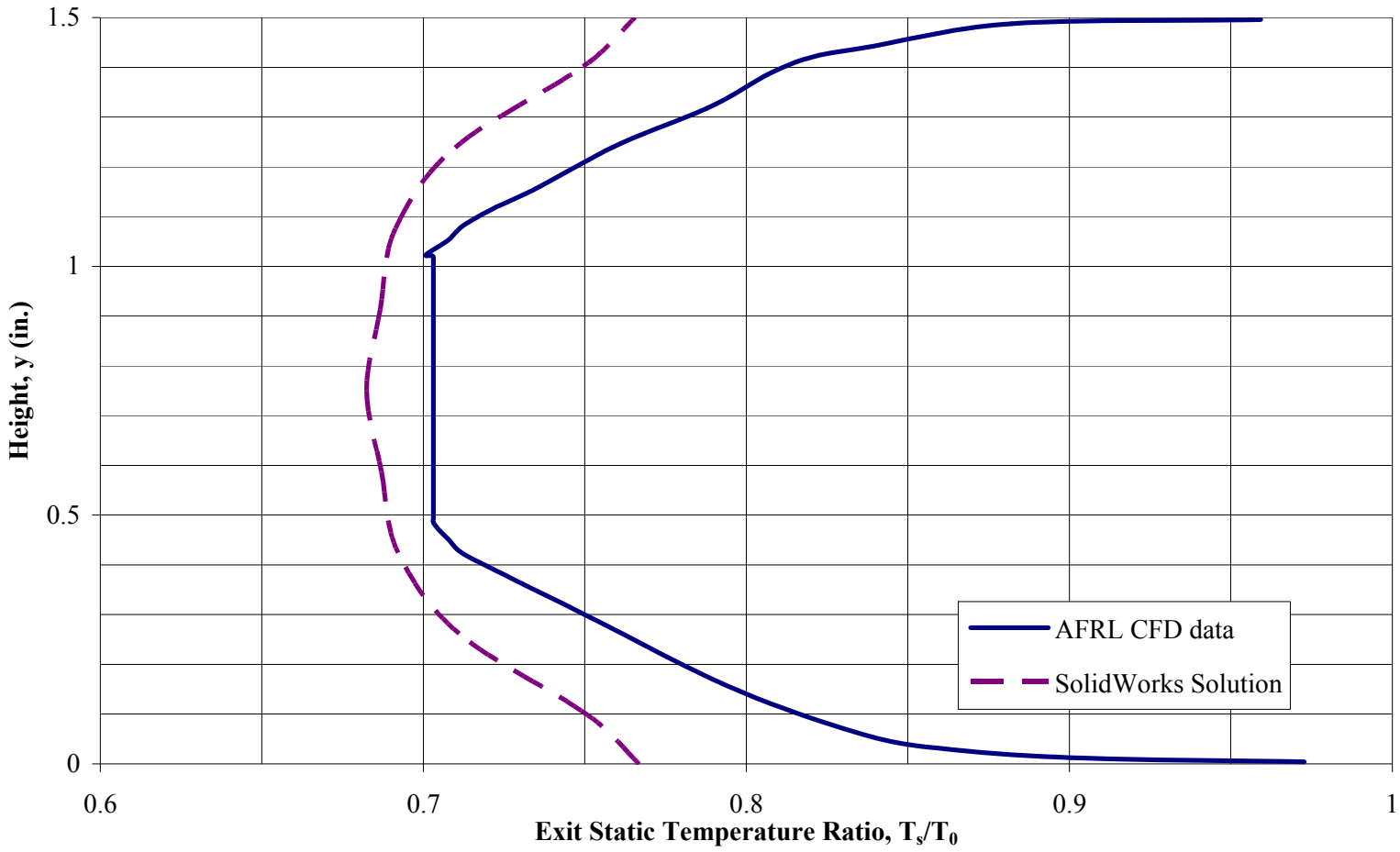

Fig. 17 Exit static temperature comparison for nozzle-isolator no back pressure case

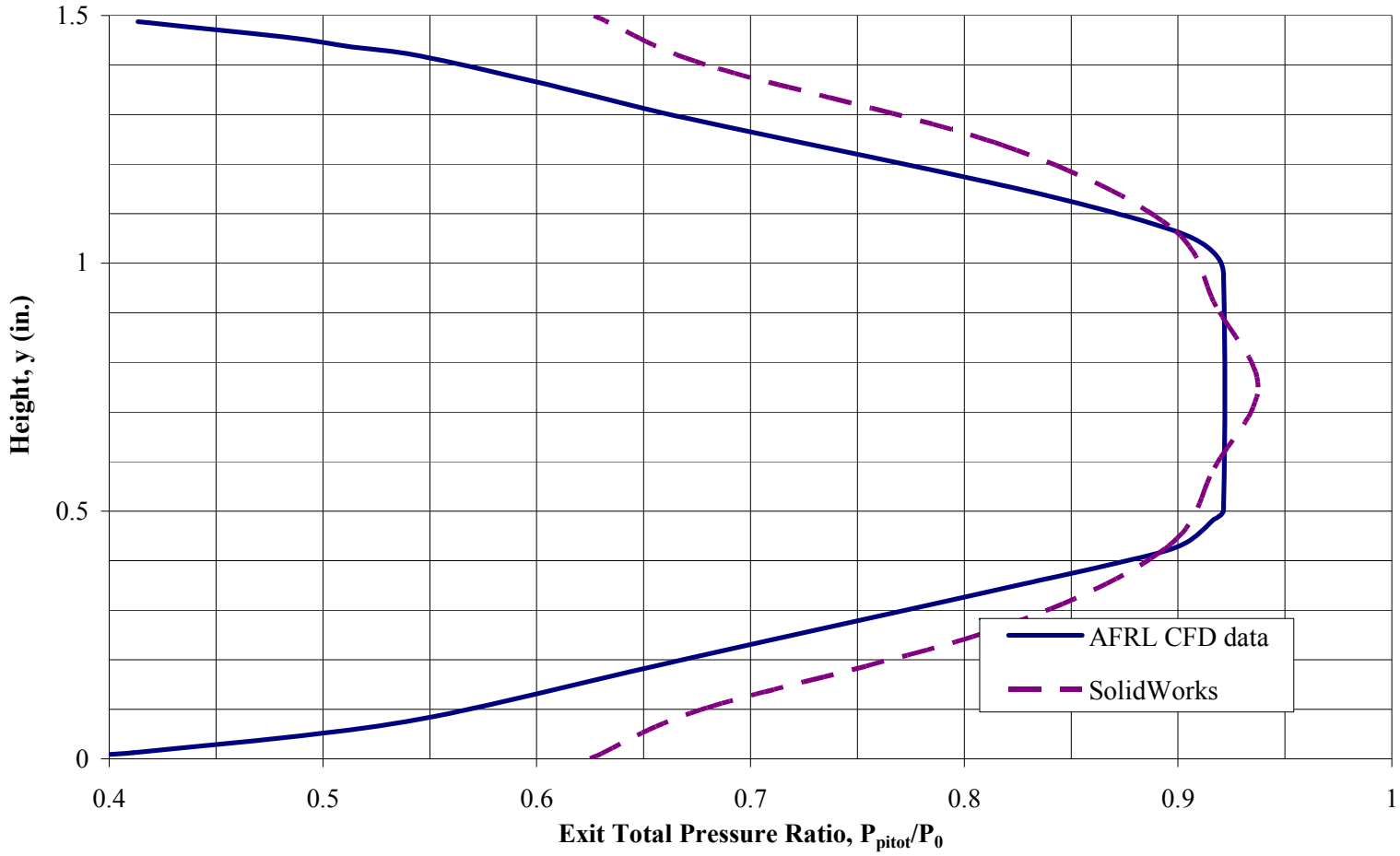

Fig. 18 Exit total pressure comparison for nozzle-isolator no back pressure case

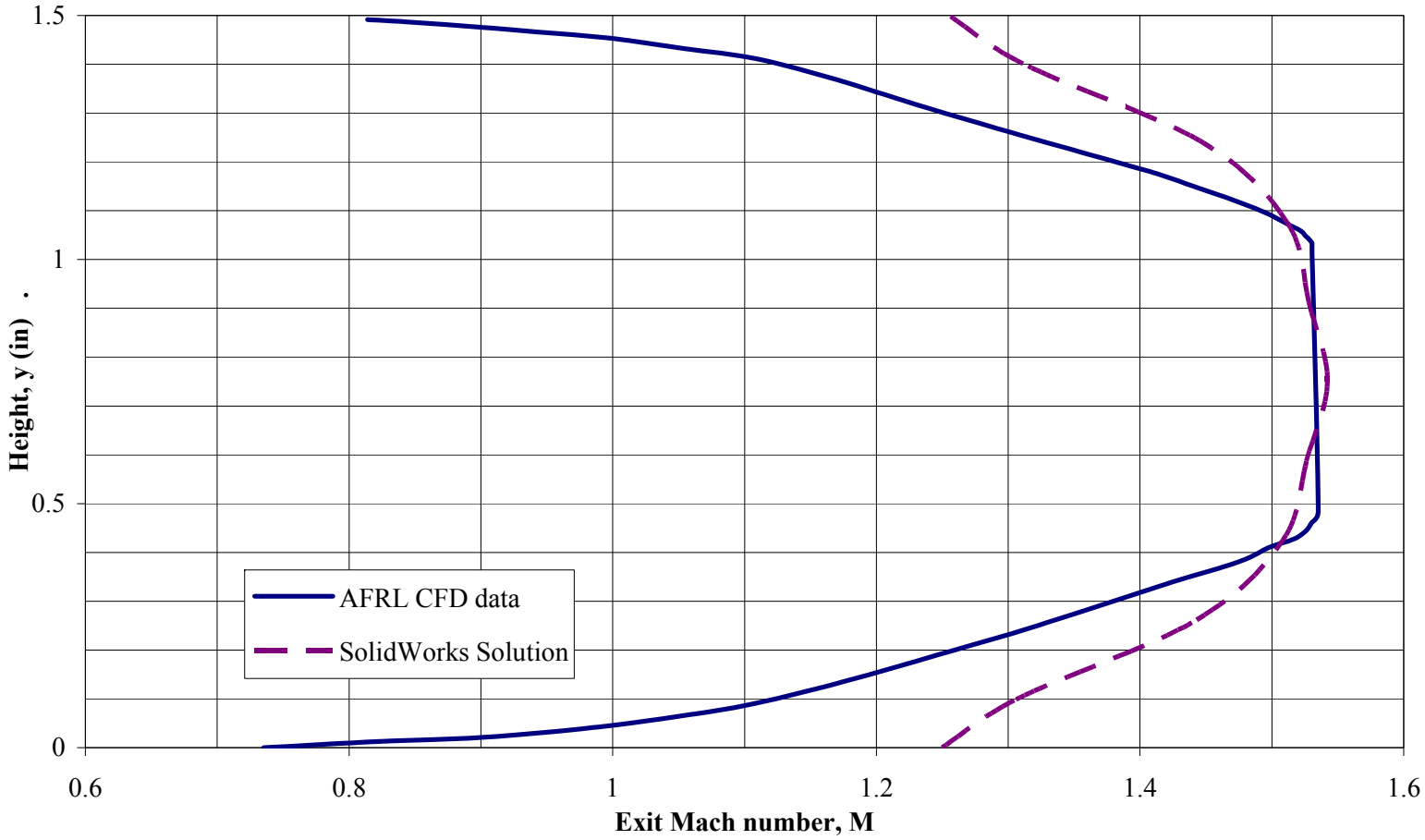

Fig. 19 Exit Mach number comparison for nozzle-isolator no back pressure case

a)

b)

Fig. 20 CFD solution for static pressure, no back pressure case: a) 138 iterations, b) 225 iterations

c)

d)

Fig. 20, Cont. CFD solution for static pressure, c) 366 iterations, d) 861 iterations

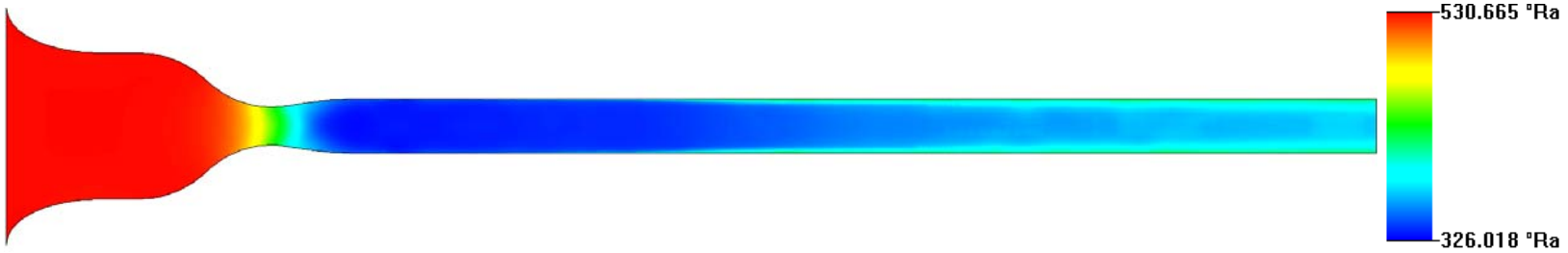

Fig. 21 CFD solution for static temperature, no back pressure case, 861 iterations

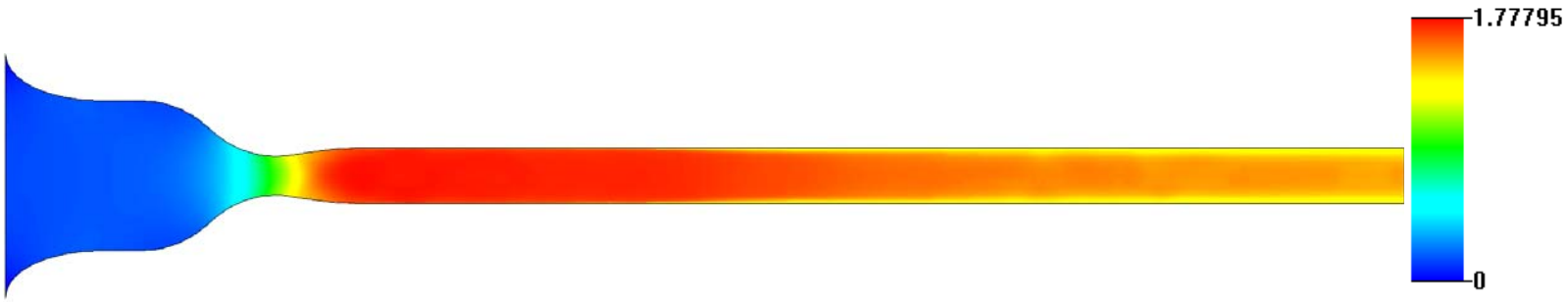

Fig. 22 CFD solution for Mach number, no back pressure case, 861 iterations

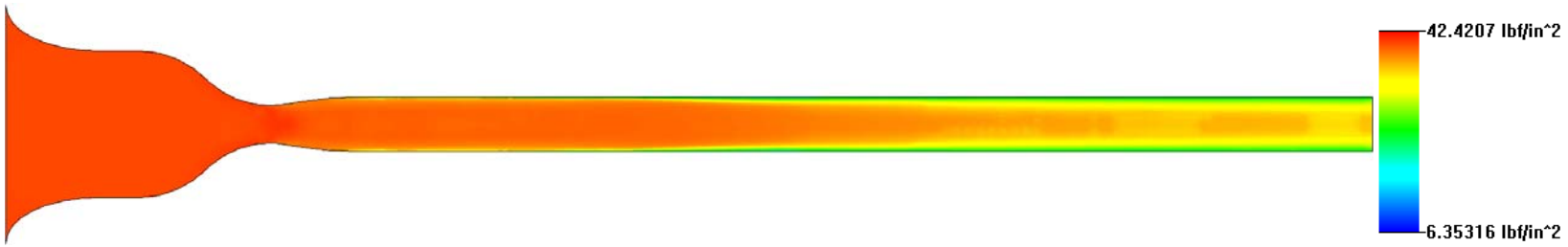

Fig. 23 CFD solution for total pressure, no back pressure case, 861 iterations

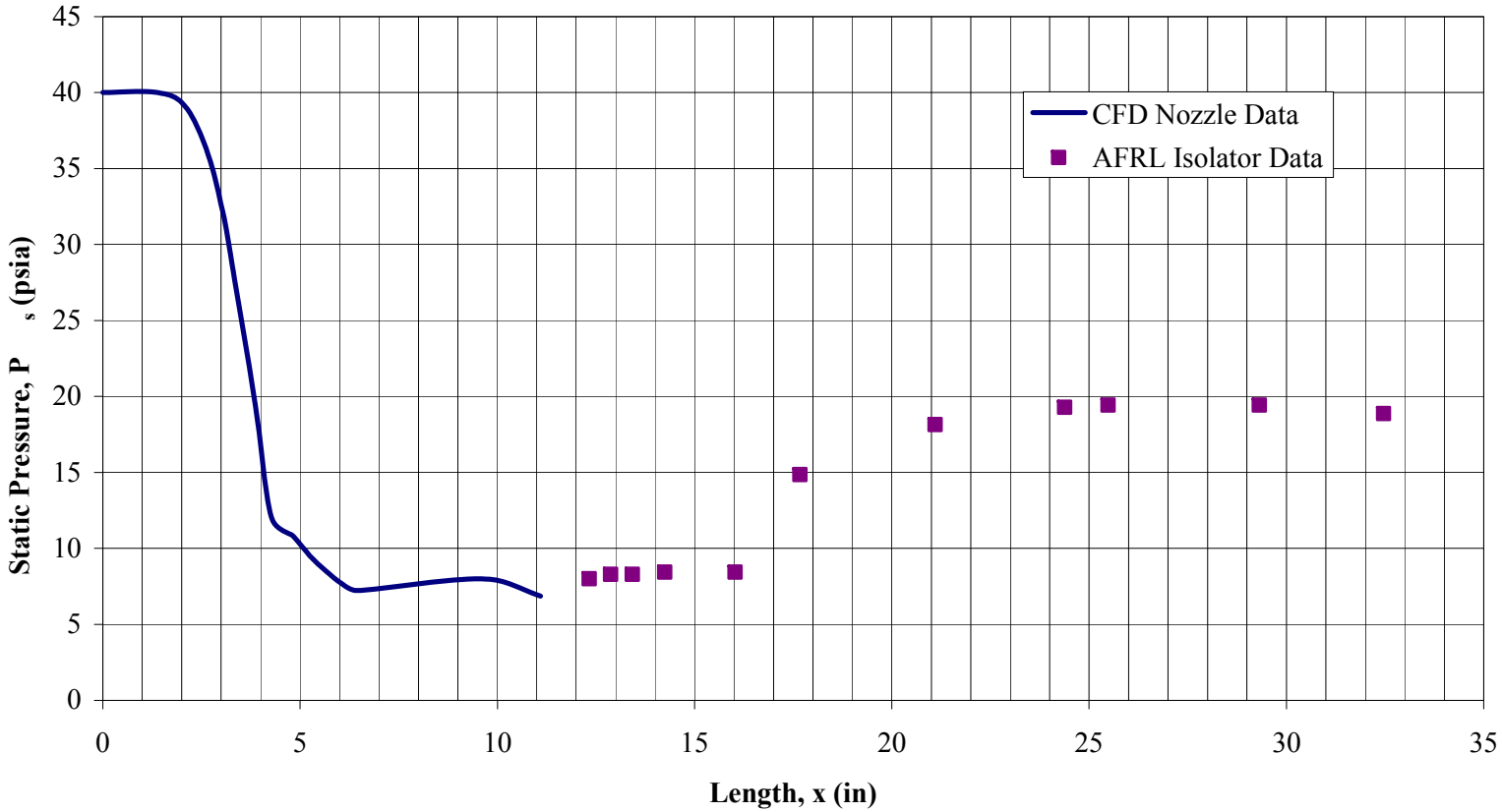

Fig. 24 AFRL pressure profile for a PR=2.38 isolator

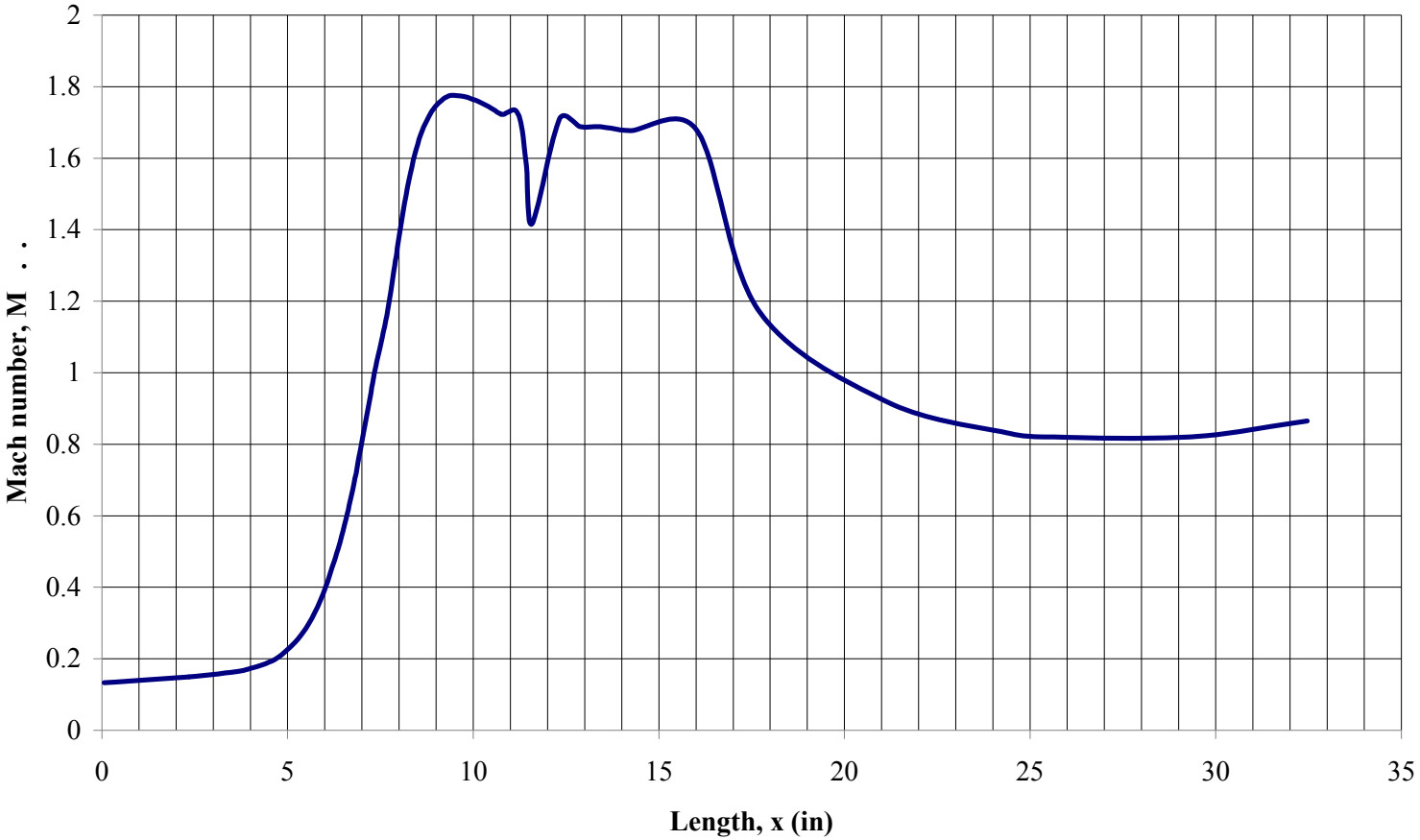

Fig. 25 Assumed AFRL Mach number profile for a PR=2.38 isolator

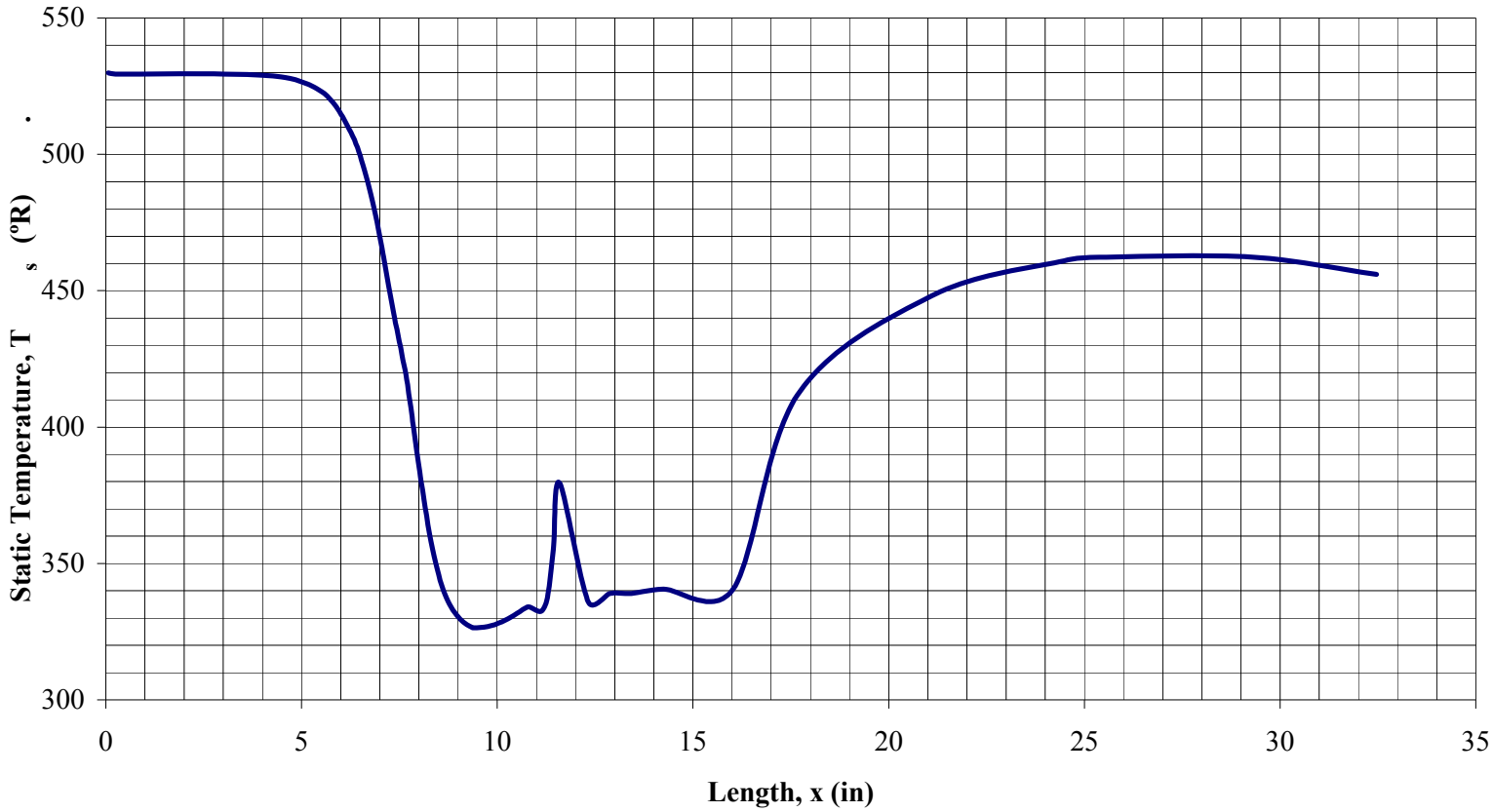

Fig. 26 Assumed AFRL static temperature profile for a PR=2.38 isolator

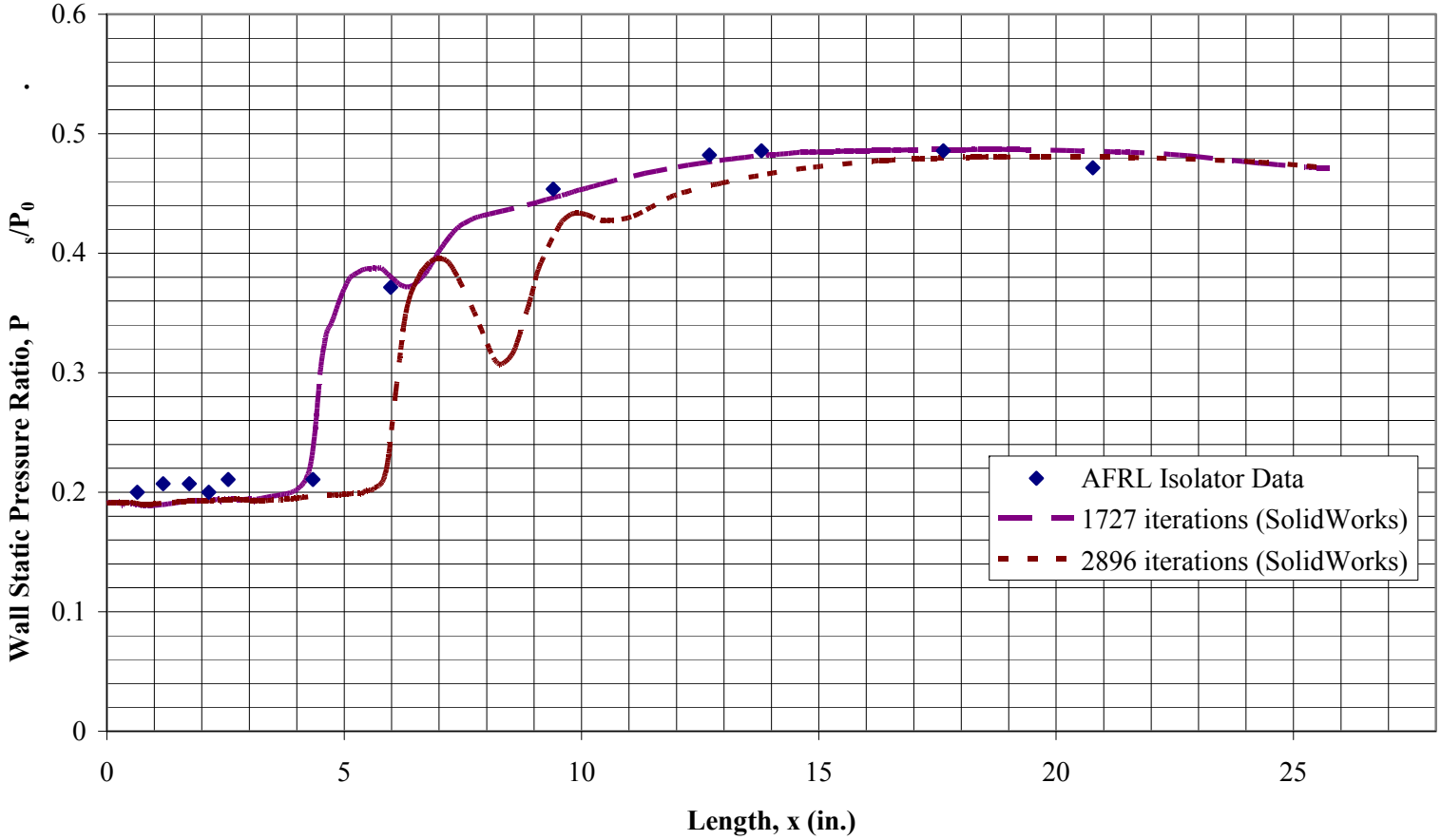

Fig. 27 Comparison of CFD solution and wind tunnel data for isolator wall static pressure distribution, PR=2.38

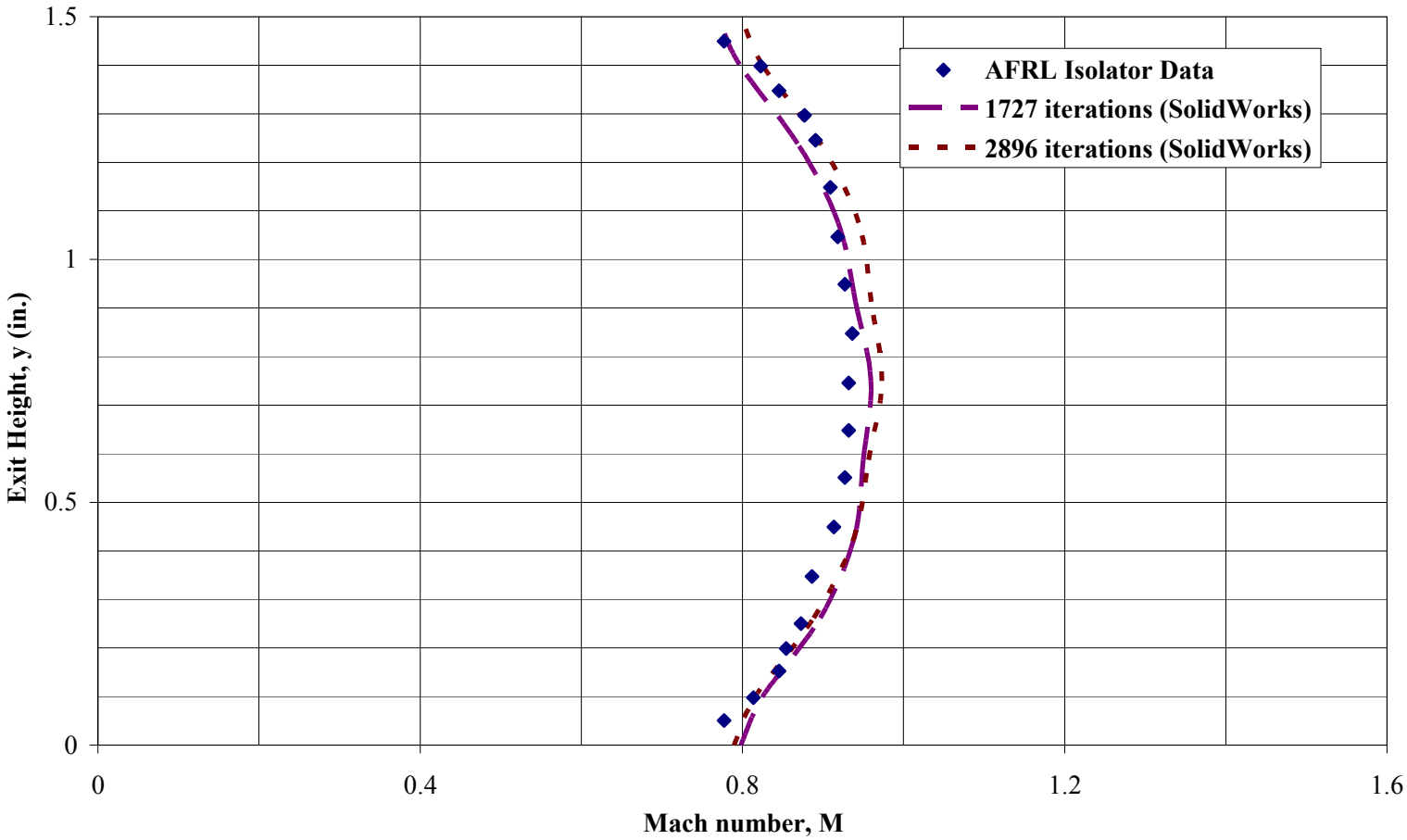

Fig. 28 Comparison of CFD solution and wind tunnel data for exit Mach number profile, PR=2.38 isolator

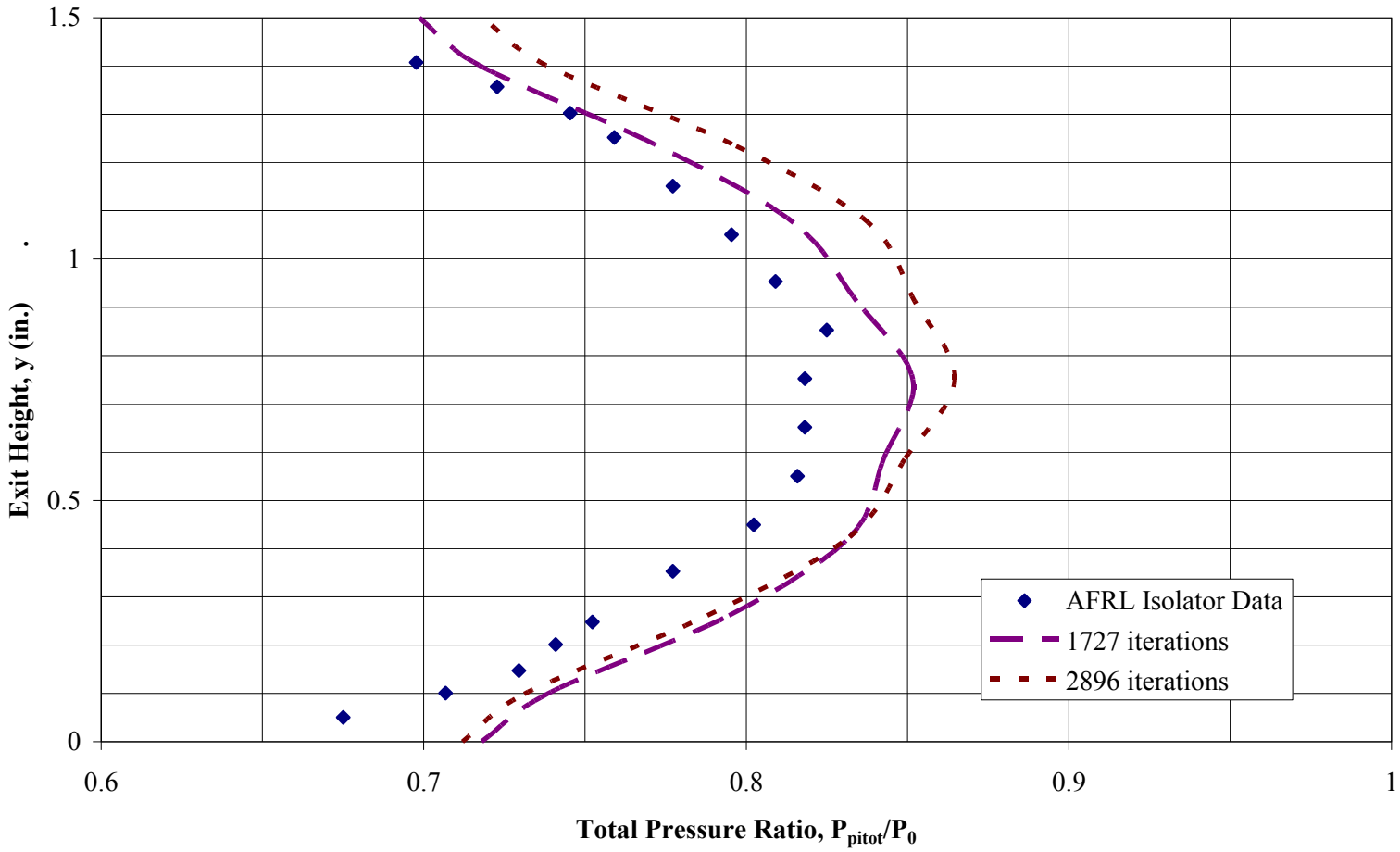

Fig. 29 Comparison of CFD solution and wind tunnel data for isolator exit total pressure distribution, PR=2.38

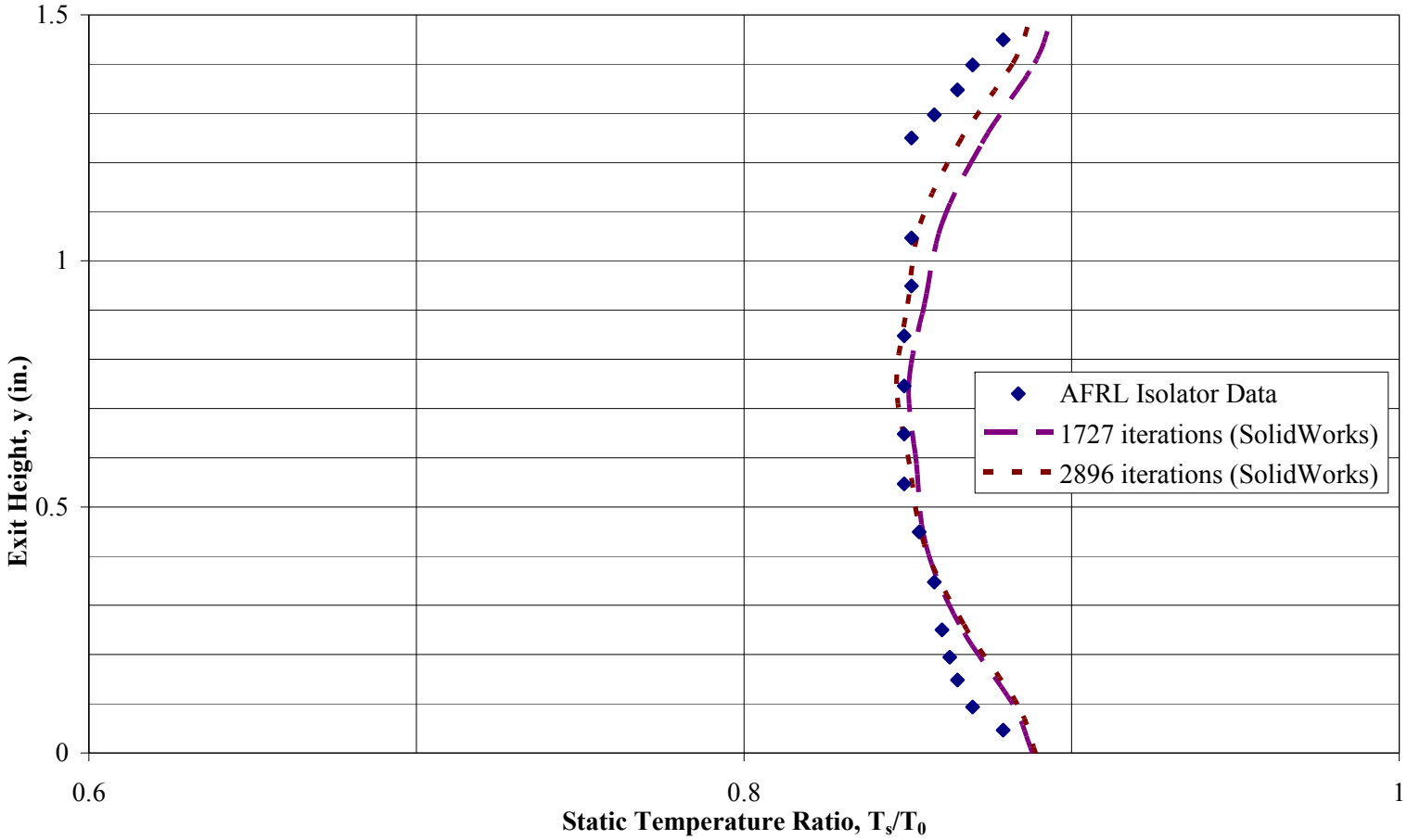

Fig. 30 Comparison of CFD solution and wind tunnel data for isolator exit static temperature distribution, PR=2.38

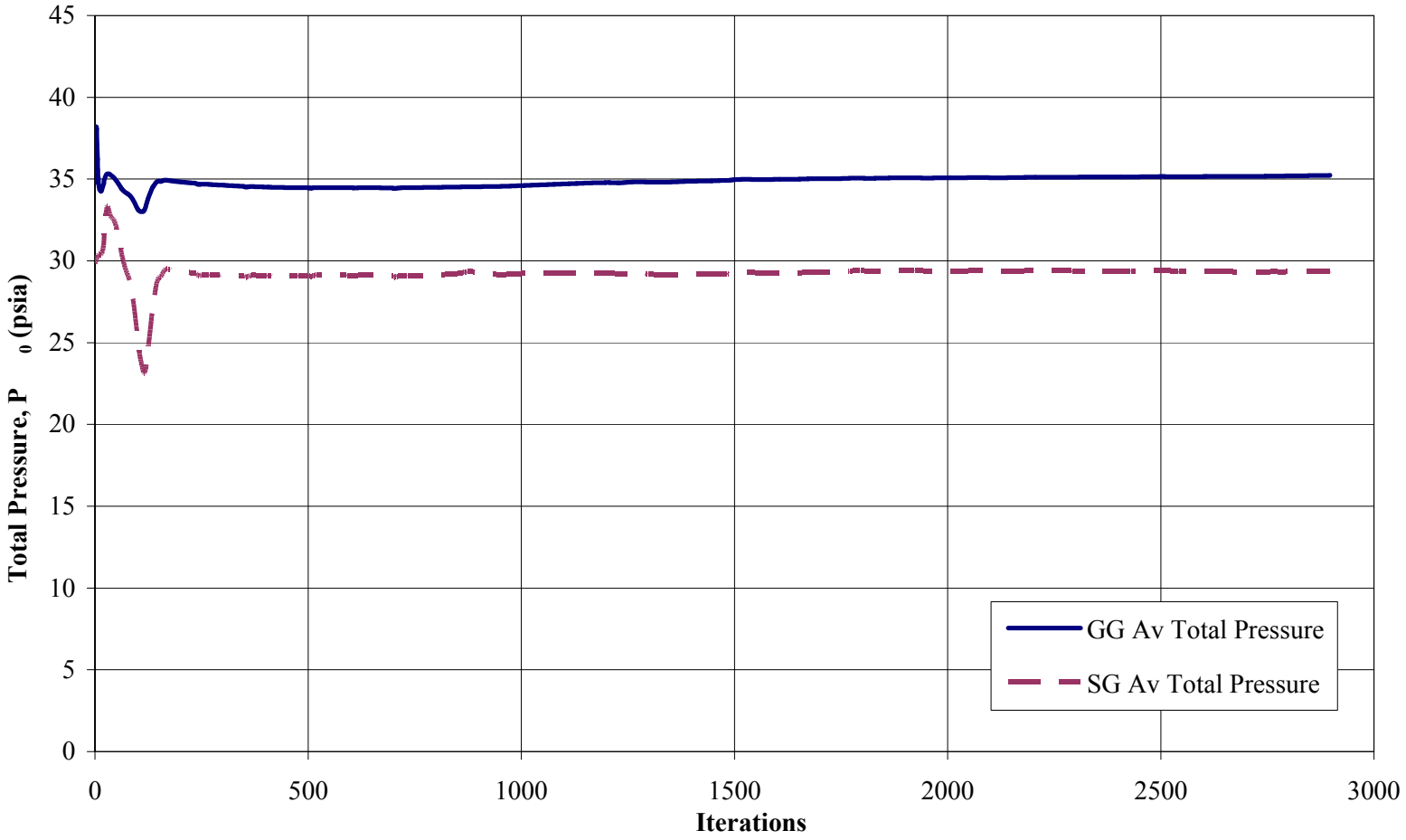

Fig. 31 Total pressure convergence history for the nozzle-isolator control volume and the isolator exit, PR=2.38

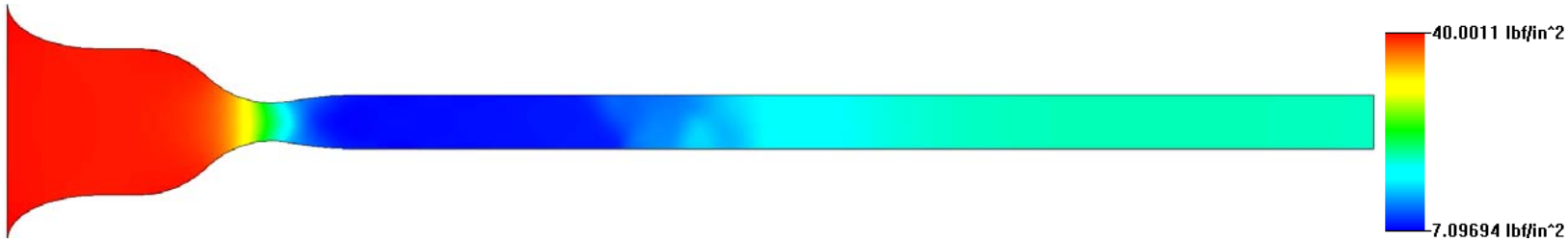

Fig. 32 CFD progression of static pressure for a PR=2.38 case

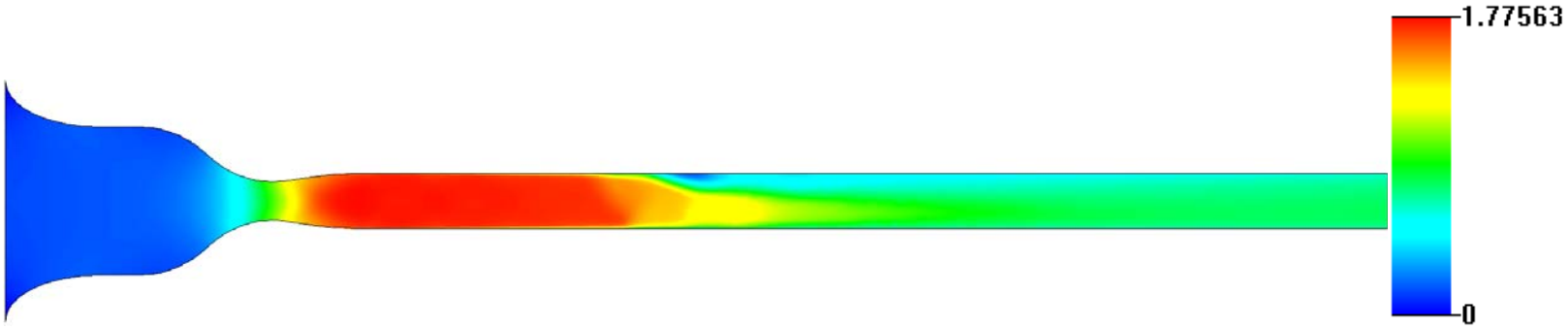

Fig. 33 CFD progression of Mach number for a PR=2.38 case

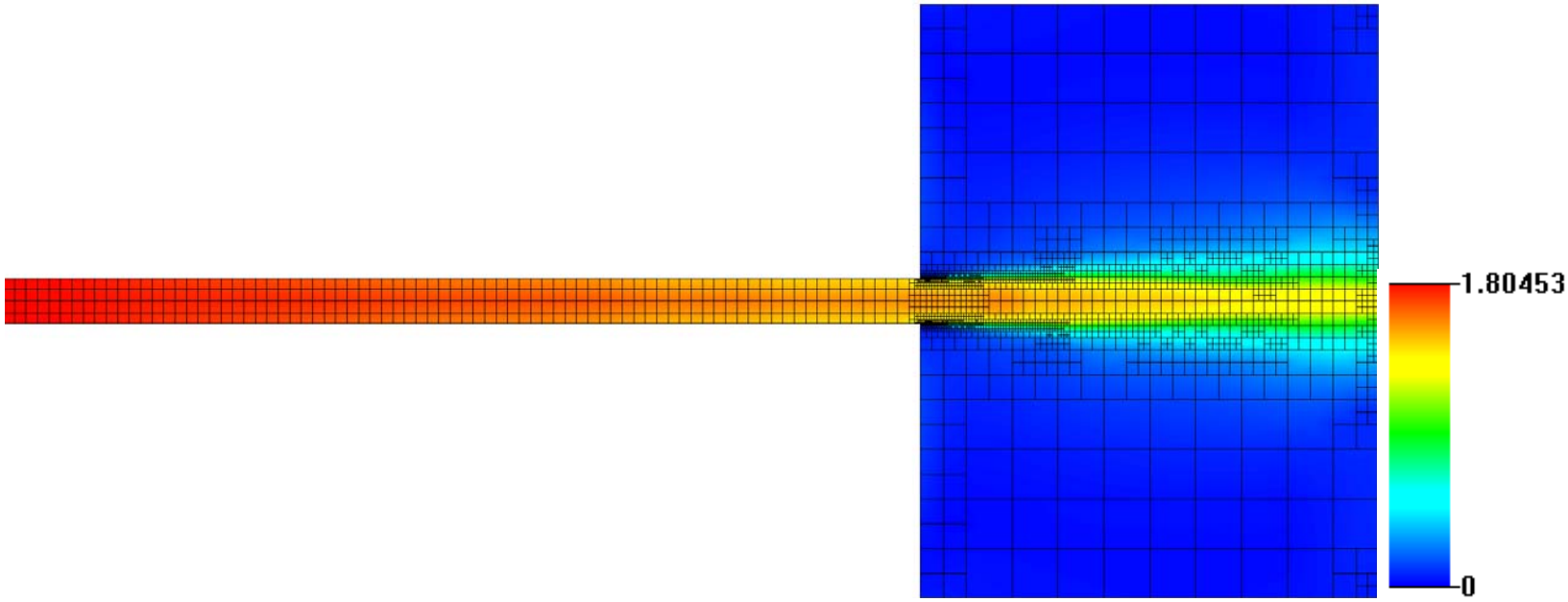

Fig. 34 Final grid mesh for 1X no back pressure case with Mach number contours

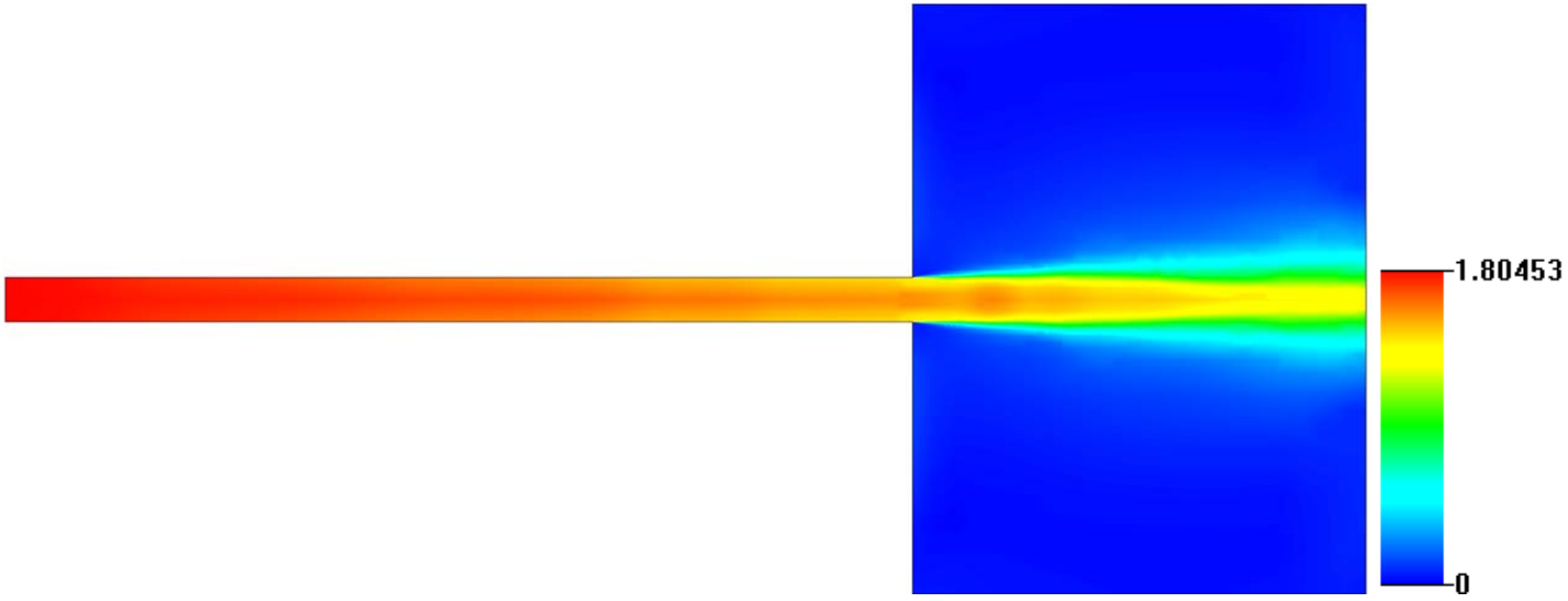

Fig. 35 Mach number contour for a 1X no back pressure case

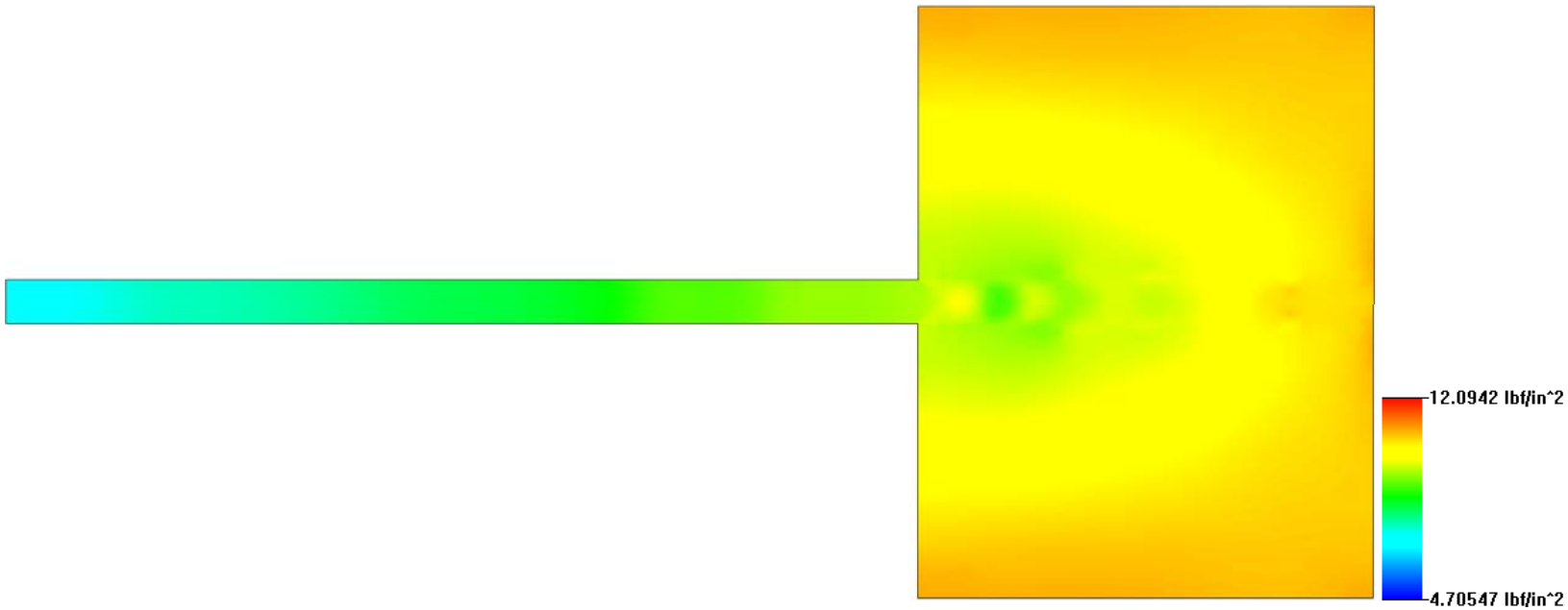

Fig. 36 Static pressure contour for 1X no back pressure case

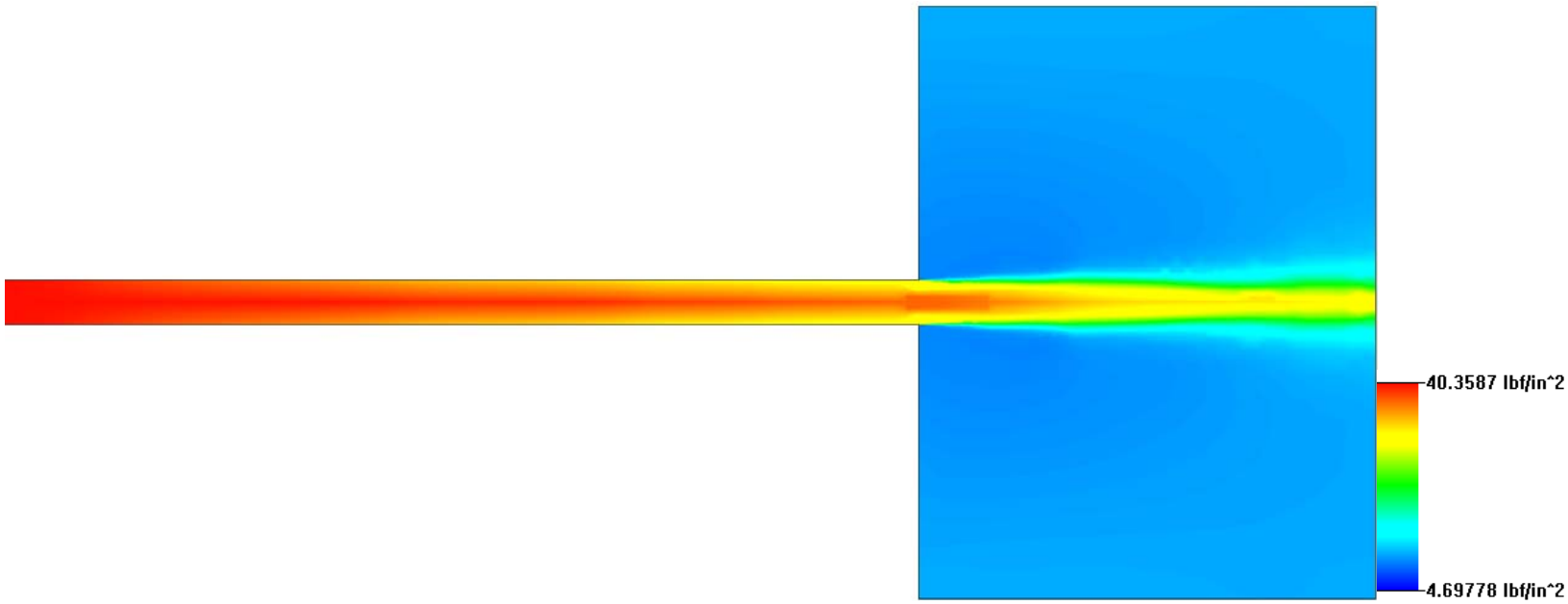

Fig. 37 Total pressure contour for a 1X no back pressure case

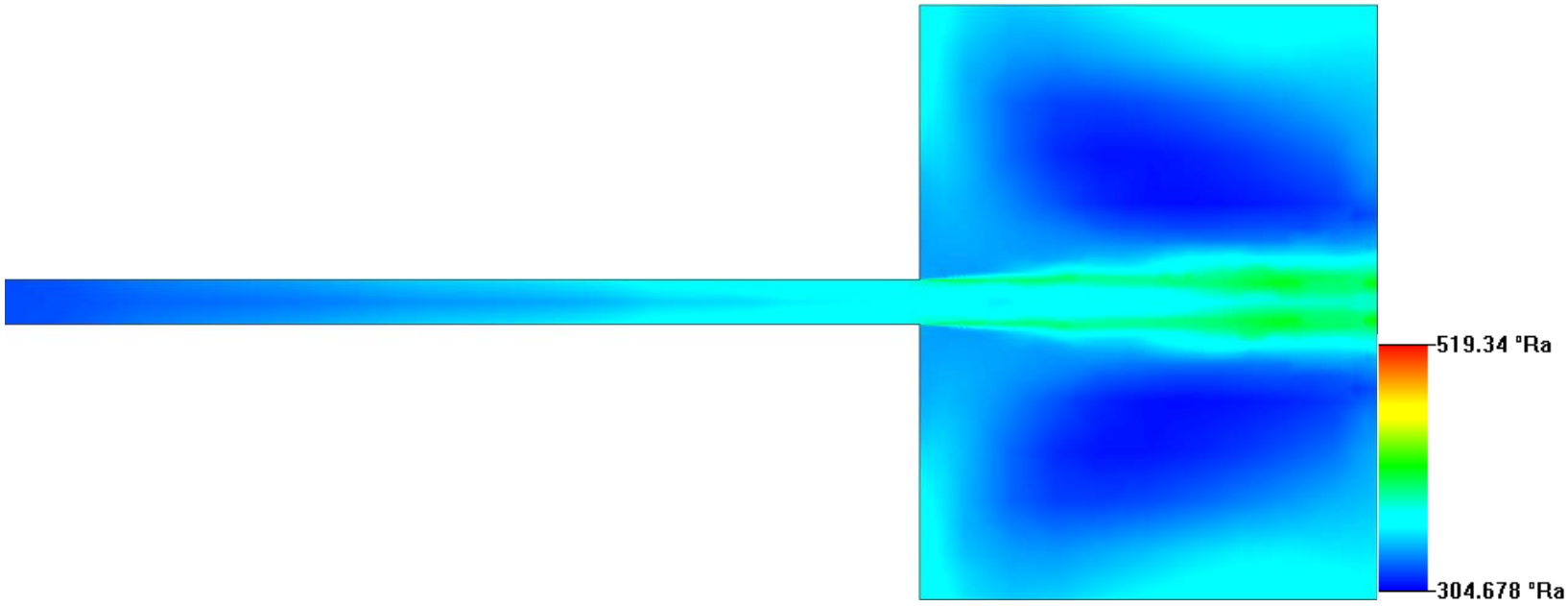

Fig. 38 Static temperature contour for a 1X no back pressure case

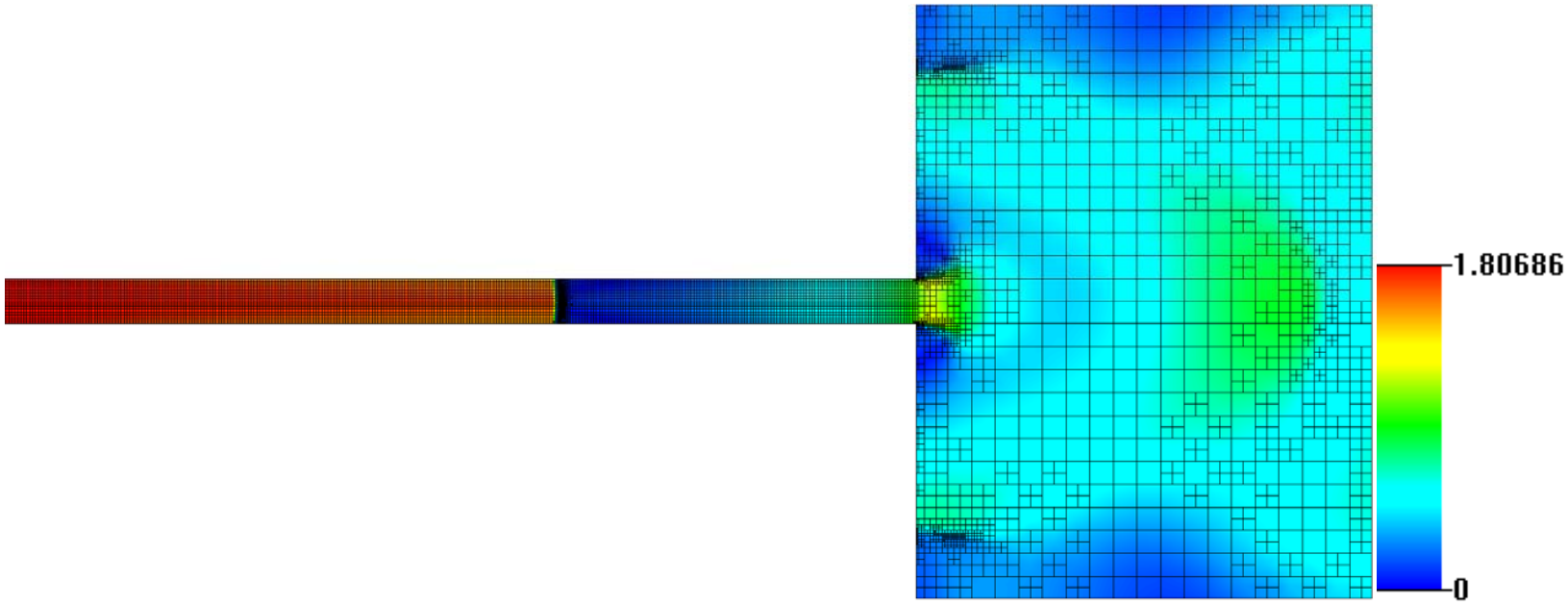

Fig. 39 Final grid mesh for a 1X PR=2.38 case with Mach number contour

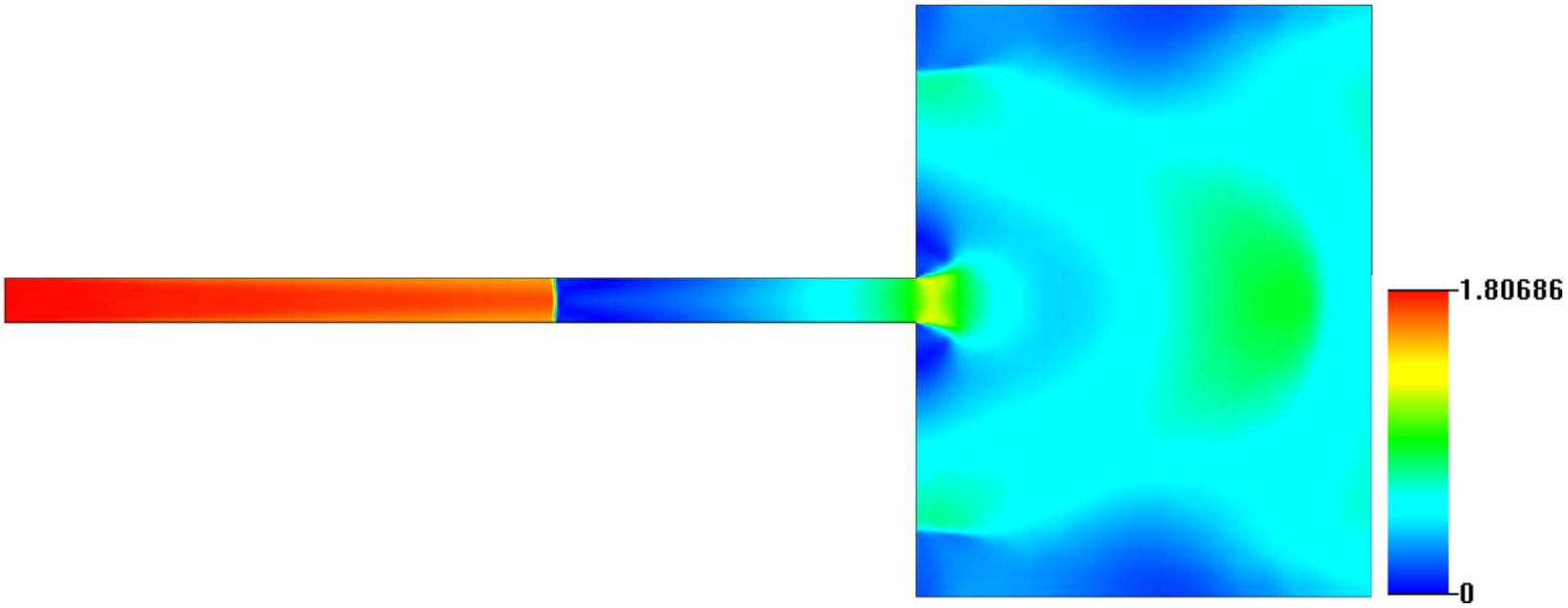

Fig. 40 Mach number contour for a 1X PR=2.38 case

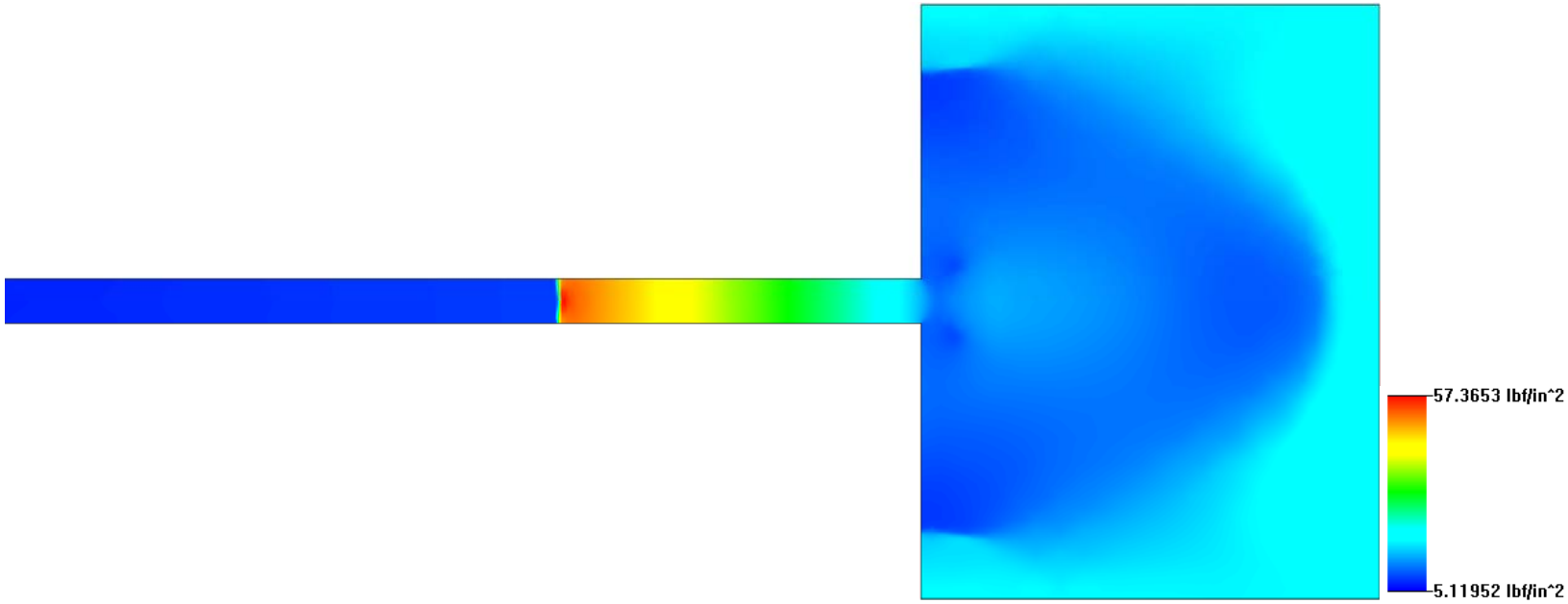

Fig. 41 Static pressure contour for a 1X PR=2.38 case

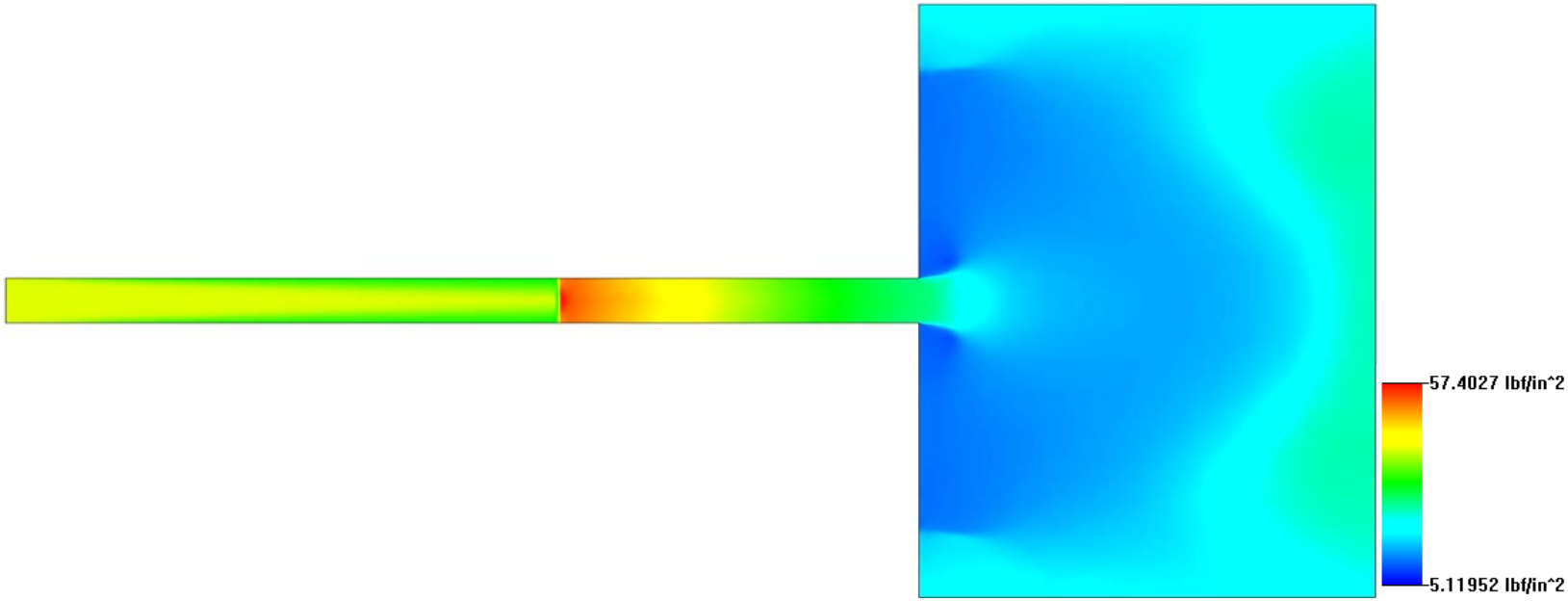

Fig. 42 Total pressure contour for a 1X PR=2.38 case

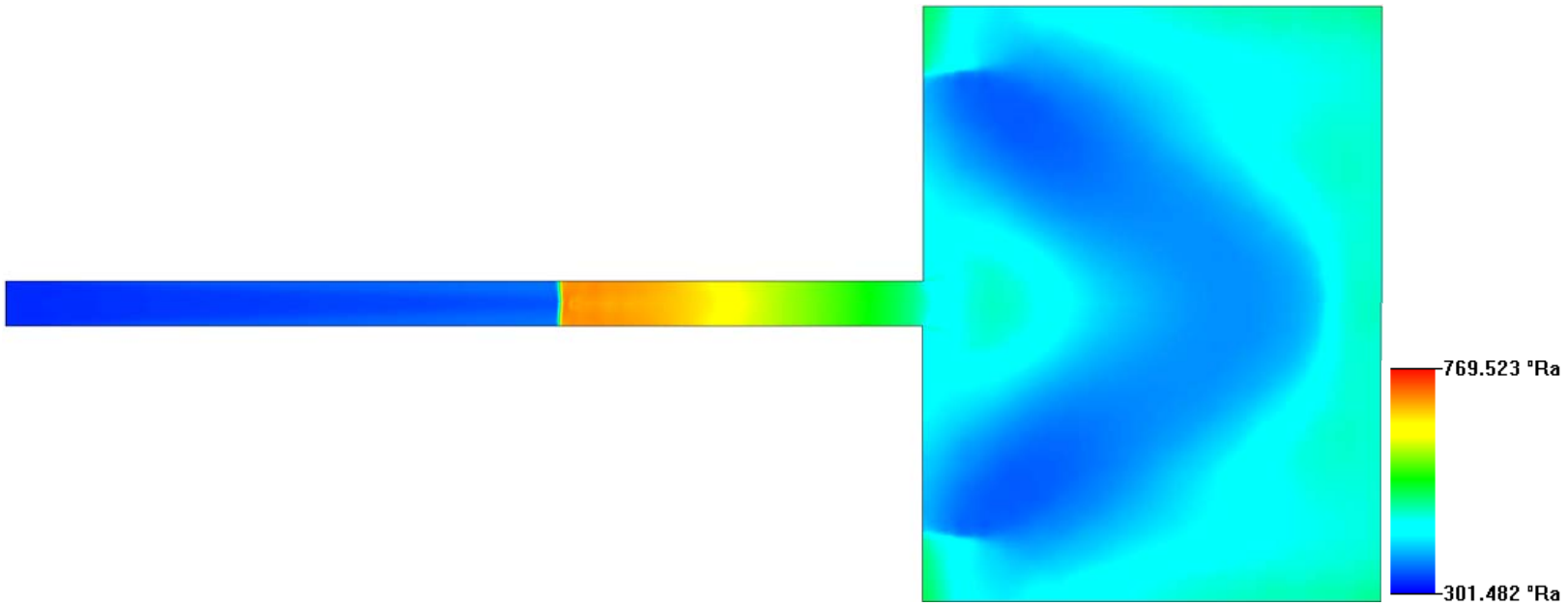

Fig. 43 Static temperature contour for a 1X PR=2.38 case

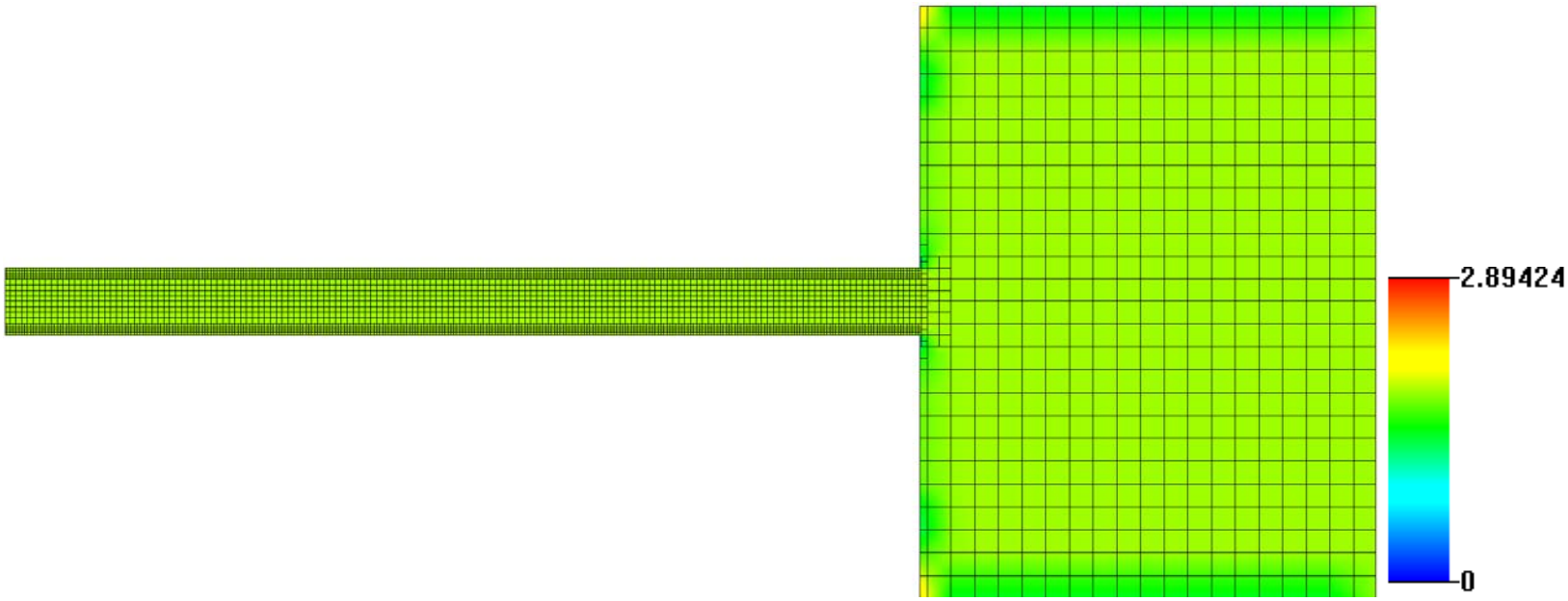

Fig. 44 Initial mesh for a 10X PR=2.38 case with Mach number contour

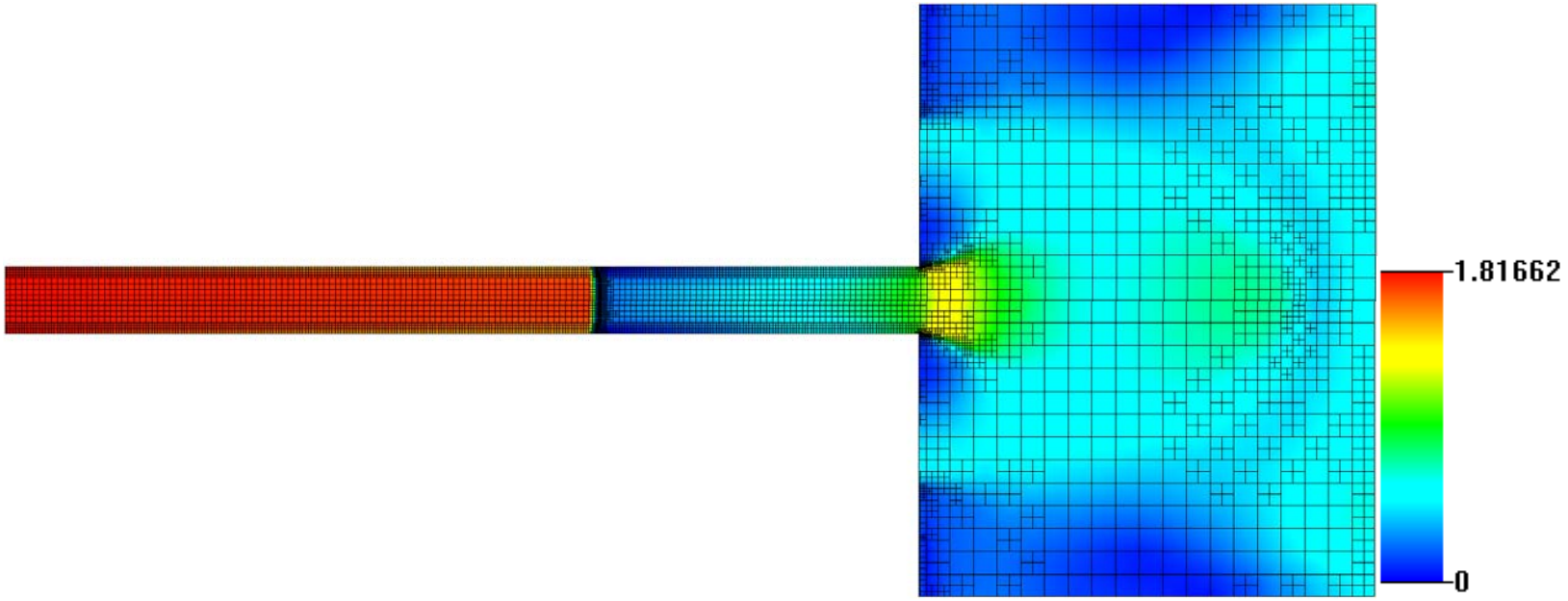

Fig. 45 Final grid mesh with Mach number contour for a 10X PR=2.38 case

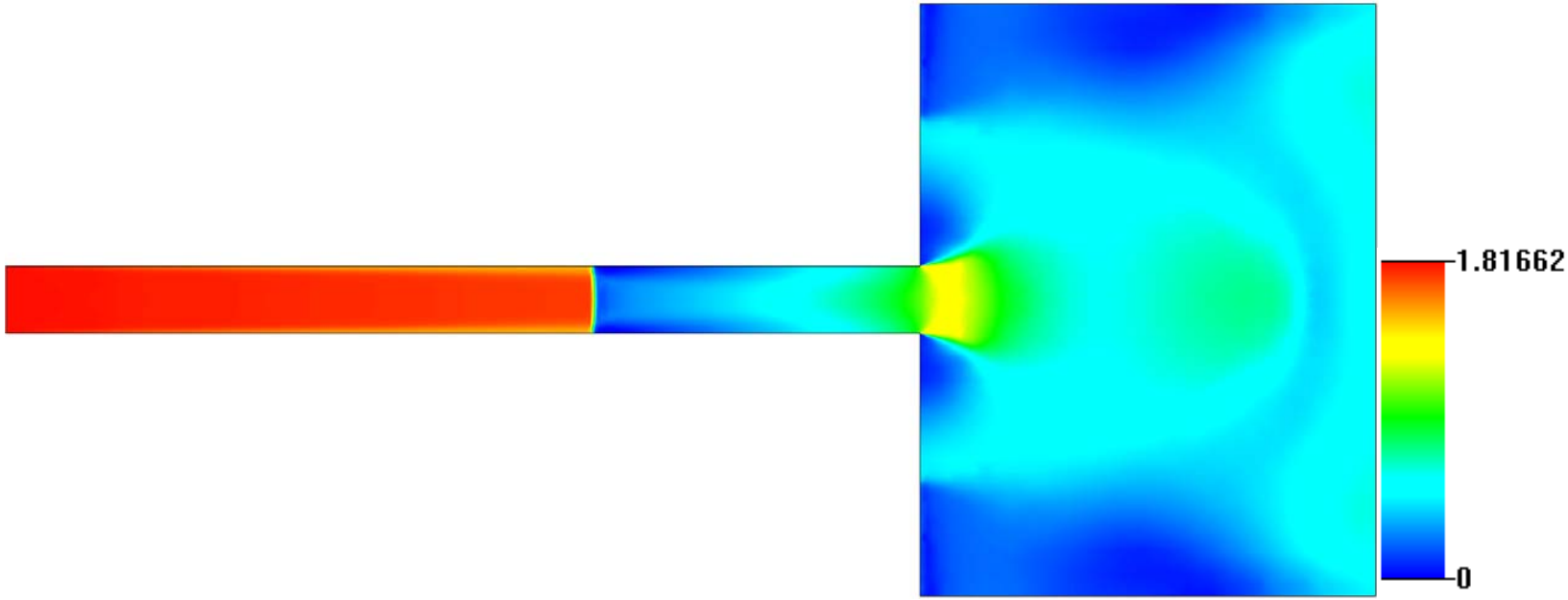

Fig. 46 Mach number contour for a 10X PR=2.38 case

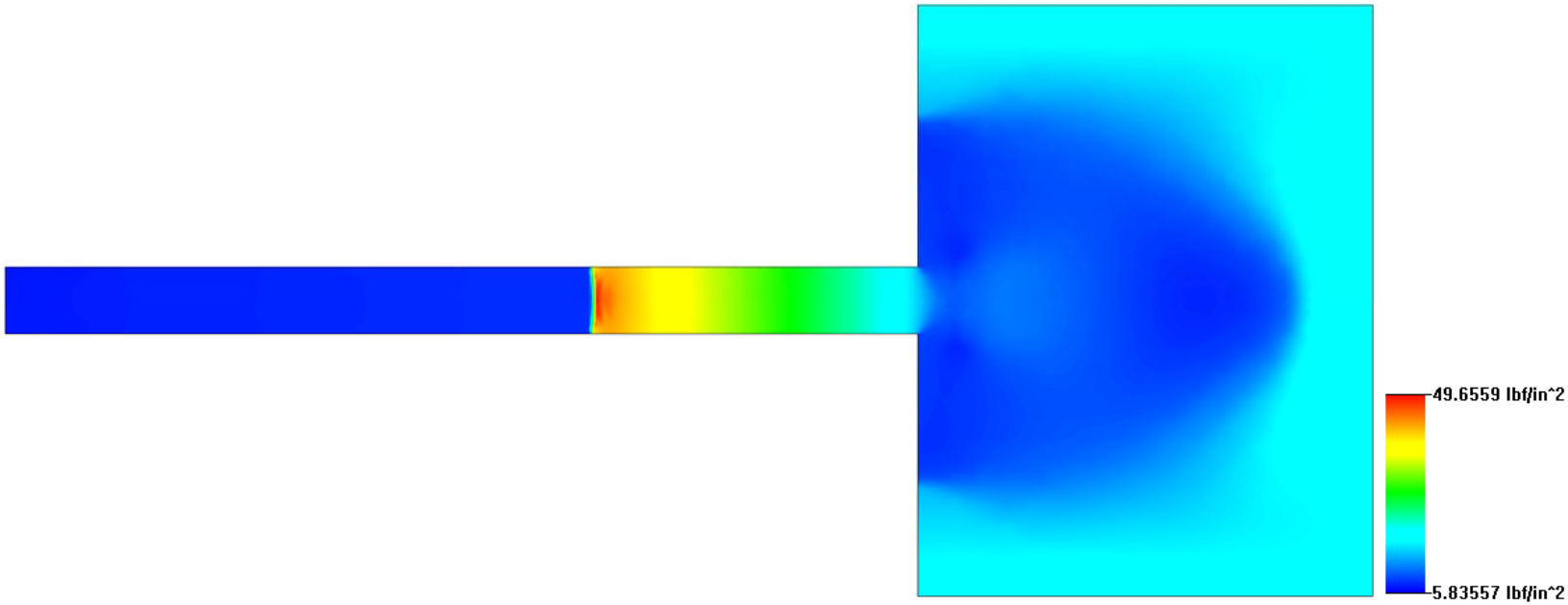

Fig. 47 Static pressure contour for a 10X PR=2.38 case

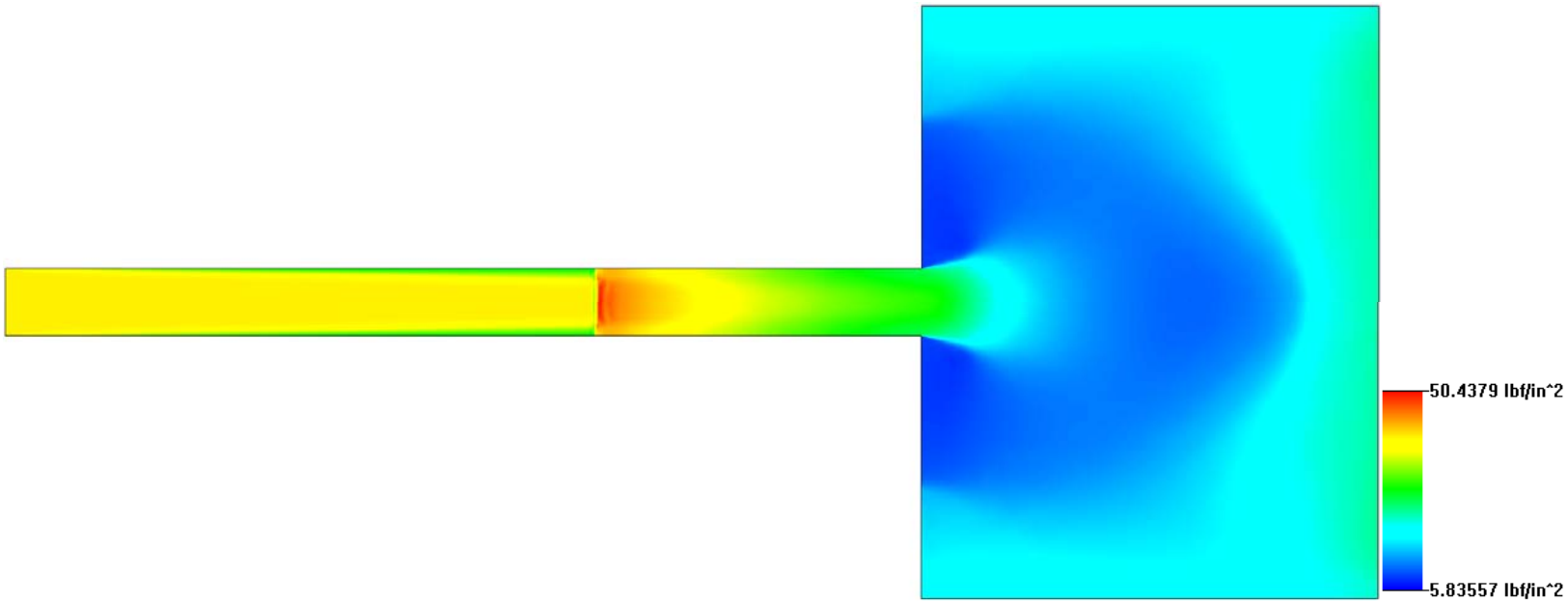

Fig. 48 Total pressure contour for a 10X PR=2.38 case

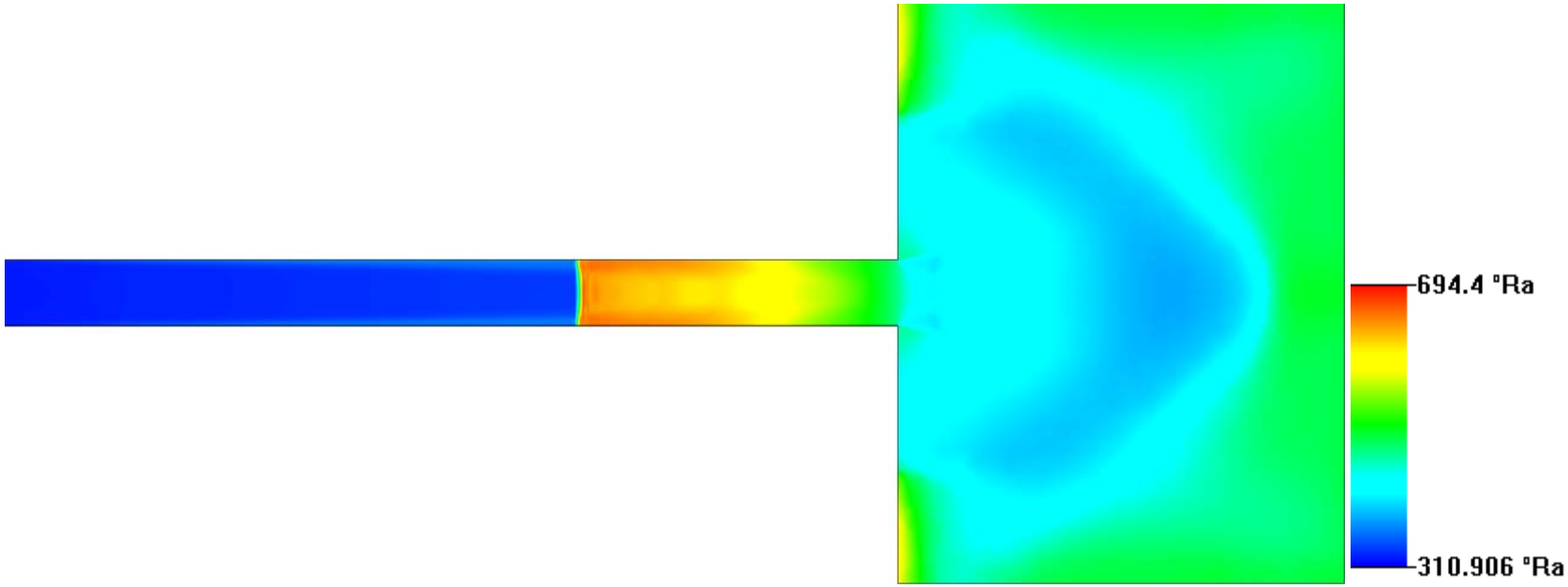

Fig. 49 Static temperature contour for a 10X PR=2.38 case

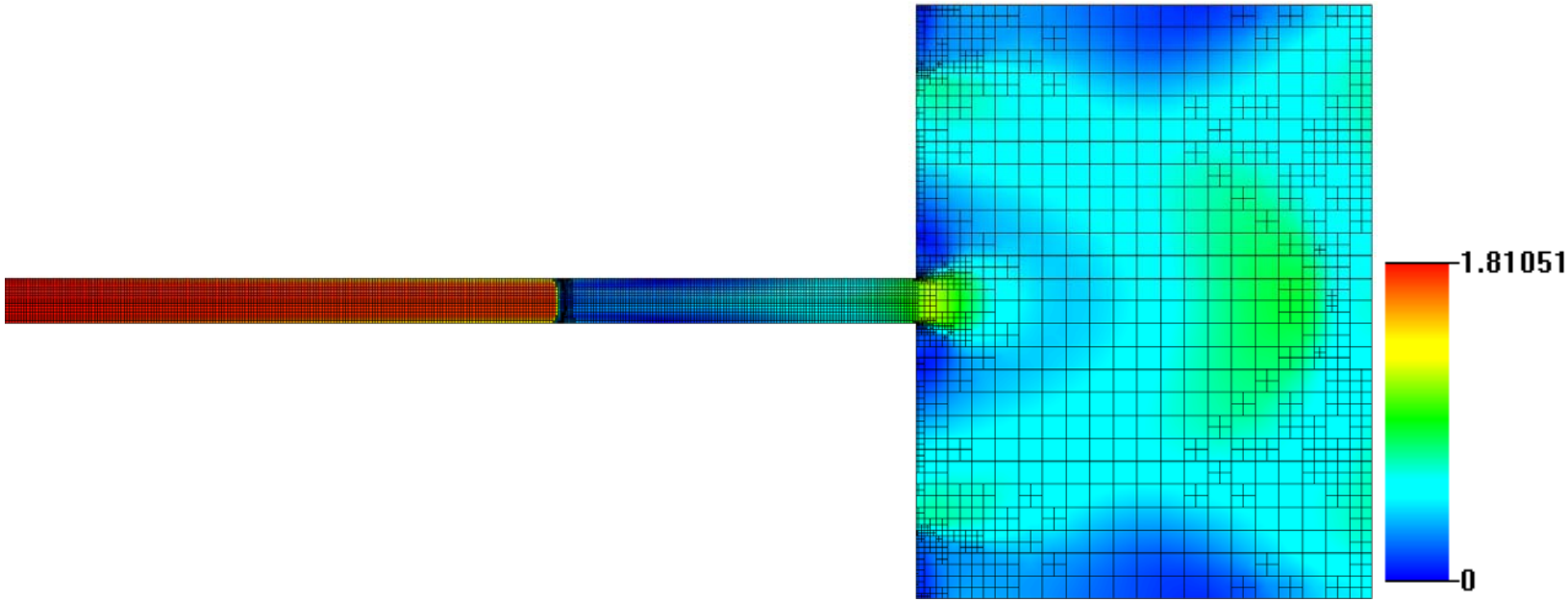

Fig. 50 Final grid mesh for 100X PR=2.38 case with Mach number contour

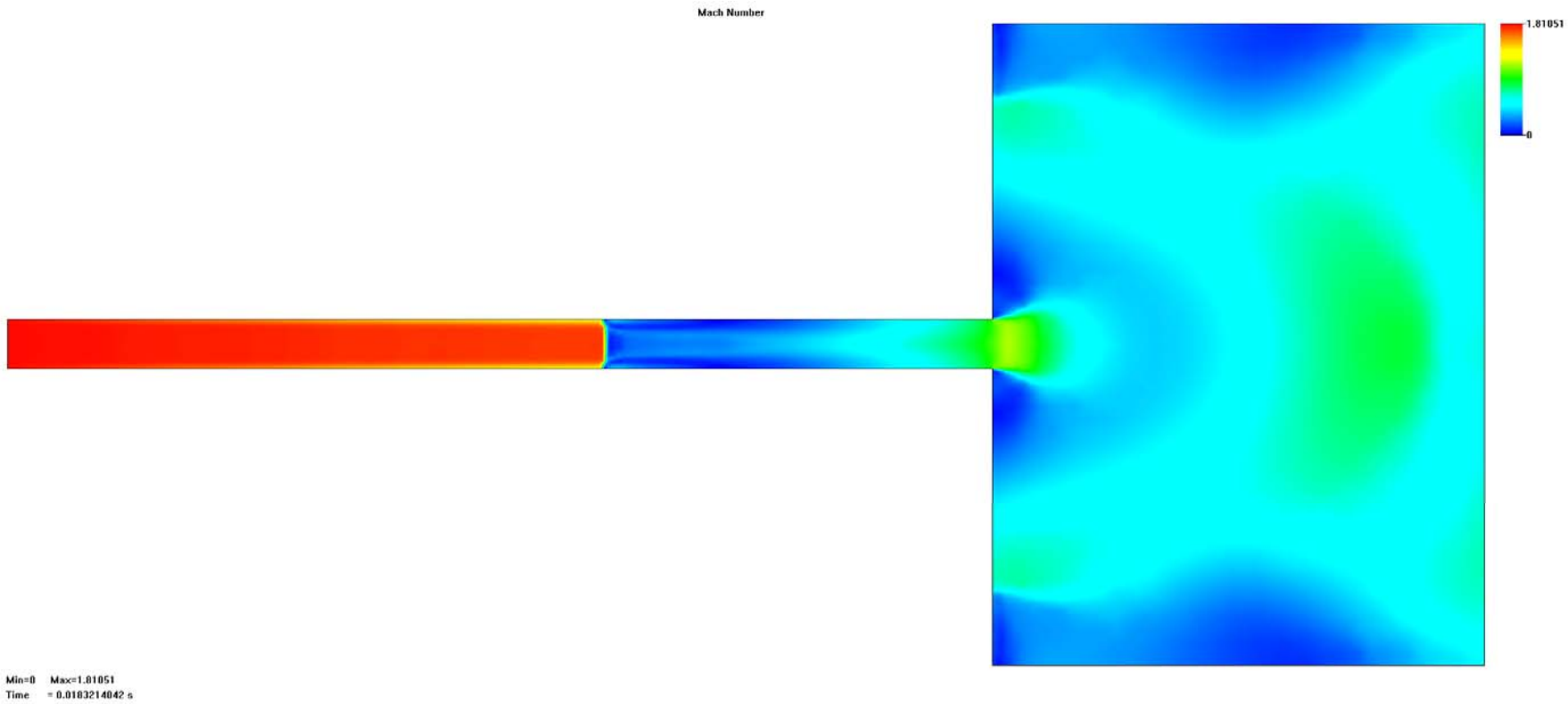

Fig. 51 Mach number contour for a 100X PR=2.38 case

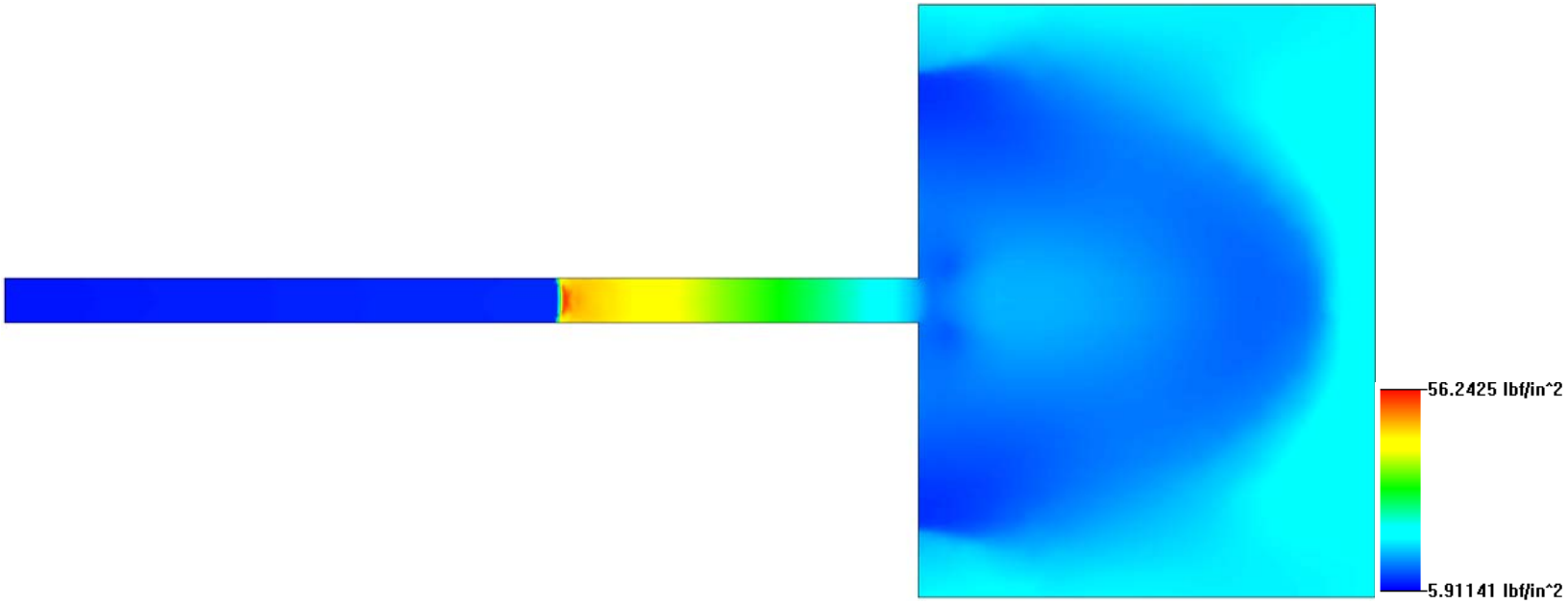

Fig. 52 Static pressure contour for a 100X PR=2.38 case

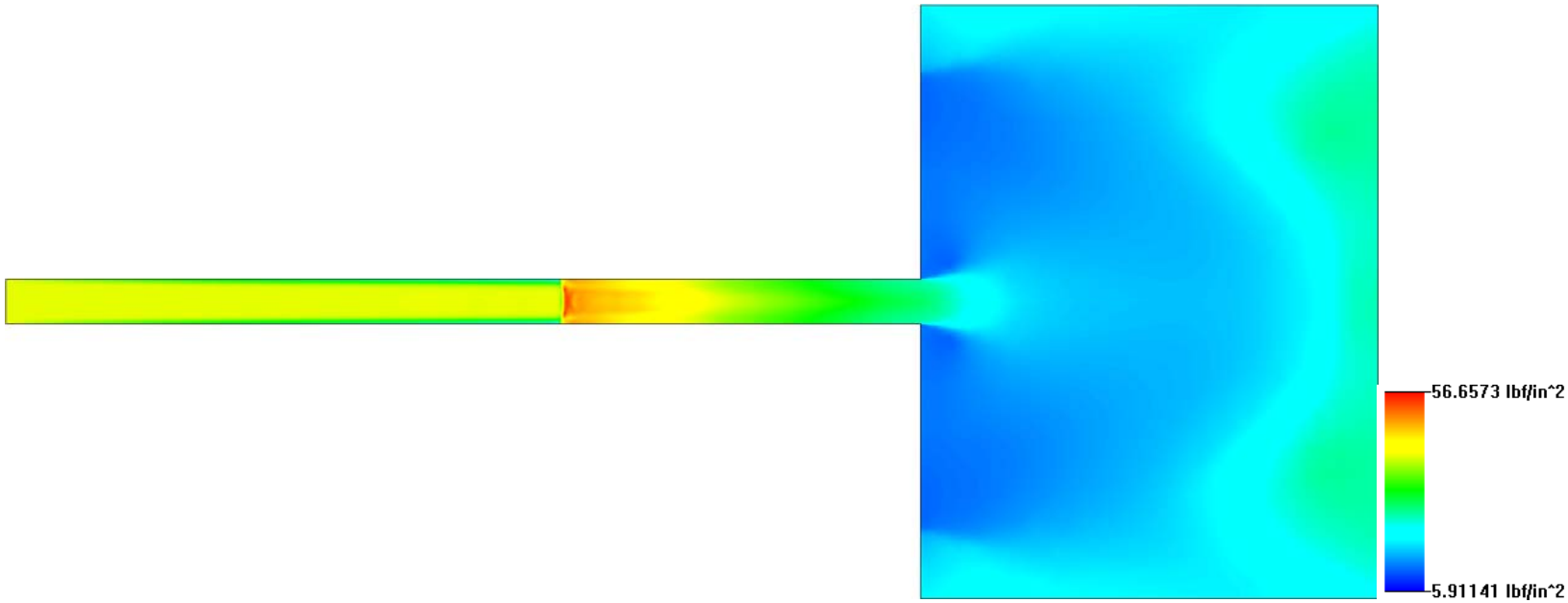

Fig. 53 Total pressure contour for a 100X PR=2.38 case

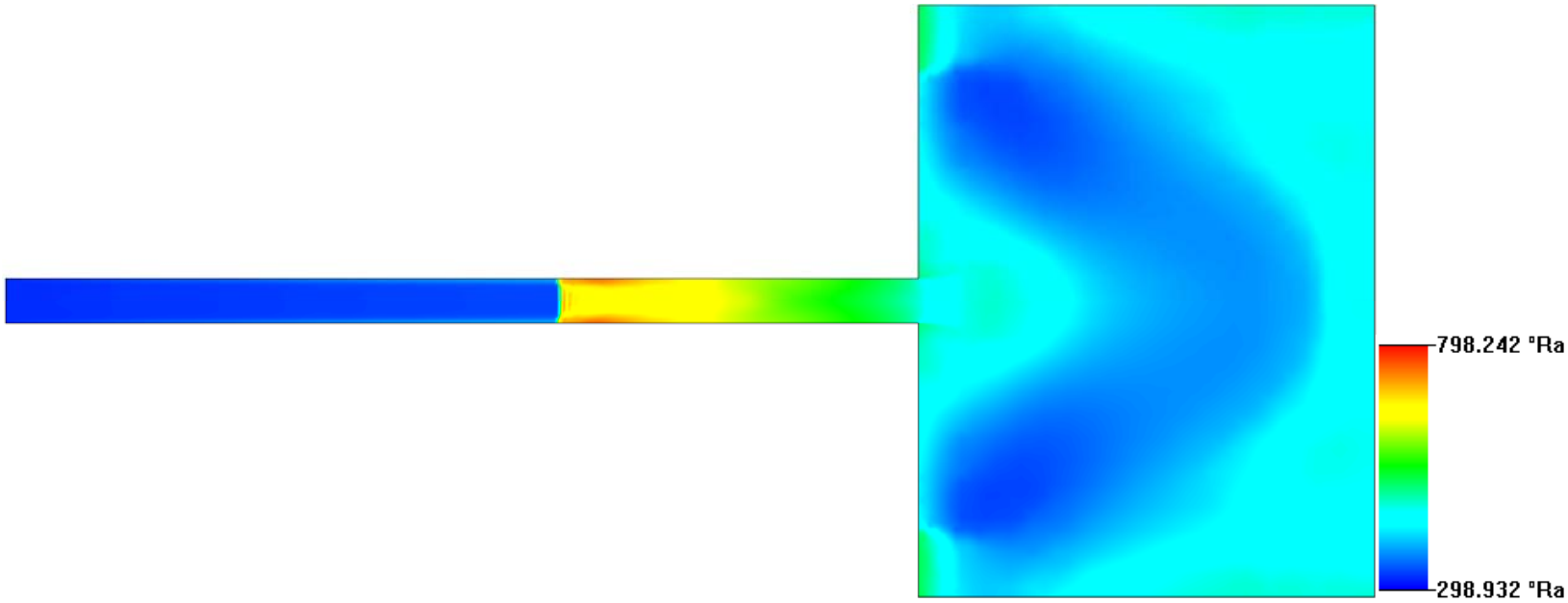

Fig. 54 Static temperature contour for a 100X PR=2.38 case

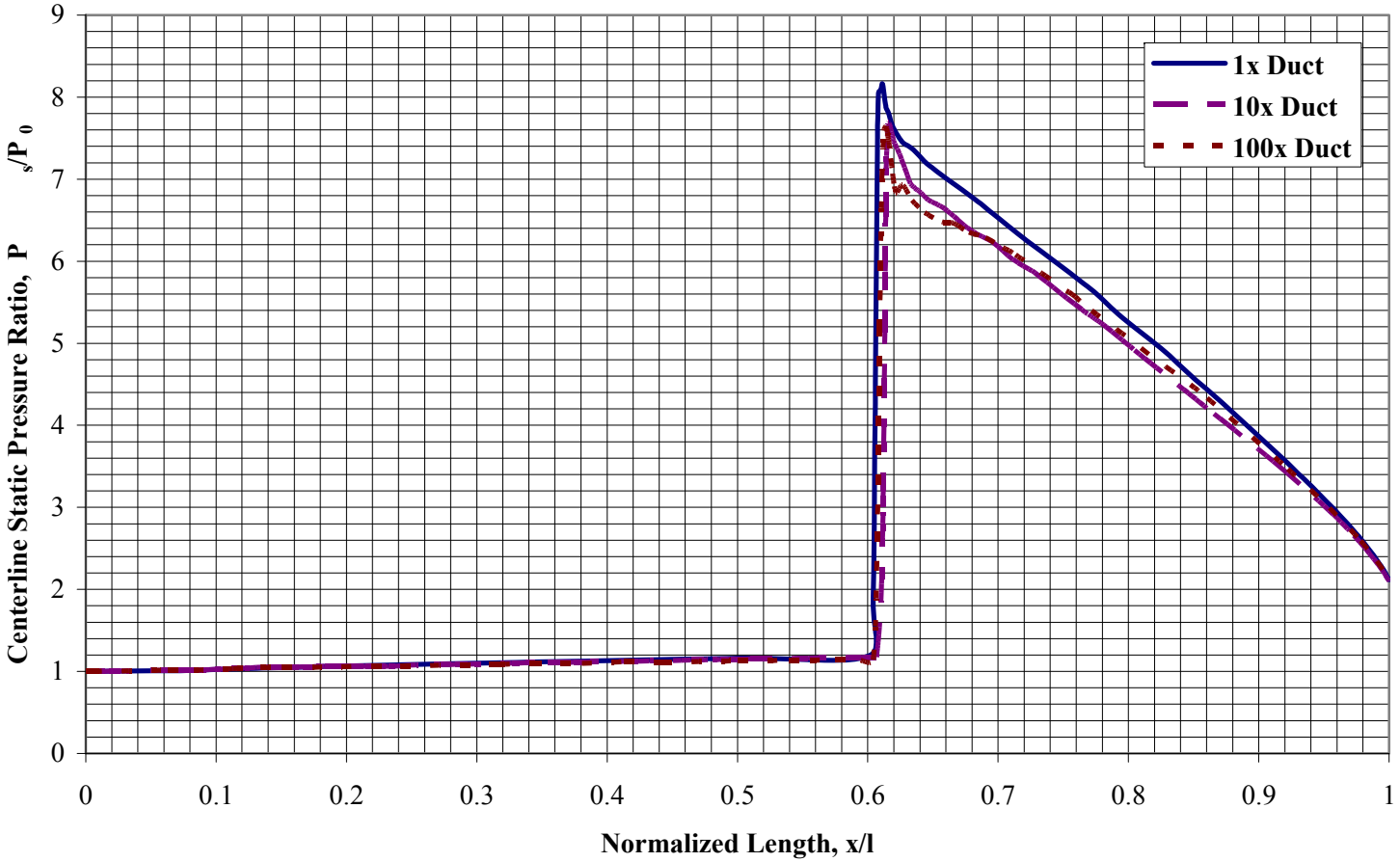

Fig. 55 Comparison of centerline static pressure distribution for scaled isolators, PR=2.38 case

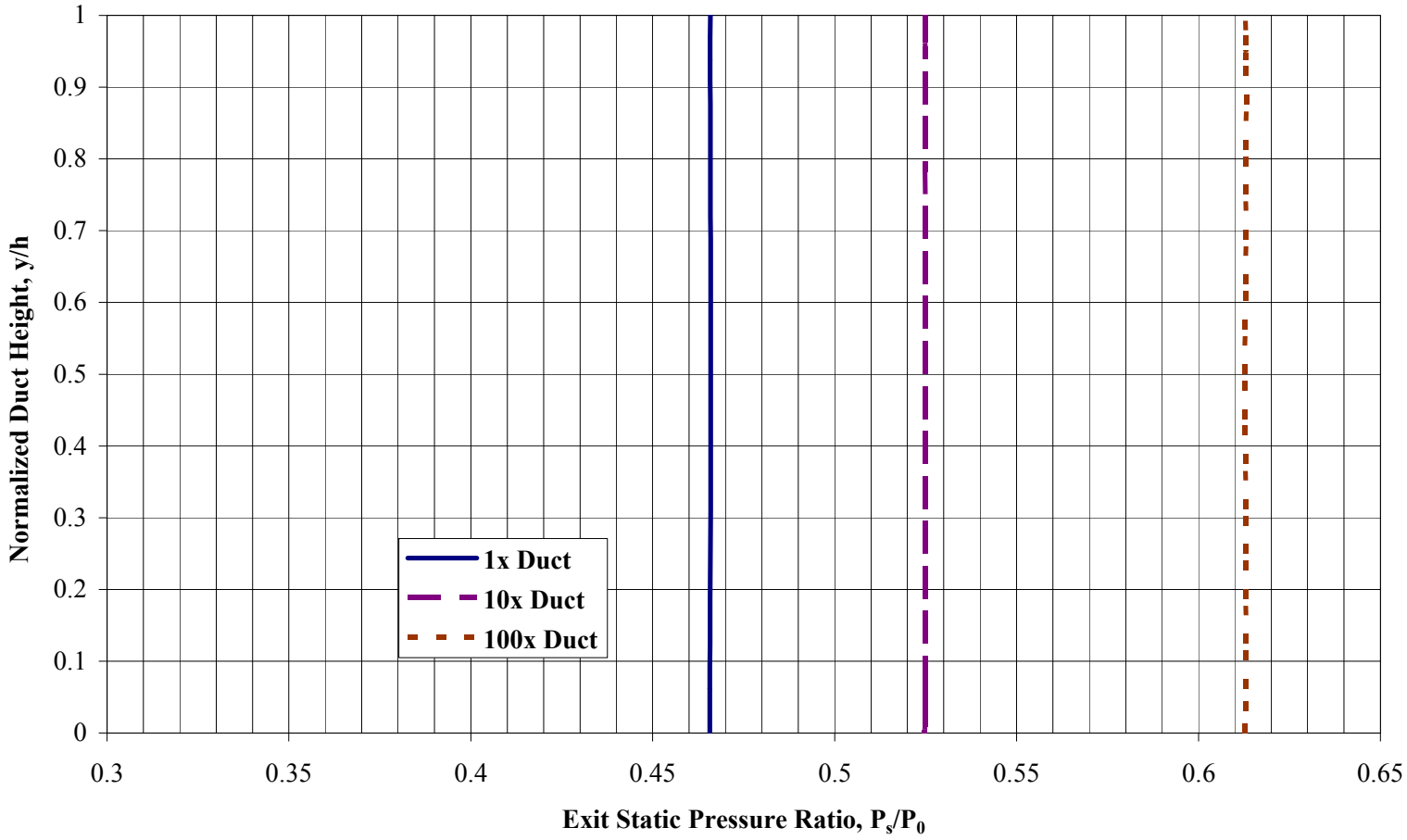

Fig. 56 Comparison of exit static pressure profiles for scaled isolators, PR=2.38

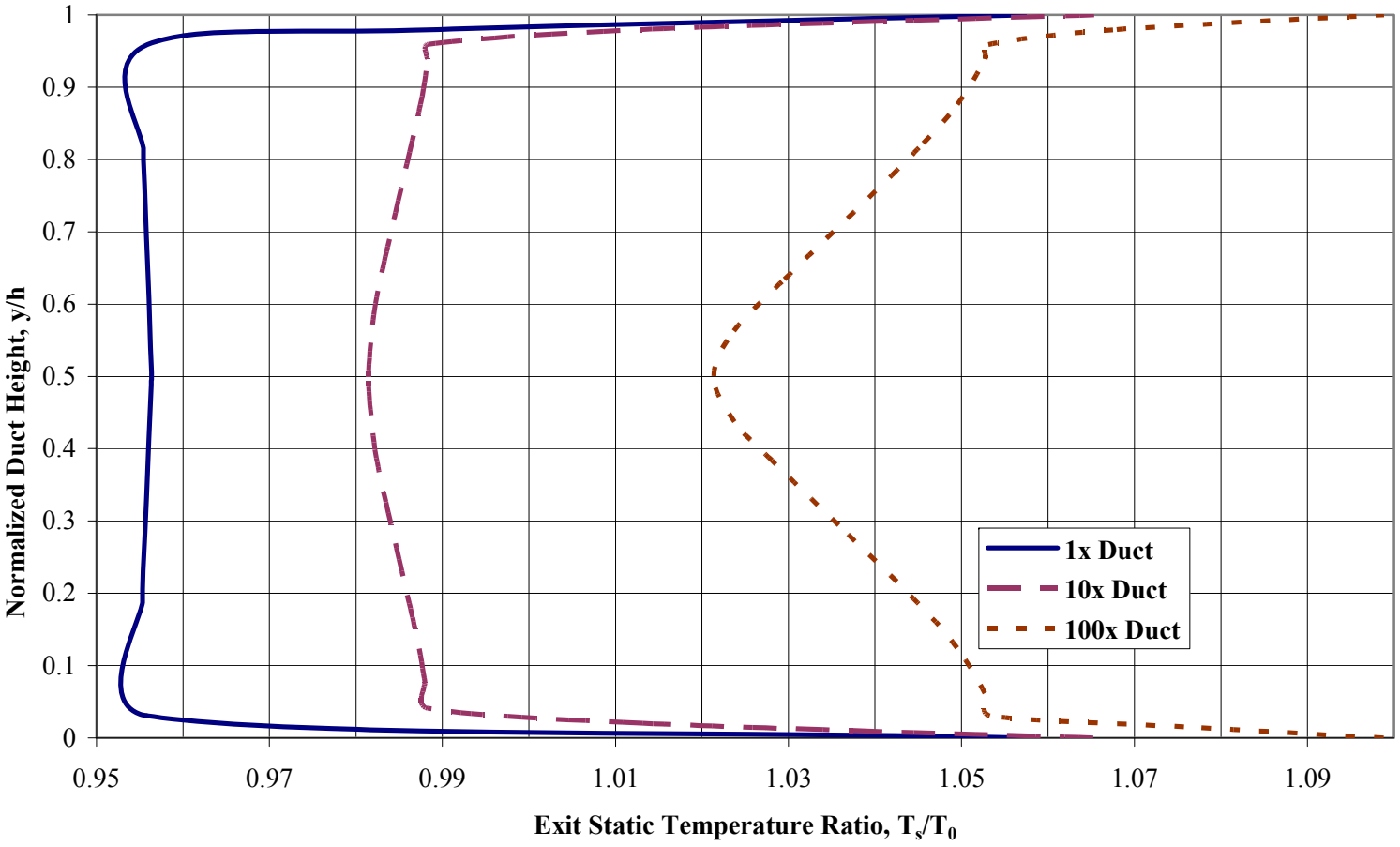

Fig. 57 Comparison of exit static temperature profiles for scaled isolators, PR=2.38

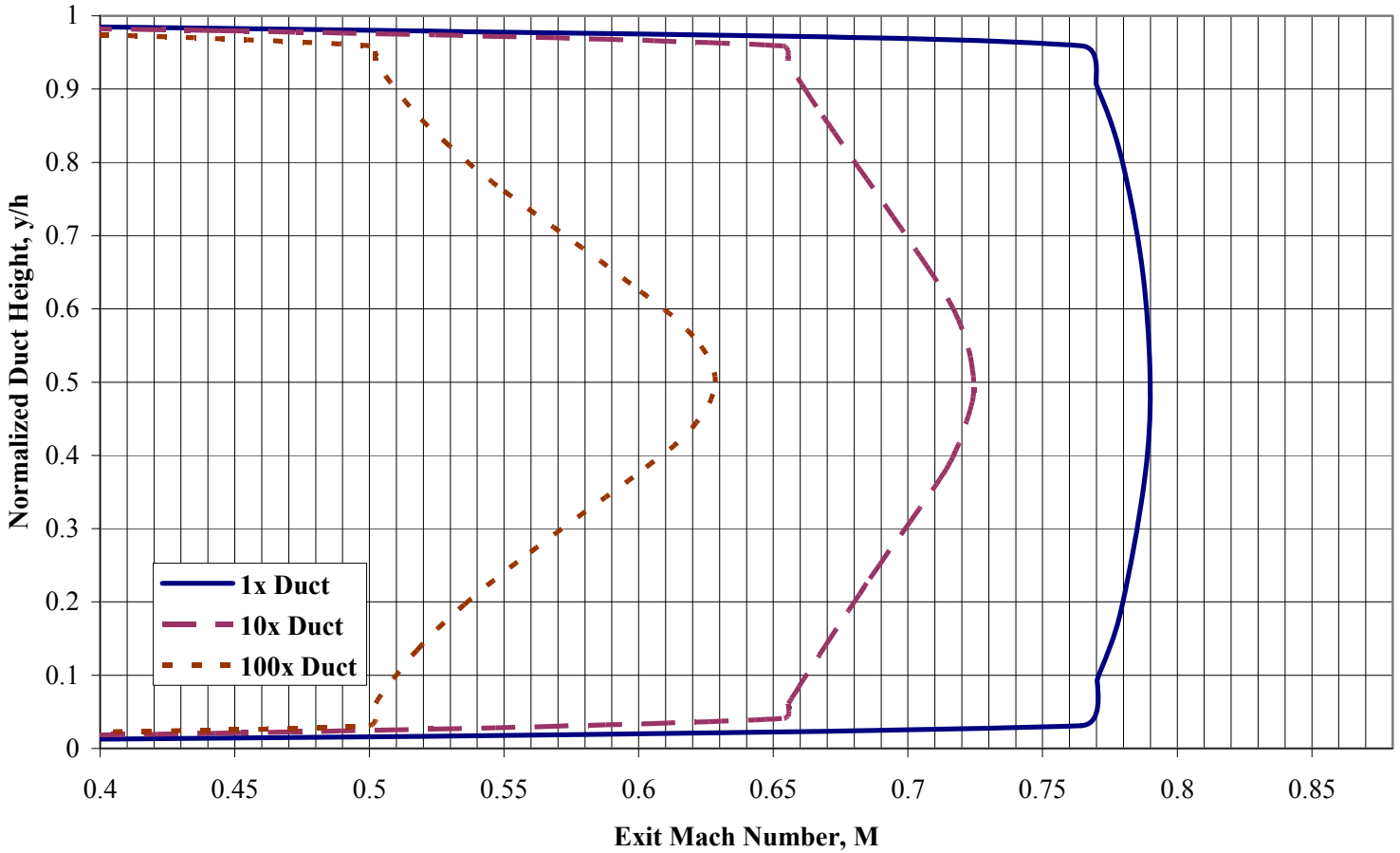

Fig. 58 Comparison of exit Mach number profiles for scaled isolators, PR=2.38

B. Sample Calculations for Converging-Diverging Duct CFD Validation Case

Initial Conditions and Set-up

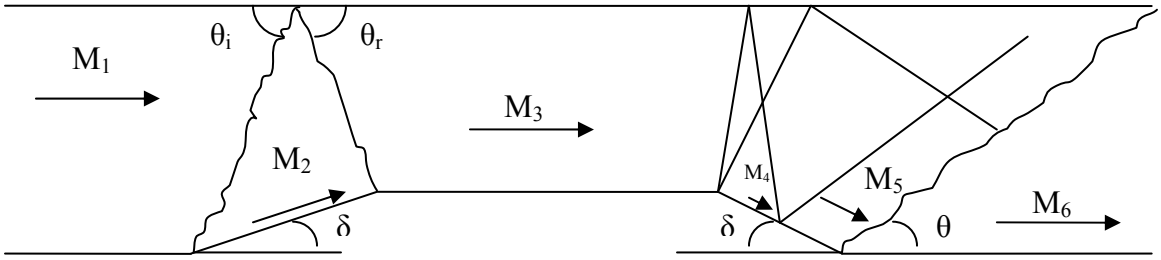

Fig. B. 1 Predicted flow interactions inside CD nozzle

$$M_1 = \text{Mach at entrance= } 3 \tag{24}$$

$$T_1 = \text{Temperature at entrance=293 } K \tag{25}$$

$$P_1 = \text{Pressure at entrance=1 atm} \tag{26}$$

$$\delta = \text{Wall Deflection=11.36}^{\circ} \tag{27}$$

$$\lambda = \sqrt{\left(M_1^2 - 1\right)^2 - 3\left(1 + \frac{\gamma - 1}{2} M_1^2\right)\left(1 + \frac{\gamma + 1}{2} M_1^2\right)\tan^2 \delta} = 7.75 \tag{28}$$

$$\chi = \frac{\left(M_1^2 - 1\right)^3 - 9\left(1 + \frac{\gamma - 1}{2} M_1^2\right)\left(1 + \frac{\gamma - 1}{2} M_1^2 + \frac{\gamma + 1}{4} M_1^4\right)\tan^2 \delta}{\lambda^3} = .989 \tag{29}$$

$$\theta_i = \tan^{-1}\left\{\frac{M_1{}^2 - 1 + 2\lambda\cos\left[\left(4\pi x + \cos^{-1}\chi\right)\Big/3\right]}{3\left(1+\frac{\gamma-1}{2}M_1{}^2\right)\tan\delta}\right\} = 28.6^\circ \tag{30}$$

Where $\left\{\begin{matrix} x = 1 \text{ for weak shocks} \\ x = 0 \text{ for strong shocks}\end{matrix}\right\}$

$$M_{1_n} = \text{Mach at entrance normal to shock wave} = M_1 \sin\theta_i = 1.438 \tag{31}$$

$$M_{2_n} = \text{Mach behind normal shock} = \sqrt{\frac{\left[M_{1_n}^2(\gamma-1)\right]+2}{2\gamma M_{1_n}^2 - (\gamma-1)}} = .724 \tag{32}$$

$$\frac{T_2}{T_1} = \left[1+\frac{2\gamma\left(M_{1_n}^2-1\right)}{\gamma+1}\right]\left[\frac{2+(\gamma-1)M_{1_n}^2}{(\gamma+1)M_{1_n}^2}\right] = 1.279 \tag{33}$$

$$T_2 = \frac{T_2}{T_1}T_1 = 375 \text{ K} \tag{34}$$

$$\mathrm{M}_{2_t} = M_1\cos\theta_i\sqrt{\frac{T_1}{T_2}} = 2.33 \tag{35}$$

$$\mathrm{M}_2 = \sqrt{M_{2_n}^2 + M_{2_t}^2} = 2.44 \tag{36}$$

$$P_{o1} = \frac{P_{o1}}{P_1}P_1 = P_1\left(1+\frac{\gamma-1}{2}M_1^2\right)^{\frac{\gamma}{\gamma-1}} = 36.7 \text{ atm} \tag{37}$$

$$\frac{P_2}{P_1} = 1+\frac{2\gamma\left(M_1^2-1\right)}{\gamma+1} = 2.25 \tag{38}$$

$$P_2 = \frac{P_2}{P_1} P_1 = 2.25 \text{ atm} \tag{39}$$

$$\frac{P_{o2}}{P_{o1}} = \left[\frac{(\gamma+1) M_{1_n}^2}{2+(\gamma-1) M_{1_n}^2} \right]^{\frac{\gamma}{\gamma-1}} \left[\frac{\gamma+1}{2\gamma M_{1_n}^2 - (\gamma-1)} \right]^{\frac{1}{\gamma-1}} = .948 \tag{40}$$

$$P_{o2} = \frac{P_{o2}}{P_{o1}} P_{o1} = 34.9 \text{ atm} \tag{41}$$

$$\lambda = \sqrt{\left(M_2{}^2 - 1\right)^2 - 3\left(1 + \frac{\gamma-1}{2} M_2{}^2\right)\left(1 + \frac{\gamma+1}{2} M_2{}^2\right) \tan^2 \delta} = 4.72 \tag{42}$$

$$\chi = \frac{\left(M_2{}^2 - 1\right)^3 - 9\left(1 + \frac{\gamma-1}{2} M_2{}^2\right)\left(1 + \frac{\gamma-1}{2} M_2{}^2 + \frac{\gamma+1}{4} M_2{}^4\right) \tan^2 \delta}{\lambda^3} = .972 \tag{43}$$

$$\theta = \tan^{-1} \left\{ \frac{M_2{}^2 - 1 + 2\lambda \cos\left[\left(4\pi x + \cos^{-1} \chi \right) / 3 \right]}{3\left(1 + \frac{\gamma-1}{2} M_2{}^2\right) \tan \delta} \right\} = 33.9^\circ \tag{44}$$

Where $\left\{ \begin{array}{l} x = 1 \text{ for weak shocks} \\ x = 0 \text{ for strong shocks} \end{array} \right\}$

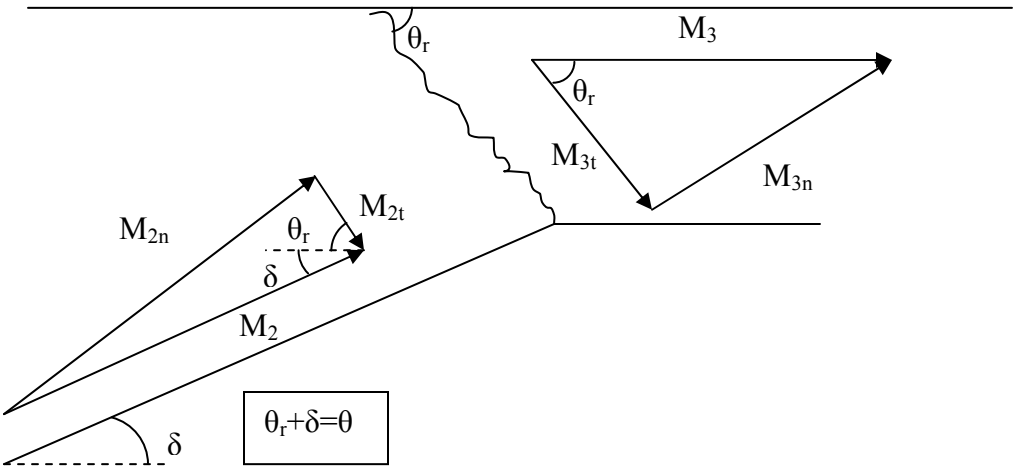

Fig. B. 2 Schematic of reflecting shock flow predictions

$$\theta_r = \theta - \delta = 22.5^\circ \tag{45}$$

$$M_{2_n} = M_2 \sin\left(\theta_r + \delta\right) = 1.359 \tag{46}$$

$$M_{3_n} = \sqrt{\frac{\left[M_{2_n}^2\left(\gamma-1\right)\right]+2}{2\gamma M_{2_n}^2-\left(\gamma-1\right)}} = .769 \tag{47}$$

$$\frac{T_3}{T_2} = \left[1+\frac{2\gamma\left(M_{2_n}^2-1\right)}{\gamma+1}\right]\left[\frac{2+\left(\gamma-1\right)M_{2_n}^2}{\left(\gamma+1\right)M_{2_n}^2}\right] = 1.229 \tag{48}$$

$$T_3 = T_2\frac{T_3}{T_2} = 461 \text{ K} \tag{49}$$

$$\mathrm{M}_{3_t} = M_2 \cos\left(\theta_r + \delta\right)\sqrt{\frac{T_2}{T_3}} = 1.825 \tag{50}$$

$$\mathrm{M}_3 = \sqrt{M_{3_n}^2 + M_{3_t}^2} = 1.981 \tag{51}$$

$$\frac{P_3}{P_2} = 1 + \frac{2\gamma\left(M_{2_n}^2 - 1\right)}{\gamma + 1} = 1.990 \tag{52}$$

$$P_3 = P_2 \frac{P_3}{P_2} = 4.47 \text{ atm} \tag{53}$$

$$\frac{P_{o3}}{P_{o2}} = \left[\frac{\left(\gamma+1\right)M_{2_n}^2}{2+\left(\gamma-1\right)M_{2_n}^2}\right]^{\frac{\gamma}{\gamma-1}}\left[\frac{\gamma+1}{2\gamma M_{2_n}^2 - \left(\gamma-1\right)}\right]^{\frac{1}{\gamma-1}} = .968 \tag{54}$$

$$P_{o3} = P_{o2}\frac{P_{o3}}{P_{o2}} = 33.7 \text{ atm} \tag{55}$$

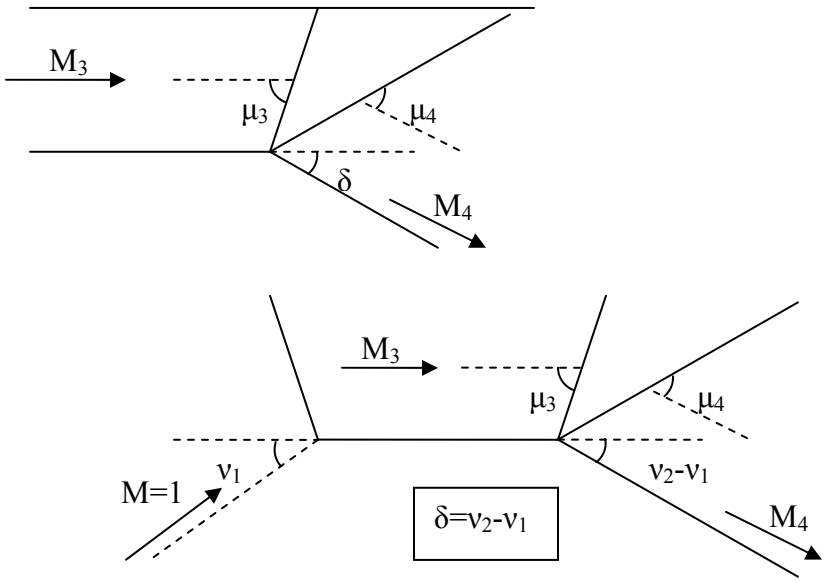

Fig. B. 3 Schematic of expansion flow prediction with Prandtl-Meyer theory

Prandtl-Meyer Formula: $$\nu_1 = \left[\sqrt{\frac{\gamma+1}{\gamma-1}}\tan^{-1}\sqrt{\frac{\gamma-1}{\gamma+1}\left(M_3^2-1\right)} - \tan^{-1}\sqrt{M_3^2-1}\right] = 25.9^{\circ} \quad (56)$$

Using an iterative process to find M_4 where ν_1 is subtracted by both sides setting the equation = 0:

$$0=\left[\sqrt{\frac{\gamma+1}{\gamma-1}}\tan^{-1}\sqrt{\frac{\gamma-1}{\gamma+1}\left(M_4^2-1\right)} - \tan^{-1}\sqrt{M_4^2-1}\right] - \nu_2 \quad (57)$$

$$M_4 = 2.42 \quad (58)$$

$$\frac{P_4}{P_3} = \left[\frac{2+(\gamma-1)M_3^2}{2+(\gamma-1)M_4^2}\right]^{\frac{\gamma}{\gamma-1}} = .503 \tag{59}$$

$$P_4 = P_3 \frac{P_4}{P_3} = 2.25 \text{ atm} \tag{60}$$

$$\frac{T_4}{T_3} = \frac{2+(\gamma-1)M_3^2}{2+(\gamma-1)M_4^2} = .822 \tag{61}$$

$$T_4 = T_3 \frac{T_4}{T_3} = 379 \text{ K} \tag{62}$$

$$\mu_3 = \sin^{-1}\left(\frac{1}{M_3}\right) = 30.317^\circ,\ \mu_4 = \sin^{-1}\left(\frac{1}{M_4}\right) = 24.4023^\circ \tag{63}$$

Supersonic Nozzle Design Theory

The purpose of using this method is to obtain the Mach number before the impending shock at region 6. Using method of characteristics, the determination of flow patterns can be obtained through reflecting characteristic lines compared to reflecting expansion waves. This can also help in determining the Mach number without the knowledge of pressure or temperature in all locations. Assuming isentropic conditions across expansion waves, the total pressure and temperature are assumed constant with decreasing static pressure and temperature.

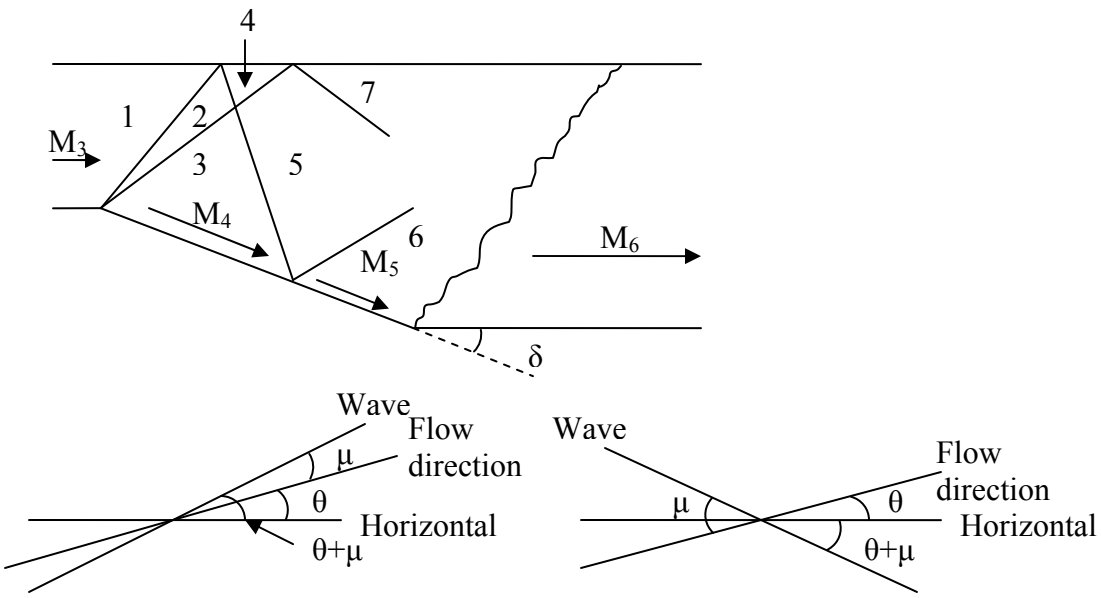

Fig. B. 4 Representation of expansion flow with characteristic lines and region labeling

Table B. 1. Characteristic flow parameters listed by region

Region	θ (deg)	ν (deg)	M	μ (deg)	θ+μ (deg)	θ-μ (deg)
1	0.00	25.9	1.981	30.3	30.3	-30.3
2	5.68	31.5	2.19	27.1	32.8	-21.5
3	11.36	37.2	2.42	24.4	35.8	-13.06
4	0.00	37.2	2.42	24.4	24.4	-24.4
5	5.68	42.9	2.67	22.0	27.7	-16.34
6	11.36	48.6	2.94	19.89	31.2	-8.52
7	0.00	48.6	2.94	19.86	19.89	-19.89

Known values: $\theta_1 = 0°,\ \theta_4 = 11.36°,\ \mathrm{M}_1 = 1.981,\ \nu_1 = 25.9°$ (64)

$$\Delta\nu = \Delta\theta = 11.361° - 0° = \nu_4 - 25.9° \quad \therefore\ \nu_4 = 37.2° \tag{65}$$

Using the Prandtl-Meyer formula displayed on eq. 56, $\mathrm{M}_4 = 2.42$

$$\text{2-wave separation: } \Delta\nu/2 = \frac{\nu_4 - \nu_1}{2} = 5.68° \tag{66}$$

$$\therefore\ \Delta\nu = \Delta\theta \text{ and } \frac{\theta}{2} = \theta_1 + \theta_2, \quad \theta_2 = 5.6805° - 0° = 5.68° \tag{67}$$

$$\nu_2 = \Delta\nu + \nu_1 = 31.5° \tag{68}$$

$$\theta_3 = \frac{\Delta\theta}{2} + \theta_2 = 11.36° \tag{69}$$

$$\nu_3 = \nu_2 + (\theta_3 - \theta_2) = 37.2° \tag{70}$$

$$\nu_5 = \frac{(\nu_4 - \theta_4) + (\nu_3 + \theta_3)}{2} = 42.9° \tag{71}$$

$$\theta_5 = \theta_4 + (\nu_5 - \nu_4) = 5.68° \tag{72}$$

$$\theta_6 = \theta_3 = 11.36° \tag{73}$$

$$\nu_6 = \nu_5 + (\theta_6 - \theta_5) = 48.6° \tag{74}$$

$$\theta_7 = \theta_4 = \theta_1 = 0° \tag{75}$$

Use the Prandtl-Meyer formula to determine the Mach number in each region based on ν_x. Given the Mach number, the flow direction can be determined relative to the characteristic line:

$$\mu_x = \sin^{-1}\left(\frac{1}{M_x}\right), \text{ where x=region location} \tag{76}$$

Based on this information, the Mach number at region 6 is represented by M_5

$$M_5 = 2.94 \tag{77}$$

$$P_{o5} = P_{o4} = P_{o3} = 33.7 \text{ atm} \tag{78}$$

$$\frac{P_5}{P_3} = \left[\frac{2+(\gamma-1)M_3^2}{2+(\gamma-1)M_5^2}\right]^{\gamma/\gamma-1} = .227 \tag{79}$$

$$P_5 = P_3\frac{P_5}{P_3} = 1.012 \text{ atm} \tag{80}$$

$$\frac{T_5}{T_3} = \frac{2+(\gamma-1)M_3^2}{2+(\gamma-1)M_5^2} = .654 \tag{81}$$

$$T_5 = T_3\frac{T_5}{T_3} = 302 \text{ K} \tag{82}$$

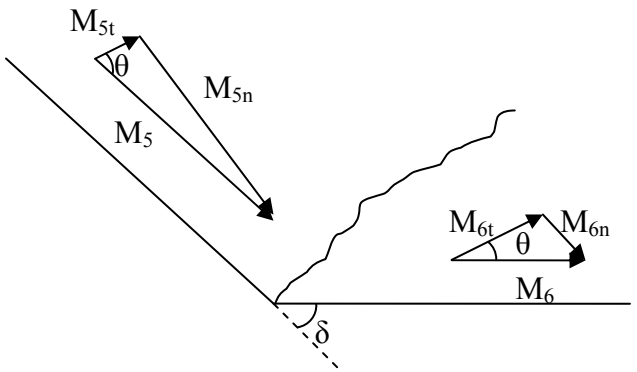

Fig. B. 5 Final shock schematic near exit of CD nozzle

$$\lambda = \sqrt{\left(M_5{}^2 - 1\right)^2 - 3\left(1 + \frac{\gamma - 1}{2} M_5{}^2\right)\left(1 + \frac{\gamma + 1}{2} M_5{}^2\right)\tan^2\delta} = 7.35 \tag{83}$$

$$\chi = \frac{\left(M_5{}^2 - 1\right)^3 - 9\left(1 + \frac{\gamma - 1}{2} M_5{}^2\right)\left(1 + \frac{\gamma - 1}{2} M_5{}^2 + \frac{\gamma + 1}{4} M_5{}^4\right)\tan^2\delta}{\lambda^3} = .989 \tag{84}$$

$$\theta = \tan^{-1}\left\{\frac{M_5{}^2 - 1 + 2\lambda\cos\left[\left(4\pi x + \cos^{-1}\chi\right)/3\right]}{3\left(1 + \frac{\gamma - 1}{2} M_5{}^2\right)\tan\delta}\right\} = 28.6^\circ \tag{85}$$

Where $\left\{\begin{matrix} x = 1 \text{ for weak shocks} \\ x = 0 \text{ for strong shocks} \end{matrix}\right\}$

$$M_{5_n} = M_5 \sin\theta = 1.429 \tag{86}$$

$$M_{6_n} = \sqrt{\frac{\left[M_{5_n}^2\left(\gamma - 1\right)\right] + 2}{2\gamma M_{5_n}^2 - \left(\gamma - 1\right)}} = .728 \tag{87}$$

$$\frac{T_6}{T_5}=\left[1+\frac{2\gamma\left(M_{5_n}^2-1\right)}{\gamma+1}\right]\left[\frac{2+(\gamma-1)M_{5_n}^2}{(\gamma+1)M_{5_n}^2}\right]=1.274 \tag{88}$$

$$T_6=T_5\frac{T_6}{T_5}=384\text{ K} \tag{89}$$

$$\mathrm{M}_{6_t}=M_5\cos(\theta)\sqrt{\frac{T_5}{T_6}}=2.28 \tag{90}$$

$$\mathrm{M}_6=\sqrt{M_{6_n}^2+M_{6_t}^2}=2.39 \tag{91}$$

$$\frac{P_6}{P_5}=1+\frac{2\gamma\left(M_{5_n}^2-1\right)}{\gamma+1}=2.21 \tag{92}$$

$$P_6=P_5\frac{P_6}{P_5}=2.24\text{ atm} \tag{93}$$

$$\frac{P_{o6}}{P_{o5}}=\left[\frac{(\gamma+1)M_{5_n}^2}{2+(\gamma-1)M_{5_n}^2}\right]^{\frac{\gamma}{\gamma-1}}\left[\frac{\gamma+1}{2\gamma M_{5_n}^2-(\gamma-1)}\right]^{\frac{1}{\gamma-1}}=.951 \tag{94}$$

$$P_{o6}=32.0\text{ atm} \tag{95}$$

Vita

Jaime Enrique Pérez was born in San Antonio, TX on January 11, 1984. He was raised in Georgia and went to high school at Lee County High School in Leesburg. He entered the Regent's Engineering Transfer Program at Georgia Southern University, and then transferred to the Georgia Institute of Technology and received a B.S. in aerospace engineering in 2006. Jaime is currently pursuing his master's in aviation systems at the University of Tennessee Space Institute, Tullahoma, TN.